2014

Carbon nanomaterials as electrodes in thermogalvanic cells for waste heat recovery

Mark S. Romano
University of Wollongong

UNIVERSITY OF WOLLONGONG

Intelligent Polymer Research Institute

Australian Institute for Innovative Materials

Carbon Nanomaterials as Electrodes in Thermogalvanic Cells for Waste Heat Recovery

Mark S. Romano

This thesis is presented as part of the requirements for the

Award of the Degree of

Doctor of Philosophy

from

The University of Wollongong

2014

CERTIFICATION

I, Mark S. Romano, declare that this thesis, submitted in partial fulfilment of the requirements for the award of Doctor of Philosophy, in the Australian Institute for Innovative Materials, University of Wollongong, is wholly my own work unless otherwise referenced or acknowledged. The document has not been submitted for qualifications at any other academic institution.

Mark S. Romano
2014

ABSTRACT

A possible solution to the worlds growing energy problem is to improve the efficiency of energy conversion processes by harnessing waste heat. Thermogalvanic systems, also known as thermocells, allow the direct conversion of thermal to electrical energy. A device consists of two electrodes operating at different temperatures and placed in contact with a redox-based electrolyte. The temperature dependence of the redox reactions generates a potential difference such that when the thermocell is connected to an external circuit, current and power may be extracted.

The initial part of this work focused on an investigation of $K_3Fe(CN)_6/K_4Fe(CN)_6$ concentration (in aqueous media) as the electrolyte for thermocell applications with carbon based electrodes. Thermocell performance is maximised through the use of 0.4 M $K_3Fe(CN)_6/K_4Fe(CN)_6$ due to the low thermal conductivity and high ionic conductivity of said solution.

Various thermocell designs were developed to understand how electrodes should be positioned to achieve increased power output. With electrodes placed far apart, a large temperature difference between electrodes may be attained. However, this results in a lower current density because of the larger distance that ions need to diffuse in the thermocell. Electrodes also need to be oriented such that reaction products from the cathode only need to travel in a straight path to get to the anode, and vice versa. A T-shaped thermocell produced the highest power density due to the optimum electrode position.

Composite electrodes of single-walled carbon nanotubes (SWNT) and reduced graphene oxide (rGO) for thermocell applications were developed and tested. The best performing electrode had a composition of 90 % SWNT and 10 % rGO by weight and a thickness of 4.5 μm. This optimised electrode favours rapid electrolyte diffusion and more efficient access to the electroactive surface area. Further enhancements in thermocell performance were realised through the use of a novel stacked electrode configuration, which consists of 10 alternating layers of the optimised SWNT-rGO film and stainless steel. Using the stacked electrode, a power conversion efficiency

relative to a Carnot engine (Φ_r) of 2.63 % was attained. To date this Φ_r is the highest reported value in thermocells.

The optimised SWNT-rGO composite was incorporated into carbon cloth in order to investigate the effect of vascular electrode structures on thermocell performance. The maximum power density (585 mW/m^2) is obtained by dip coating the carbon cloth with 5 layers of the SWNT-rGO composite. Excessive amounts of the nano-carbon composite blocks the pores in the carbon cloth and reduces the performance of the vascular structure.

ACKNOWLEDGEMENTS

This work would not have been completed without the help of numerous individuals who unselfishly gave their support.

To my supervisor, Associate Professor Jun Chen, for sharing your knowledge on electrochemistry, your technical advice and encouragement, thank you. My gratitude goes out to my co-supervisor, Professor Gordon Wallace for the support and guidance throughout the course of my PhD.

A big "thank you" goes out to Dr Joselito Razal for the invaluable assistance in writing up the various manuscripts published as a result of this study. Also for helping me to adjust to a new environment and culture. I acknowledge the following for their help with various technical aspects of my PhD: Dr Adrian Gestos for getting me started on thermal harvesting experiments. Dennis Antiohos for assistance in synthesis and characterisation of reduced graphene oxide. Dr Andrew Nattestad and Dr Stephen Beirne for helping design and print various device components.

For the financial assistance extended, I would like to thank The Department of Science and Technology, Philippines.

To the Razal, Arrogante, Ramos, Villaruz, and Tabaranza families for your friendship and being my "second family" here in Australia.

I would like to thank my family for the support and love they gave me. The constant reminders to finish my thesis really helped

To my wife, Anna Gianellie Adriatico-Romano, you have my heartfelt thanks for putting up with me through the rollercoaster ride that has been my PhD. I would not be writing this acknowledgement if not for your unwavering love and support.

And of course, I thank Almighty God for showering His divine grace and giving me the strength to stay awake through all the sleepless nights.

PUBLICATIONS

M.S. Romano, N. Li, D. Antiohos, J.M. Razal, A. Nattestad, S. Beirne, S. Fang, Y. Chen, R. Jalili, G.G. Wallace, R. Baughman, J. Chen, *Carbon Nanotube - Reduced Graphene Oxide Composites for Thermal Energy Harvesting Applications*, **Advanced Materials**. (accepted September 2013)

D. Antiohos, K. Pingmuan, **M.S. Romano**, S. Beirne, T. Romeo, P. Atchison, A Minnett, G. Wallace, S. Phanichphant, J. Chen, *Manganosite-Microwave Exfoliated Graphene Oxide Composites for Asymmetric Supercapacitor Device Application*, **Electrochimica Acta**. (accepted September 2012)

D. Antiohos, **M.S. Romano**, J.M. Razal, J. Chen, *"Recent Progress in Carbon Nanotube Research"*, Book chapter: *Carbon Nanotubes for Energy Applications*, **Publisher-Intech**. (accepted September 2012)

M.S. Romano, S. Gambhir, J.M. Razal, A. Gestos, G. Wallace, J. Chen, *Novel Carbon Materials for Thermal Energy Harvesting*, **Journal of Thermal Analysis and Calorimetry**. (accepted February 2012)

ABBREVIATIONS

PCE – power conversion efficiency

CNTs – carbon nanotubes

MWNT – multi walled carbon nanotube

SWNT – single walled carbon nanotubes

SSA – specific surface area

BET - Brunauer-Emmett-Teller isotherm

CVD – chemical vapour deposition

P-SWNT – purified single walled carbon nanotubes

EIS – electrical impedance spectroscopy

P-MWNT – purified multi walled carbon nanotubes

NCNTs – nitrogen-doped carbon nanotubes

BCNTs – boro-doped carbon nanotubes

GO – graphite oxide

eGO – exfoliated graphene oxide

rGO – reduced graphene oxide

CCG – chemically reduced graphene

NMP – N-methyl-pyrrolidon

SDBS – sodium dodecylbenzene sulphonate

SC – sodium cholate

TGA – Thermogravimetric analysis

UV-Vis – Ultraviolet-Visible spectroscopy

SEM – scanning electron microscope

CV – cyclic voltammetry

CAD – computer aided design

CHP – 1-cyclohexyl-2-pyrrolidone

CRGO – chemically reduced graphene oxide

I_{mass} – mass current density

V_{oc} – open circuit voltage

R_{ct} – charge transfer resistance

R_s – solution resistance

ESA – electroactive surface area

EPD – electrophoretic deposition

TABLE OF CONTENTS

LIST OF FIGURES

LIST OF TABLES

CHAPTER 1

Thermocells, Carbon Nanotubes and Graphene Electrode Materials

1.1 The energy problem

Energy, whether in the form of oil, gasoline or electricity is an essential constituent of all economic activity [1]. The constant increase in population coupled with demands for a more energy intensive standard of living resulted in the energy crisis during the 1970s. This led to the development of renewable energy sources and energy conservation measures. These programs were scaled back as the energy supply eventually met society's demands. In the 1980s, the dangers of pollution led to programs concerned with minimising/reversing the environmental impact of fossil fuels (coal, oil, and gas) extraction, transport, and consumption [2]. In 2007, the world's primary energy use increased by 2.4%, which has resulted in enormous strain on the global energy supply. This is made apparent by the skyrocketing of oil prices (cost per barrel: $28 in 2003, $38 in 2005 and $100 in 2010) and the increased cost of commodities that utilize petroleum for manufacture and transport [3-6]. Data from the United States Department of Energy (Figure 1.1) show the constant rise in the world's energy consumption from 1980. They also predict that the world's energy consumption will increase by 20% over the next 20 years [7]. The constant consumption of fossil fuels coupled with its detrimental effect on climate change has spurred research on renewable, alternative and green energy systems [8].

Development of materials and engineering improvements for energy conversion systems, capable of harnessing unorthodox sources, is vital due to the constant rise of energy costs associated with a more energy intensive lifestyle of an ever growing population [9].

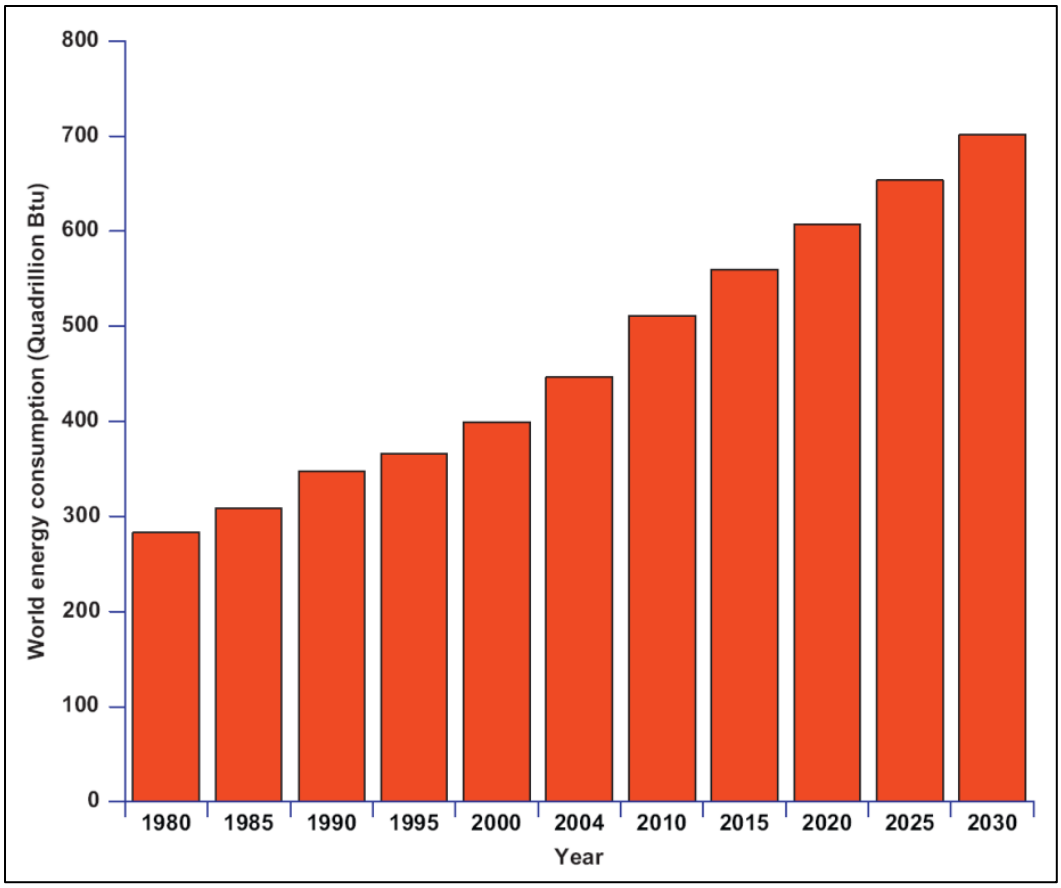

Figure 1.1 Values and forecasts for energy utilisation from 1980 to 2030 by The United States Department of Energy. Reprinted from [7] with permission from Elsevier.

1.2 Thermal energy harvesting

1.2.1 Waste heat sources

Low grade heat (normally around 130 ^{o}C) is a by-product of almost all human activity, especially when energy conversion is involved. Low grade heat is also known as “waste heat” because the dissipated heat into the environment is unutilised. For example, when thermal energy is transduced to mechanical work by heat engines, excess heat is always produced. This is supported by the second law of thermodynamics, which states that no heat engine can attain 100% efficiency. Another scenario of this can be seen in cars, wherein their motors waste around 70% of the energy generated. This wasted energy dissipates into the environment through a hot exhaust pipe and warm brakes. Another example is the Wartsila-Sulzer RTA96-C turbocharged two-stroke diesel engine, reputed to be among the most efficient in the world. However, only 50% of the energy in the fuel can be converted to useful motion, with the remainder ending up as waste heat [10]. Waste heat also exists in factories, particularly in the steel and glass production industries. Pipes that carry hot liquids are also low grade heat sources. Other scenarios wherein heat simply dissipates into the environment are power plants, geothermal sources, household appliances, and various electronic gadgets.

Progress in the field of low grade thermal energy conversion can lead to more effective use of the ever-present energy source that is waste heat. Systems capable of harnessing waste heat would be able to provide supplemental power to current energy conversion systems and help address the challenges of climate change and the finite nature of fossil fuels [11].

1.2.2 Thermogalvanic cells

Studies on the conversion of heat to electricity have been conducted as early as the 1960s [12]. Since then, several thermal converters have been developed to transduce waste heat into electrical power. Examples are ferromagnetic materials, thermocouples and thermionic converters. However, these systems yield extremely low conversion efficiencies [13-15]. Advances in the more popular thermoelectric system has been hampered by its high initial cost and material limitations; as these systems operate in the temperature range much higher than low grade heat [16]. Another drawback to thermoelectrics is their inflexible nature, limiting their applications to flat surfaces [16]. Scenarios wherein waste heat is generated from a curved surface, i.e. heating/cooling pipes or exhaust pipe on an automobile, would be inapplicable to thermoelectric systems.

One device that shows promise as a cheap thermoenergy conversion system is a thermogalvanic cell, also known as a thermocell. It is a non-isothermal electrochemical cell that is able to directly transduce thermal energy to electrical power [17]. This electrochemical system consists of two electrodes (usually identical) that are held at different temperatures and placed in contact with a redox-based electrolyte [18, 19]. Thermocells utilise the temperature dependence of the direction of redox reactions to generate a potential difference; i.e. the two half-cells of the system are held at varying temperatures causing a difference in redox potentials of the mediator at the anode and cathode [19]. This reaction can drive electrons through an external circuit that allows generation of current and power [20, 21]. Various electrolytes have been used for thermocells: molten salt electrolytes, solid electrolytes and aqueous electrolytes [22, 23].

A schematic of a thermocell with a ferri-/ferro-cyanide redox couple is shown in Figure 1.2.

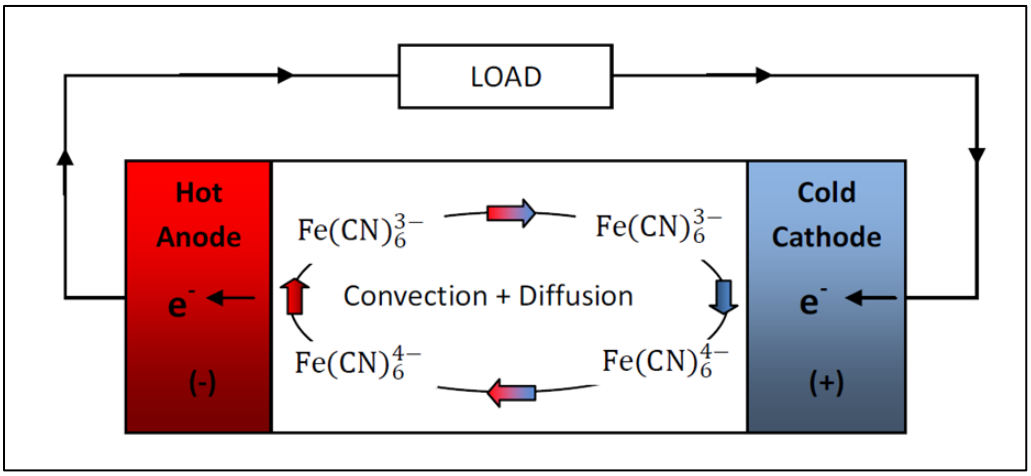

Figure 1.2 Schematic diagram of a ferri-/ferro-cyanide redox thermogalvanic cell. Reproduced from [24] with permission from Springer Science and Business Media.

For the cell shown, ferrocyanide is oxidized at the hot anode, the electron donated then travels through an external circuit and returns to the cell via the cold cathode where it is consumed in the reduction of ferricyanide [25]. The electrolyte composition is maintained by the balance of oxidized and reduced species; i.e. for each mole of ferrocyanide being oxidized an equivalent number of moles of ferricyanide are being reduced. The accumulation of reaction products at either half-cell is prevented by the diffusion and convection of the electrolyte that occurs naturally and allows the cell to operate in a self-regenerative manner. Moving mechanical components are not needed for thermocell operation as mass transport occurs naturally [20].

As mentioned earlier, the simple design of these systems allows them to function without the need for moving parts. This aspect, coupled with their stability allows operation for extended periods without regular maintenance. This translates to decreased operational costs. Thermocells also have zero carbon emission hence will not contribute

to the environmental impact of electrical power generation. The flexible nature of these systems will allow them to be conformed into various shapes wherein waste heat may be sourced [26].

1.2.3 Power conversion efficiency for thermogalvanic cells

As with any heat engine, a thermogalvanic cell is driven by the transport of entropy from a region of elevated temperature to a region of low temperature [21]. The thermoelectric power or Seebeck coefficient ($\Delta V/\Delta T$) of a material is the amount of thermoelectric voltage generated in response to a temperature difference across it. It is dictated by the structural entropy induced by ion and solvent interactions [27]. It must be noted that the term thermoelectric power is a misnomer since it is not concerned with power production but instead gives the electric field induced by differences in temperature. Assuming the hypothetical redox system A + ne^- ↔ B occurs in the thermocell, the Seebeck coefficient may be expressed as shown in Equation 1.1 [28].

$$nF\left(\frac{\Delta V}{\Delta T}\right)_{t=\infty} = (S_B + S_B^*) - (S_A + S_A^*) - n\overline{\overline{S_e}} \qquad \text{Equation 1.1}$$

Where V represents the electrode potential, T is temperature, S_A and S_B are the partial molar entropies of species A and B accordingly, with their respective Eastman entropies of transport denoted by S_A^* and S_B^*, n is the number of electrons involved in the redox reaction, F is Faraday's constant, and $\overline{\overline{S_e}}$ is the transported entropy of electrons in the electrodes. The Eastman entropy of transport may be attributed to the interaction of an ion and its hydration shell with the solution. Ions in thermogalvanic

systems carry both their partial molar entropy and Eastman entropy of transport into the half-cell as each ion is consumed in one half-cell and produced in the other. It must be noted that Equation 1.1 is valid for conditions wherein sufficient time has been allowed for the thermocell to reach steady-state. The Seebeck coefficient is initially higher than the steady-state value as molecules around the hot electrode move faster than those surrounding the cold electrode, a phenomenon known as the Soret effect. Due to the Soret effect, concentration gradients develop in the thermocell wherein the concentration of reactants is higher at the cold side. Despite this, it is common practice to use the initial temperature dependence for two reasons: First, the final steady-state value of the Seebeck coefficient has been shown to take extended periods, even days to be achieved [29]. Second, systems that have a Seebeck coefficient large enough to be useful in thermocells have Eastman entropy of transport values that are small compared with their partial molar entropies [30]. This allows Equation 1.1 to be expressed as [20]:

$$nF\left(\frac{\Delta V}{\Delta T}\right)_{t=0} = S_B - S_A - n\overline{\overline{S}}_e \qquad \text{Equation 1.2}$$

For most thermocells, $\overline{\overline{S}}_e$ is usually infinitesimal. For example, copper leads result in $\overline{\overline{S}}_e < 2\mu V/K$ [30]. Equation 1.2 can now be approximated by:

$$\left(\frac{\Delta V}{\Delta T}\right)_{t=0} \cong \frac{S_B - S_A}{nF} \qquad \text{Equation 1.3}$$

The power output of thermogalvanic cells is dictated not only by $\Delta V/\Delta T$ but also by several overpotentials common in electrochemical cells which will be discussed later on.

The power conversion efficiency (Φ) of a thermocell is given by Equation 1.4 [31].

$$\Phi = \frac{\text{Electrical power output}}{\text{Thermal power flowing through the cell}} \qquad \text{Equation 1.4}$$

The thermal power flowing through the cell ($\partial Q/\partial T$) is largely controlled by cell design and electrolyte selection. It may be expressed as [32]:

$$\frac{\partial Q}{\partial T} = f_i + f_r \qquad \text{Equation 1.5}$$

Where f_i is the rate of heat flow from the hot electrode to the cold electrode induced by thermal conduction and f_r is the rate of heat transfer induced by the reversible heat of the cell reaction. The expression for the thermal power flowing through the cell can be expanded to give [30]:

$$\frac{\partial Q}{\partial T} = KA\frac{\Delta T}{d} + \frac{IT\Delta S}{nF} \qquad \text{Equation 1.6}$$

Where K is the thermal conductivity of the electrolyte, A is the electrode cross-sectional area, ΔT is the thermal gradient across the distance (d) between the two

electrodes, I is the cell current, ΔS is the entropy of the cell reaction, n is the number of electrons transferred, and F is the Faraday constant.

Inclusion of the reversible heat of cell reaction is only valid for thermocells wherein there is a net consumption of electrolyte. For thermogalvanic systems wherein the hot and cold electrodes are periodically switched or when a reversible redox couple is used, no net consumption of the electrolyte occurs. The expression for the thermal power flowing through the cell can be simplified to [30]:

$$\frac{\partial Q}{\partial T} = KA\frac{\Delta T}{d} \qquad \text{Equation 1.7}$$

It has been shown by Anderson et al. [32] that Equation 1.7 is a reasonable approximation to Equation 1.6 as very little chemical reactions occur in thermocells.

Qualitative behaviour of the current and voltage dependencies are shown in Figure 1.3; it depicts that the maximum electrical output power is obtained when the external and internal loads are equal.

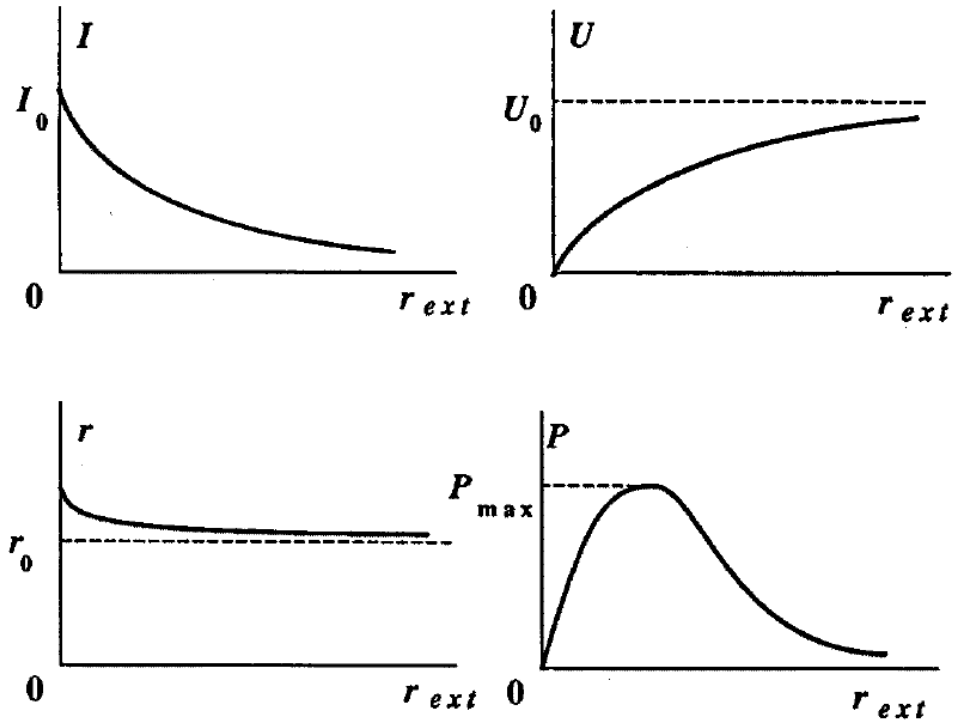

Figure 1.3 The typical dependencies of the current (*I*) on the effective voltage (*U*), internal resistance (*r*) and the useful power on the external resistance (r_{ext}). Reprinted from [31] with permission from Elsevier.

Based on Figure 1.3, the maximum electrical output power (P_{max}) is given by Equation 1.8 [31].

$$P_{max} = 0.25\, V_{oc} I_{sc} \qquad \text{Equation 1.8}$$

Where V_{oc} is the open circuit voltage and I_{sc} is the short circuit current. Rearranging Equation 1.3, we can see that V_{oc} is highly dependent on the reaction entropy of the redox couple ($\Delta S_{B,A}$) and the thermal gradient (ΔT) at which the electrodes are exposed to, as shown in Equation 1.9 [20].

$$V_{oc} = \frac{\Delta S_{B,A} \Delta T}{nF}$$ Equation 1.9

Short circuit current densities for thermocells cannot be reliably calculated using the Tafel equation [33]. This is due to the difficulty of reproducibly measuring exchange currents, wherein there is significant variability from one research group to another. The current generation capability of thermocells is best done by direct measurements. It must be noted that based on the Tafel equation, short circuit current density scales with exchange current densities for thermocells provided that ohmic and mass transport resistances are kept at a minimum.

Using Equation 1.7 and Equation 1.8, the power conversion efficiency (Equation 1.4) can be expressed as shown in Equation 1.10.

$$\Phi = \frac{0.25\, V_{oc} I_{sc}}{KA\left(\frac{\Delta T}{d}\right)}$$ Equation 1.10

A direct comparison of power conversion efficiency (PCE) of different power conversion devices would be inaccurate, owing to complications that arise from the difference in operating temperatures used. A convenient method of standardising power conversion measurements in thermal converters is to compare their power conversion efficiency relative to that of a Carnot engine operating between the same temperatures Φ_r (Equation 1.11).

$$\Phi_r = \frac{\Phi_{Thermogalvanic\ cell\ operating\ at\ \Delta T}}{\Phi_{Carnot\ engine\ operating\ at\ \Delta T}}$$ Equation 1.11

This facilitates relatively accurate comparisons of thermogalvanic cells having different operating conditions, i.e. thermal gradient, electrolyte, electrode separation, etc. [20].

Ohmic, mass transport and activation overpotentials are losses that need to be minimised in order to realise an improvement in thermocell conversion efficiency. At large electrode separations, ohmic overpotential is dictated by the electrolyte resistance; and mass transport overpotential is maximized. By decreasing the inter-electrode separation, an increase in short circuit current will be observed; resulting in larger amounts of generated power. This is because both ohmic and mass transport overpotentials will decrease. However, the power conversion efficiency will be lowered owing to the higher thermal flux flowing from the hot to cold side of the cell, i.e. it will be harder to maintain the thermal gradient [34]. Thermocells should be designed so as to exploit the natural convection induced by the differences in temperature. The optimum configuration for thermocells using the ferri-/ferro-cyanide redox mediator is to hold the cold electrode above the hot electrode or have the two electrodes side by side. These orientations result in larger output power as the mass transport overpotential is minimised owing to the different densities of ferri- and ferro-cyanide [18]. It has been shown that changes in the concentration of the redox couple will change the thermal conductivity of the electrolyte, thus affecting its ability to maintain a thermal gradient between the anode and cathode [24]. Optimisation of electrolyte concentration coupled with appropriate cell design is necessary to mitigate both ohmic and mass transport overpotentials while maintaining large power conversion efficiency.

Activation overpotential is associated with the activation barrier/voltage needed to carry out reactions at the electrode. For the same activation overpotential, larger current densities are realised when the exchange current density is increased. This increase in exchange current density is attained when the concentration of the redox couple in the electrolyte is maximised, the thermal gradient is increased and the number of possible reaction sites is augmented [35]. Porous electrodes have the advantage of increased electroactive surface area and will directly amplify the short circuit current density [26]. It must be noted that for porous electrodes, short circuit current density does not increase indefinitely with electrode thickness as mass transfer overpotential will become limiting. The reaction products formed within the pores of the anode will not be able to diffuse fast enough to the cathode and vice versa, generating concentration gradients around both electrodes [35]. Another way to decrease the activation overpotential in thermocells is by using catalytic electrodes attained by doping [36].

Initial research on thermocells focused on platinum electrodes, the archetypal non-reactive catalytic material. In fact, a study on the effects of platinum electrode cleaning was performed and it was deduced that this affects the power delivery characteristics of thermogalvanic cells [18]. If power inputs are ignored, such as mechanical stirring, thermocells with platinum electrodes are able to attain power conversion efficiency relative to a Carnot engine of 1.2 %. However, if power inputs are strictly excluded, Φ_r drops to ~0.5 % [20]. Such low efficiencies coupled with the high cost of this noble metal are reasons why thermocells have remained unsuitable for practical applications.

1.3 Carbon nanotubes

The research of Sumio Iijima into molecular carbon structures led to his discovery of carbon nanotubes (CNTs) in 1991 [37]. A CNT could be an individual layer of carbon atoms bonded in a hexagonal lattice that has been rolled up to have a cylindrical shape, this is known as a single-walled carbon nanotube (SWNT, Figure 1.4).

Figure 1.4 Schematic representation of a SWNT [38]

If several layers of carbon atoms are rolled up concentrically, the resulting structure is called a multi-walled carbon nanotube (MWNT, Figure 1.5). The exceptional electrical transport and mechanical stability of CNTs in a wide range of electrolytes has led to widespread research on this material for use as electrodes in electrochemical applications [37, 39-42].

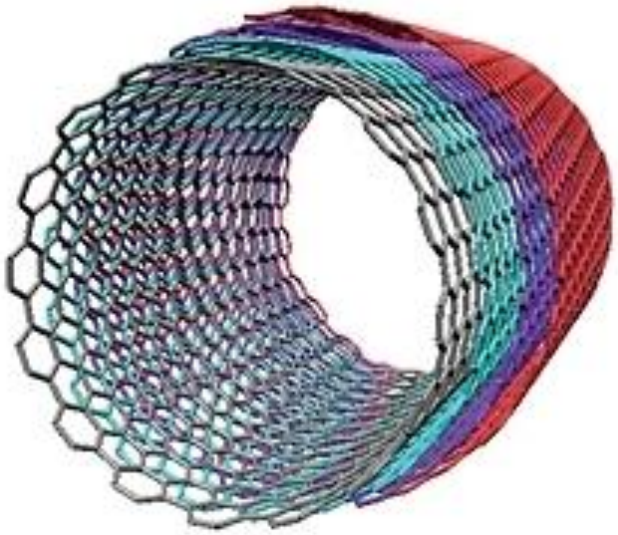

Figure 1.5 Schematic representation of a MWNT. Reprinted from [43] with permission from the University of Waterloo.

CNT electrodes are known to exhibit Nernstian behaviour and more importantly, fast electron transfer kinetics with the redox couple ferri-/ferro-cyanide. Peak potential separation in cyclic voltammograms obtained using micron-sized MWNT electrodes and 5 mM potassium ferrocyanide is 59 mV, which is the expected theoretical value and implies that the highest electron transfer rate was attained [44]. Incidentally, the ferri-/ferro-cyanide redox couple has been studied intensively in thermocell applications owing to the large Seebeck coefficient it possesses. The Seebeck coefficient of 1.4 mV/K for the ferri-/ferro-cyanide redox couple implies that an open circuit potential of 84 mV is attainable at a thermal gradient of 60 ^{o}C (the usual limit for aqueous systems without significant cooling) [35]. The fast electron transfer of CNTs in ferri-/ferro-cyanide justifies its use as electrodes in thermocells.

The nanometre diameter of CNTs gives rise to large gravimetric and volumetric specific surface areas (SSA). Their unique aspect ratios allow porous

electrodes to be fabricated by a variety of methods. Theoretically the SSA of CNTs can range from 50-1315 m^2/g, the value being dictated by the number of walls [45]. Theoretical predictions are in good agreement with experimental values obtained by the measurement of the amount of gas (usually N_2) adsorbed at 77 K and calculations using the Brunauer-Emmett-Teller (BET) isotherm. Kaneko et al. [46] have reported that MWNTs are mesoporous while Rao et al. [47] have shown that SWNTs are microporous. MWNT buckypapers (films made from a dispersion of CNT powders that has been vacuum filtered) of the same geometric area compared with platinum foil are known to have three times larger charging current density during cyclic voltammetry in a ferri-/ferro-cyanide aqueous electrolyte [26], evidence of the large accessible SSA of CNT electrodes. The large SSA of CNTs allows for a greater number of electroactive sites. When the CNT electrode porosity is controlled and the tortuousity is minimised in thermogalvanic cells (so that mass transfer is not limited within the electrode), the short circuit current generated can be significantly augmented [48].

1.3.1 Current processing techniques for CNTs relevant to thermocells

1.3.1.1 Solvent/surfactant exfoliation

One of the major obstacles to research on CNT characterisation and application is their spontaneous aggregation brought about by attractive van der Waals interactions in both aqueous and organic solutions. The resulting aggregates or “bundles” can reach lengths of several microns and diameters of tens of nanometres. Debundling of these aggregates is essential as they have mediocre

properties as compared to individual tubes. Reproducibility of results also becomes an issue when CNTs are not dispersed adequately.

Liquid phase separation is one of the simplest methods wherein stable CNT dispersions are attainable. Stable well-exfoliated CNT dispersions are achieved by appropriate selection of the solvent as forced dispersion via ultrasonication will result in agglomeration of the CNTs in a very short span of time. Selection of solvents can be based on the enthalpy of mixing per solvent volume ($\Delta\overline{H}_{mix}$) [49]:

$$\Delta\overline{H}_{mix} = \frac{2}{R_{bun}}(\delta_{NT} - \delta_{sol})^2\phi \qquad \text{Equation 1.12}$$

Where R_{bun} is the radius of the dispersed nanotube bundles, δ_{NT} and δ_{sol} are square roots of the nanotube and solvent surface energies respectively, and ϕ is the nanotube volume fraction. The solubility theory states that a negative free energy of mixing ($\Delta\overline{G}_{mix}$) is indicative of a stable dispersion.

$$\Delta\bar{G}_{mix} = \Delta H_{mix} - T\Delta\bar{S}_{mix} \qquad \text{Equation 1.13}$$

The entropy of mixing per unit volume ($\Delta\bar{S}_{mix}$) of nanotubes is generally small owing to their size and rigidity [50]. In order to minimise $\Delta\overline{G}_{mix}$ then solvents which result in small values of ΔH_{mix} are necessary. Based on Equation 1.12 the most effective solvents at dispersing CNTs would be those that have a surface energy close to the nanotube surface energy (~70 mJ/m^2); i.e. solvents with a surface tension around 40 mJ/m^2 [51].

Another method to attain stable dispersions of CNTs is through the use of surfactants. The inherent advantage of the use of surfactants over solvent dispersion is that the former is carried out in aqueous media, lessening its hazards and environmental impact. Surfactants rely on the principle wherein colloids are stabilized by surface charges [52]; i.e. Coulombic repulsion. Adsorption of the amphiphilic surfactant molecules onto CNTs is attained through their hydrophobic tails. This introduces a removable surface charge that creates an electric double layer around the nanotube; of which the magnitude and sign is proportional to its zeta potential [53]. This electric double layer provides repulsive forces that counteract the attractive van der Waals forces [54]. Selection of surfactants for CNTs dispersion depends on the size of their molecules. Low molecular weight surfactants will be able to pack tightly around the nanotube surface resulting in better stabilisation [55].

Filtration of CNT dispersions results in a planar mat of randomly arranged tubes [56] that can be up to several hundred microns thick. These free standing films or buckypapers (Figure 1.6) have been instrumental in CNT evaluation (owing to their simple processing) as electrode materials not only for thermocells but for other electrochemical applications as well. Post-treatment of buckypapers via annealing or acid washing is essential to ensure complete removal of the solvent or surfactant used to attain the CNT dispersion [57].

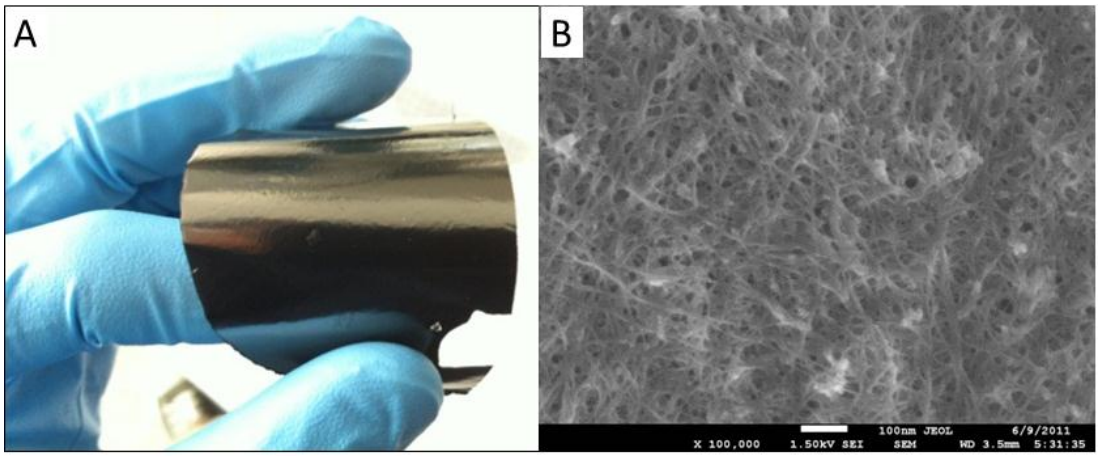

Figure 1.6 A) Free standing film of CNTs made by filtration, B) SEM image of the surface of the film shown in A. Reprinted from [58] with permission from INTECH.

1.3.1.2 Chemical vapour deposition

Chemical vapour deposition (CVD), a process that involves deposition of solids from a gas phase, has proven to be a viable method for attaining highly oriented CNTs on planar substrates (Figure 1.7) [59]. One of the theories behind the high degree of alignment is the reduction in free energy brought about by the van der Waals interactions along the tube length inducing coordinated growth by holding the tubes together [60]. The ability to tailor the growth of CNTs in three dimensional configurations is highly advantageous in thermocell applications. This configuration promotes enhanced ion accessibility with the CNT matrix allowing a larger current to be generated. The alignment of the tubes also minimises the tortuosity of the CNT electrodes which decreases the probability of forming concentration gradients within the electrode itself, leading to a decrease in the mass transfer overpotential. The wide range of substrates that can be used for CNT synthesis (metallic, carbon, etc) via CVD allows the fabrication of electrodes with a high degree of flexibility; materials that are highly desirable in thermocells [61].

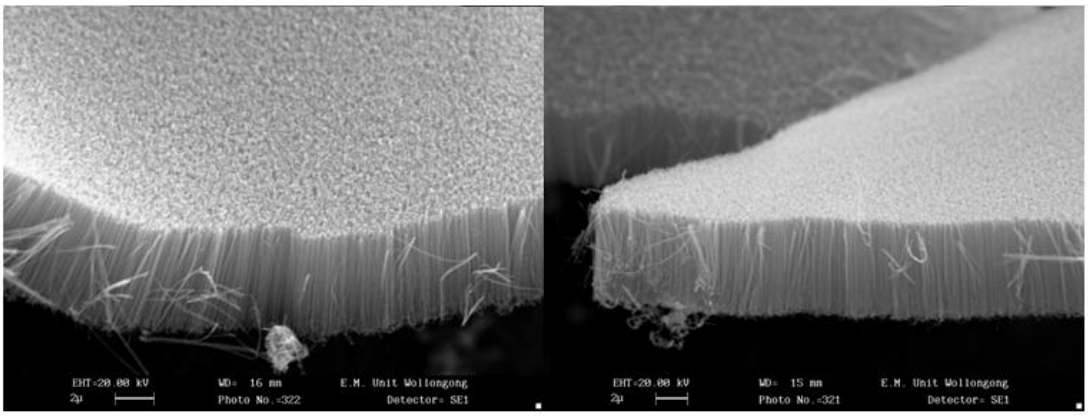

Figure 1.7 Aligned CNTs produced via CVD. Reprinted from [58] with permission from INTECH.

1.3.2 SWNT and MWNT for thermocell applications

CNTs were first used as thermocell electrodes in 2009 by Hu et al [26]. They were able to obtain an areal power density of 1.36 W/m^2 through the use of MWNT buckypaper electrodes (with less than 1 % catalyst and with MWNT diameter of around 10 nm) having an area of 0.5 cm^2. They employed a U-Cell with electrode separation of 5 cm, a temperature gradient of 60 ^{o}C wherein T_{cold} = 5 ^{o}C, and 0.4 M solution of $K_3Fe(CN)_6/K_4Fe(CN)_6$. A schematic of the cell they used is shown in Figure 1.8. Platinum electrodes they tested under the same conditions generated an areal power density of 1.02 W/m^2, proving that CNTs are viable materials for thermocell electrodes.

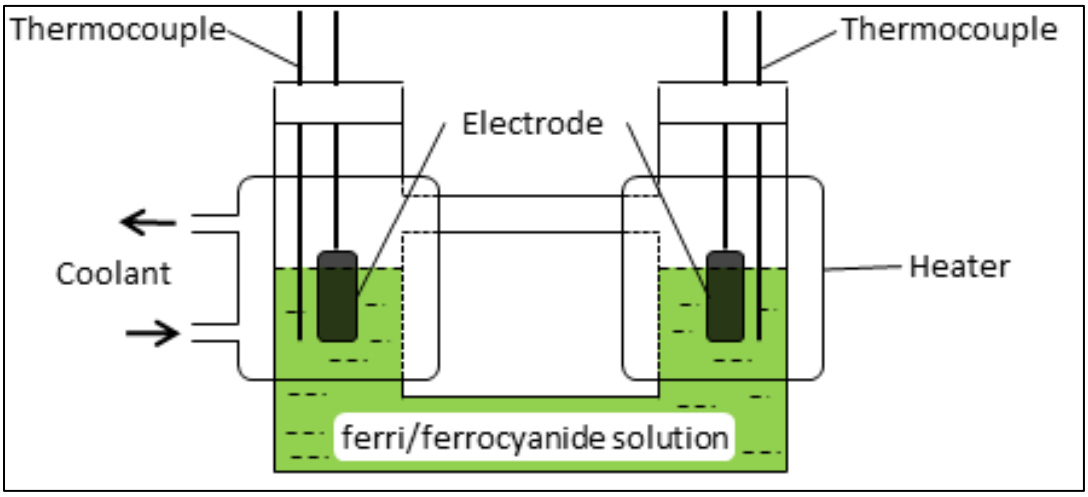

Figure 1.8 Schematic of the U-Cell used by Hu et. al for thermal energy harvesting. Reprinted from [58] with permission from INTECH.

SWNT powders produced by arc discharge (ASA-100F, Hanwha Nanotech) with an average diameter of 1.3 nm, and composition of 20-30 wt. % CNTs, 40 wt. % carbon nanoparticles, 20 wt. % catalyst material, 10 wt % amorphous carbon and graphite, was tested by Kang et al. in thermal energy harvesting [35]. A vertical test cell with a "hot above cold" orientation (Figure 1.9), glass frit separator and electrode separation of 4 cm was employed with T_{hot} = 46.4 ^{o}C and T_{cold} = 26.4 ^{o}C. SWNT electrodes with an area of 0.25 cm^2 were immersed in 0.2 M $K_3Fe(CN)_6/K_4Fe(CN)_6$ electrolyte. The mass power density obtained was around 5.15 W/kg. Commercially available purified SWNT powders (P-SWNT) sourced from Hanwha Nanotech (ASP-100F), refined by thermal and acid treatment (60-70 wt. % nanotubes, 10 wt. % catalyst material, 20 wt. % graphite impurities) was tested by the same group. The mass power density improved by 32 %, generating 6.8 W/kg. Using the same test conditions, commercially available purified MWNT (P-MWNT) having 3-6 walls with a median diameter of 6.6 nm (SMW100, Southwest Nanotechnologies, Inc) and approximately 98 wt. % carbon yielded a

specific power density of 6.13 W/kg. It must be noted that these tests were not done to maximise the power generation capability of the thermocell but to gain further insight into CNT electrodes for thermal energy harvesting. Hence the small electrode separation, low electrolyte concentration and small thermal gradient.

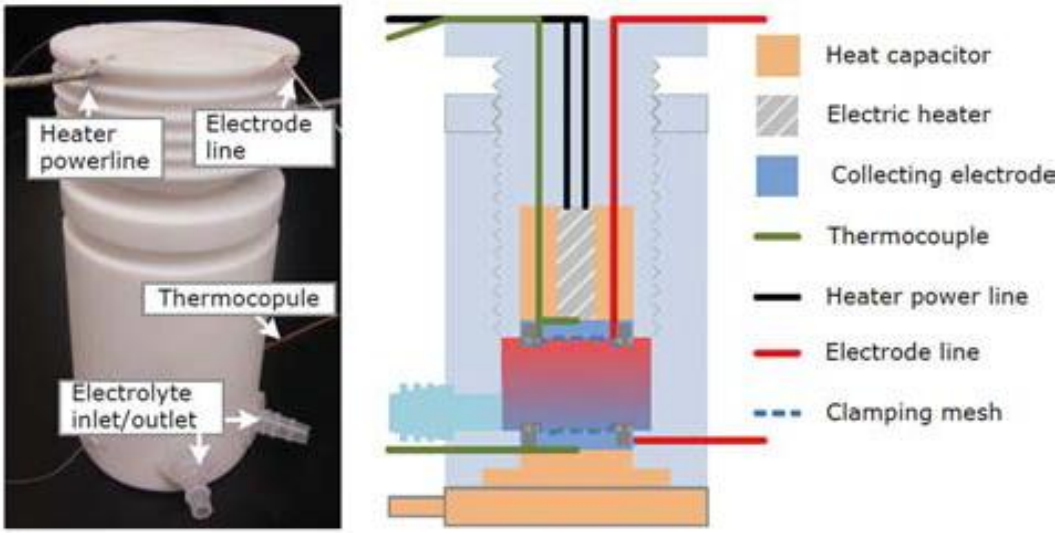

Figure 1.9 Thermocell used by Kang et al. Reprinted from [35] with permission from John Wiley & Sons, Inc.

Electrical impedance spectroscopy (EIS) of the various carbon nanomaterials tested by Kang et al. revealed that the P-SWNT electrode has a marginally lesser ohmic resistance (21 Ω) than pristine SWNT (22 Ω). This decreased ohmic resistance explains the increased specific power density generated when the P-SWNT electrodes are used.

It has been proven that the catalytic nature of MWNTs is due to the edges or sites where the tube terminates, regions that are more numerous in MWNTs than in SWNTs [62]. Due to this and the fact that P-MWNTs had lower ohmic resistance (18 Ω) compared to P-SWNTs, it was expected that P-MWNTs would perform better

in thermal energy harvesting. The authors attributed the enhanced performance of P-SWNT to the larger specific surface area, which compensated for the decreased electroactive sites and higher ohmic resistance.

1.3.3 Functionalised CNTs for thermocell applications

Functionalising or doping (using Nitrogen or Boron atoms) may be used to fine tune the physical and chemical properties of CNTs [63-65]. With advances in technology, CNT functionalisation is a reasonably simple process [66]. Dai et al have shown that nitrogen-doped carbon nanotubes (NCNTs) have high electrocatalytic activity in oxygen reduction reactions as compared to undoped CNTs [67]. They attributed the increase in performance to a four-electron pathway for oxygen reduction reactions that was attained by aligning the nanotubes and integrating nitrogen into the carbon lattice. The additional electrons contributed by nitrogen atoms can enhance electronic conductivity by providing electron carriers for the conduction band [68]. The many active defects and hydrophilic properties of NCNTs allow for enhanced electrolyte interaction in aqueous solutions [69]. Boron-doped CNTs (BCNTs) are also attractive for electrochemical applications owing to the increased edge plane sites on the CNT surface; proven to be the predominant region for electron transfer [70]. Examples of the electrocatalytic performance of BCNTs are the improved detection of L-cysteine, enhanced electroanalysis of NADH and enhancement of field emission [64, 65, 71].

The possibility of using NCNT and BCNT electrodes in thermocells was investigated by Salazar et al. [36]. Doping was attained by using a plasma-enhanced

chemical vapour deposition process. Tests were run using a U-cell configuration similar to that shown in Figure 1.8, thermal gradient of up to 40 ^{o}C wherein T_{cold} = 20 ^{o}C, and electrolyte concentration of 0.1 M $K_3Fe(CN)_6/K_4Fe(CN)_6$. The electrodes were sized to 0.178 cm^2 and were set up in a symmetric and asymmetric (N(hot)-B(cold) and B(hot)-N(cold)) fashion.

Thermocell testing (Figure 1.10) indicated inferior performance for both NCNT and BCNT as compared to Pt and pristine CNTs. Both symmetric and asymmetric configurations of the doped CNTs resulted in lower current density [36].

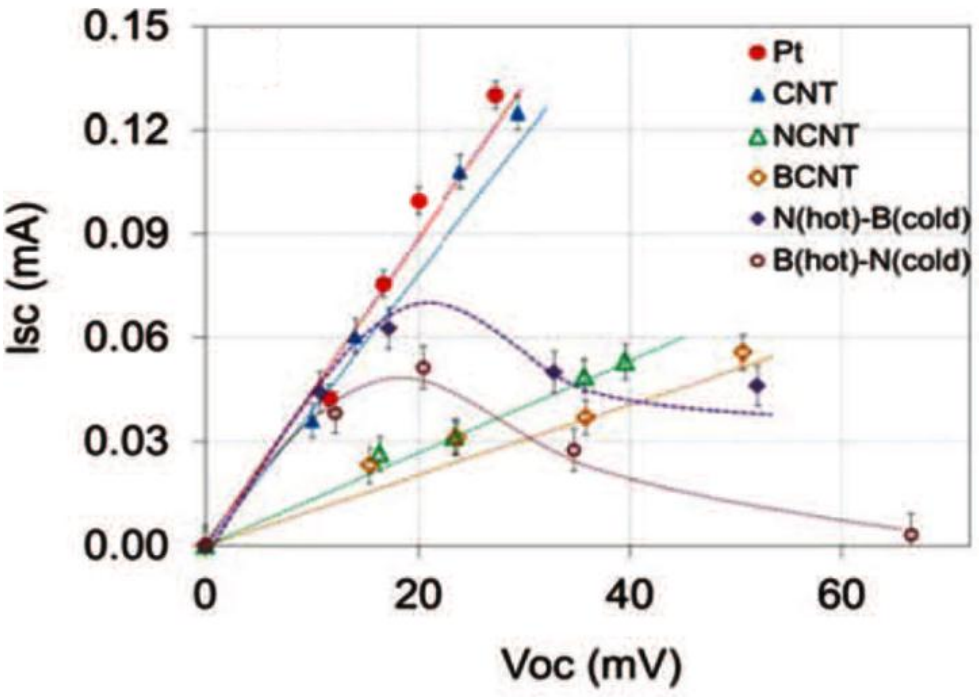

Figure 1.10 I-V curves generated using various electrodes tested by Salazar et al. Reproduced from [36] with permission from The Electrochemical Society.

The poor thermocell performance of the doped CNTs was attributed to the sluggish kinetics, evidenced by the large peak separations in the cyclic voltammograms taken at a scan rate of 100 mV/s (Figure 1.11). It was theorised that the slow-moving

kinetics for the doped electrodes was caused by the electrostatic effects at the electrode-electrolyte interface [72]. The positively charged BCNTs repulsed the similarly charged potassium (K^+) counter ion which decreased the electrolyte concentration in the vicinity of the electrode. The negatively charged NCNTs led to a strong electrostatic attraction with K^+, an effect which at low concentrations can improve electron transfer kinetics. However, the large bulk concentration (needed to achieve significant short circuit currents in thermocells) led to a high density of the K^+ ions in the vicinity of the electrode. This effectively acted as a barrier to the redox reactions that were supposed to occur at the electrode.

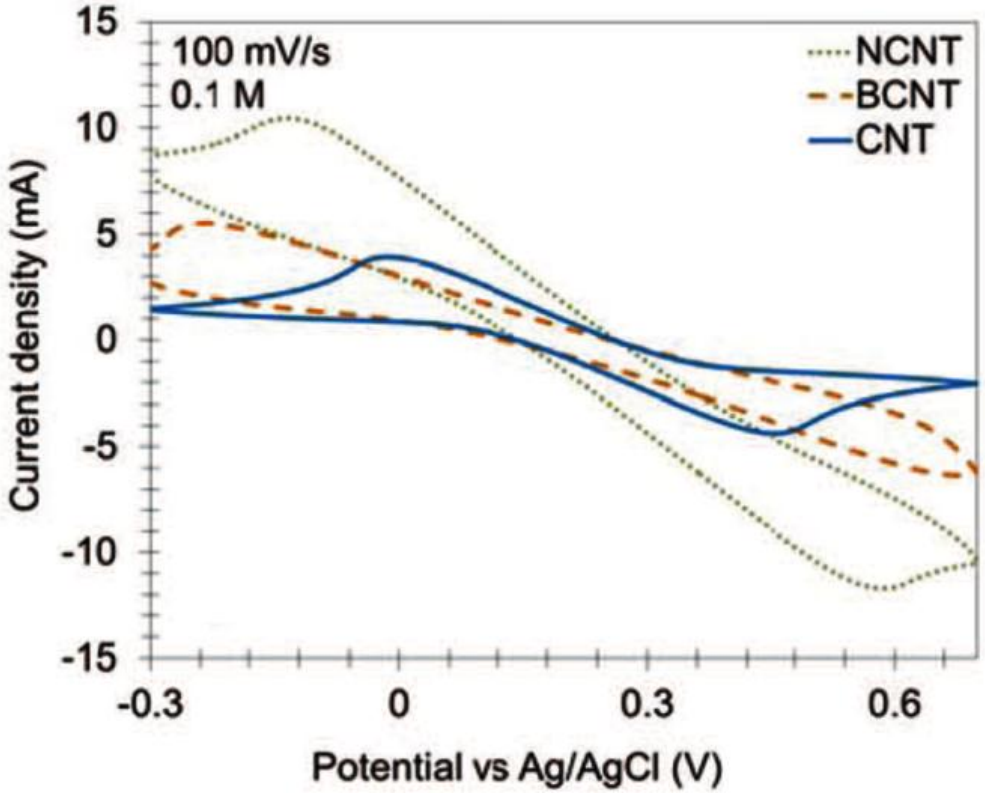

Figure 1.11 Cyclic voltammograms of various electrodes tested by Salazar et al. in 0.1M $K_3Fe(CN)_6/K_4Fe(CN)_6$ run at 100 mV/s vs Ag/AgCl reference electrode. Reproduced from [36] with permission from The Electrochemical Society.

Using BCNT and NCNT in asymmetric configurations resulted in increased currents at small thermal gradients as compared to the symmetric arrangements (Figure 1.10) [36]. This current then decreased non-linearly as the temperature difference was increased. Reaction rates at the cold side of the thermocell would be slightly slower than at the hot side, due to faster kinetics at high temperatures. At small thermal gradients, with the BCNT at the cold side of the cell, the slower kinetics induced an accumulation of reactants at its surface. The faster kinetics at the NCNT, brought about by the increased temperature, kept the electrolyte concentration in its vicinity low. Both factors allow the redox reactions to occur rapidly until a threshold thermal gradient is reached. At this point, the ion concentration in the vicinity of the NCNT is sufficiently large to slow the kinetics and reduce the currents generated. The threshold temperature gradient is attained at lower temperatures when the NCNT is kept at the cold side of the cell because the slower kinetics at this temperature promotes accumulation of K^+ ions on the NCNT surface and leads to the "blocking" effect discussed previously.

1.4 Graphene

A two dimensional material that has been attracting interest, in both experimental and theoretical aspects, from the scientific community is graphene. It consists of a single layer of carbon atoms bonded in a hexagonal/honeycomb lattice (Figure 1.12). Research on this carbon nanostructure reveals that it has a superb combination of thermal, mechanical, optical and electrical properties [73-76]. The attractive characteristics of graphene for electrochemical applications are its charge

carrier mobility of 200 000 cm^2/V-s and specific surface area (SSA) of 2 630 m^2/g [77, 78]. The unique structure of graphene has resulted in extensive research in the fields of energy storage materials [78-80] and other "green" energy related systems [81-84].

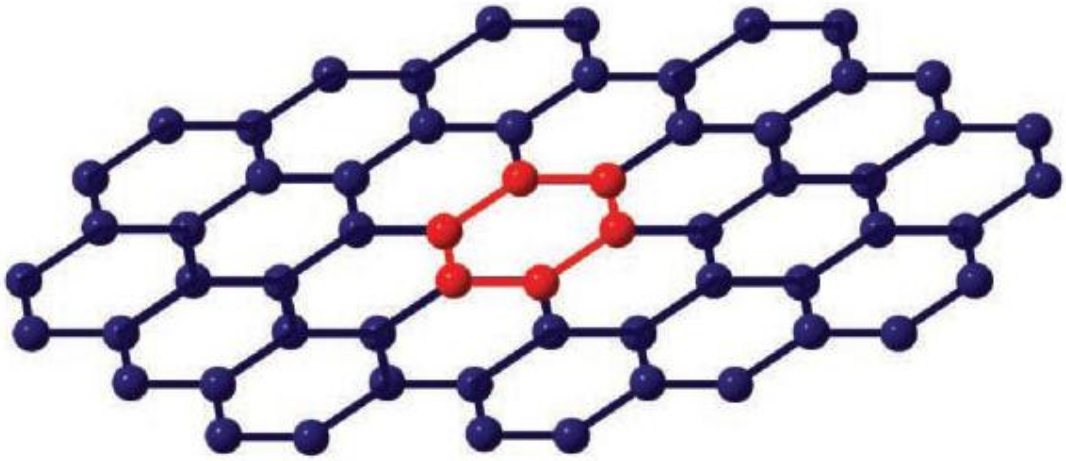

Figure 1.12 Molecular structure of graphene. Reproduced from [85] with permission from John Wiley & Sons, Inc.

Graphene was first fabricated by chemical vapour deposition in the 1970s but it was only recently that real progress was made in this area [86]. Novoselov et al. discovered that micromechanical exfoliation, also known as the "scotch tape" method, allowed monolayers to be peeled from graphite crystals resulting in pristine graphene [87]. This defect-free graphene provided the platform for fundamental studies to be carried out on its properties. With possible applications of pristine graphene in high frequency nanoelectronics [88], Chou et al. improved on the "scotch tape method" through the use of stamps [89]. Said stamps were made of SiO_2/Si pillars prepared via patterned plasma etching which were pressed into graphite substrates. This resulted in cutting and exfoliation of regularly sized

graphene which was then transferred to device active sites on another substrate. However, research on practical applications of graphene demanded large quantities of the material. This need could not be met by micromechanical exfoliation owing to its low yield and throughput. This has prompted scientists to develop methods wherein large scale production of good quality graphene is possible.

One way to scale up graphene production is through exfoliation of graphite in the liquid phase to attain single or few layer sheets [49, 90]. This method results in graphene-like materials with properties similar to pristine graphene. The main problem with liquid phase exfoliation of graphene stems from its high SSA, wherein the van der Waals interactions cause sheets to restack and form graphite [91]. This leads to a loss of the attractive properties associated with graphene. Through processes such as chemical conversion or surfactant/solvent stabilisation of graphite, said problem may be circumvented. The low cost of these solution based processes provides attractive commercial prospects for these graphene-like materials and has been the driving force behind research in these areas. Free standing films for use in electrochemical applications (Figure 1.13) are easily prepared via vacuum filtration.

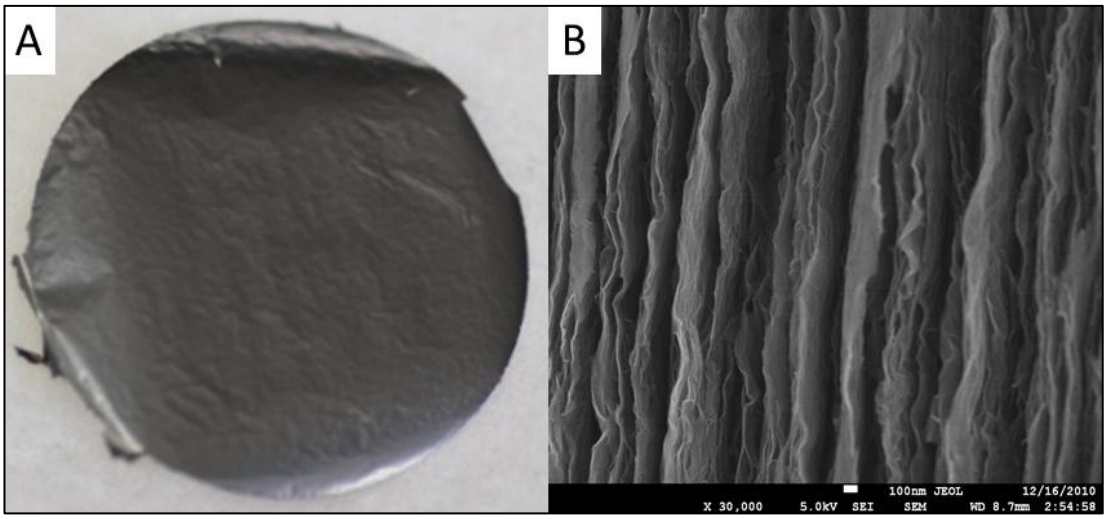

Figure 1.13 A) Free standing film of reduced graphene oxide prepared by vacuum filtration, B) SEM image of the cross-section the film shown in A.

1.4.1 Current processing techniques for graphene relevant to thermocells

1.4.1.1 Chemical conversion of graphene

Chemical conversion of graphene involves three main steps: oxidation of the graphite powder, followed by exfoliation then subsequent reduction of the dispersion. First, graphite powder is oxidized in the presence of strong acids and oxidants, resulting in a material called graphite oxide (GO). GO retains the layered structure of graphite but is lighter in colour owing to the loss of electronic conjugation [92]. To date, several methods for the synthesis of GO have been developed. Said methods are modifications of the three principal methods which were established by Hummers [93], Staudenmire [94], and Brodie [95]. The introduction of oxygen to the graphite stack results in hydroxyl, epoxy, ether, diol, and ketone groups on the basal planes and edges. The lattice disruption is evidenced by the rise in interlayer spacing from 0.335 nm for graphite to 0.625 nm after oxidative treatment [96]. These functional groups make GO hydrophilic by virtue of

their polar nature allowing intercalation of water molecules into the GO layers [92]. This makes exfoliation of GO in aqueous and organic media relatively easy to carry out. Suitable sonication or mechanical mixing can produce dispersions of monolayer or few layers of exfoliated graphene oxide sheets (eGO) [97]. The negative charge of the oxygenated species prevents restacking of the eGO [73]. The degree of surface modification imparted during oxidation dictates the maximum concentration of eGO in solution, a parameter that is critical for further processing.

The functional groups that stabilise eGO in water also make it electrically insulating by disrupting the π-conjugation [49]. Additionally, said functional groups render the eGO thermally unstable [98]. Reducing eGO is one of the more significant reactions owing to the similarities in properties between reduced graphene oxide (rGO) and pristine graphene. To restore the conductivity of eGO to a level similar to that of graphene, chemical or thermal reduction is carried out. Hydrazine monohydrate was one of the first reducing agents to be used to chemically convert eGO [92]. Its widespread use may be attributed to the fact that it does not react strongly with water, making it a feasible option for reducing aqueous dispersions of eGO. Elemental analysis of chemically converted graphene (CCG) reveals that the atomic C:O ratio is around 10:1 [99]. Despite a significant improvement from GO which has a C:O ratio of 2.7:1, a considerable amount of oxygen is present after the reduction step. This implies that CCG is not the same as pristine graphene. In order to facilitate further restoration of the sp^2 carbon network, thermal annealing at elevated temperatures of CCG is carried out [99].

Simultaneous exfoliation and reduction of GO may also be carried out by rapid heating wherein exfoliation of the layers is facilitated by the evaporation of

intercalated water and evolution of gases produced by pyrolysis of the oxygen containing functional groups [100]. Exposing GO to temperatures as high as 1050 ^{o}C have been reported, which generates pressures around 130 MPa within the stacked layers (based on state equations) [91]. Through the use of the Hamaker constant, only 2.5 MPa is needed to separate two stacked GO sheets [91]. A notable disadvantage of thermally mediated exfoliation is the structural damage induced on the rGO sheets, wherein the 30% mass loss of the GO leaves several topological defects [100]. The bulk conductivities measured (1000-2300 S/m) are indicative of effective overall reduction and restoration of the electronic structure [101]

1.4.1.2 Solvent/surfactant-assisted exfoliation of graphene

The main disadvantage of graphene preparation via chemical conversion is the fact that during the oxidation step, the π-orbital structure is disrupted. Despite removal of the oxygen functional groups via reduction, a significant number of defects still remain on the rGO sheets [102, 103]. These defects disrupt the band structure and the resulting rGO has electronic properties inferior to pristine graphene.

Possible methods that circumvent the issues associated with oxidation of graphite are to exfoliate it via stabilisation in organic solvents or surfactant-water solutions. The energy required to disperse graphene via solvent-assisted exfoliation of graphite can be expressed as the enthalpy of mixing per unit volume (Equation 1.14) [104].

$$\frac{\Delta H_{mix}}{V_{mix}} \sim \frac{2}{T_{flake}} (\delta_{graphite} - \delta_{solvent})^2 \phi \qquad \text{Equation 1.14}$$

Wherein T_{flake} is the thickness of the graphene flake, δ is the square root of the surface energy, and ϕ is the graphene volume fraction. The surface energy of graphite is the energy required to peel two sheets apart. Using Equation 1.14 as a basis, solvent-assisted exfoliation of graphite relies on matching the solvent's surface energy with that of graphene. This will minimise the energy required to carry out exfoliation. Coleman et al. tested this by dispersing graphite in a range of solvents followed by mild centrifugation. To determine the amount of graphene, they measured the optical absorbance and converted it to concentration through the use of the absorption coefficient, measured at 660 nm. Their results (Figure 1.14) indicate a peak in concentration after centrifugation at surface tension values around 40 mJ/m^2 [104]; a trend very similar to CNT dispersion (Section 1.3.1.1).

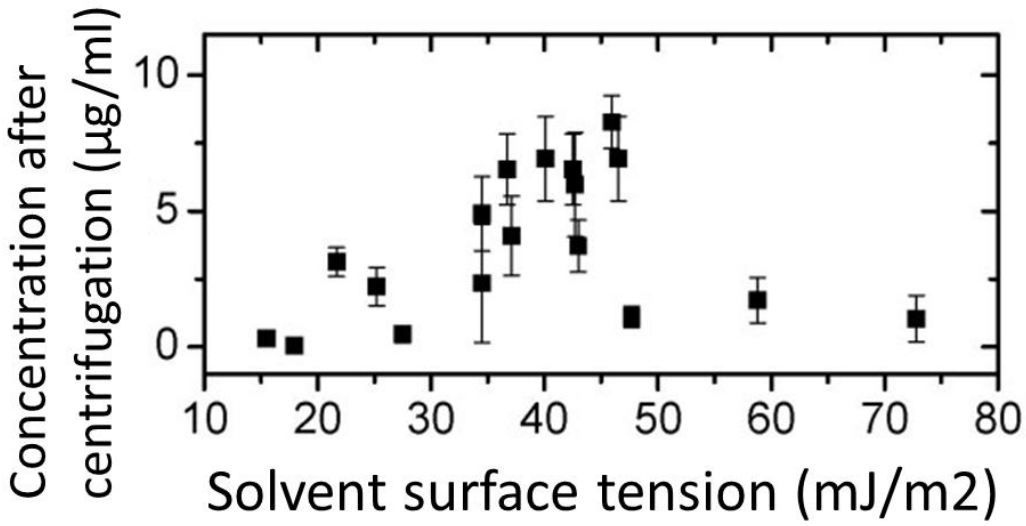

Figure 1.14 Graphene concentration after centrifugation in a variety of solvents. Reproduced from [49] with permission from John Wiley & Sons, Inc.

In order to produce concentrations of graphene that may be sufficient for practical applications, low power bath sonication for extended periods was done by Khan et al.[105]. They utilised an initial solution with a concentration of 3 mg/ml graphite in 700 mL N-methyl-pyrrolidone (NMP). The concentration of dispersed graphene increased from 0.06 mg/ml after 30 minutes of mild sonication to a saturation point of 1.2 mg/ml after 270 hours (Figure 1.15).

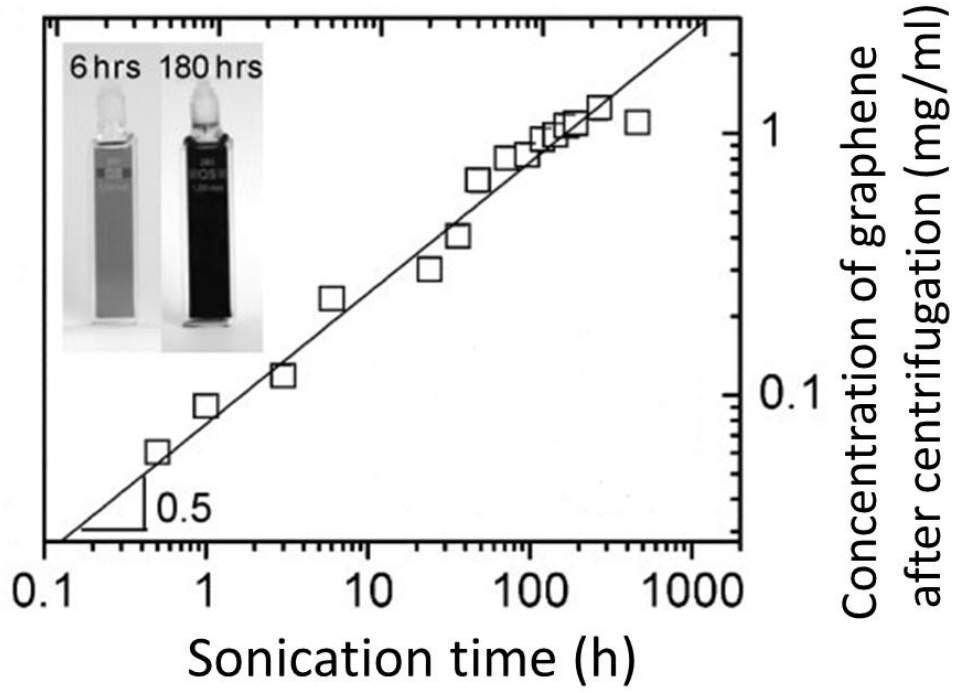

Figure 1.15 Concentration of graphene in NMP after centrifugation as a function of sonication time. Reproduced from [105] with permission from John Wiley & Sons, Inc.

Surfactant-assisted exfoliation of graphene in aqueous media is an alternative route towards graphene synthesis for certain applications wherein high boiling point and toxic solvents may not be suitable. Since water does not have a surface energy around 40 mJ/m^2, said method relies on principles analogous to dispersion of CNTs through the use of surfactants (Section 1.3.1.1). Aqueous solutions of sodium

dodecylbenzene sulphonate (SDBS) and sodium cholate (SC) have been used to effectively exfoliate graphene through the use of low powered bath sonication [106, 107]. The surfactant adsorbs onto the graphene sheets and imparts an effective charge thus stabilising the dispersion by virtue of electrostatic repulsion [106]. For SDBS assisted exfoliation, measurements of the potential at the interface between the stationary layer of fluid attached to the graphene sheet and water; i.e. zeta potential indicates a peak at -44 mV. This is indicative of colloidal stability (beyond -25 mV) and is the reason why said dispersions are stable [106]. Concentrations up to 0.3 mg/ml of graphene dispersions stabilised in water by SC have been reported [74]. Similar to solvent-assisted exfoliation, said concentration was attained after extended periods (up to 400 hours) of low power sonication.

Graphene prepared by both solvent and surfactant assisted exfoliation has shown to be composed of 1-10 stacked monolayers (determined by transmission electron microscopy) and free of oxygen containing functional groups that could disrupt the π-orbital structure. Defects measured by Raman spectroscopy are predominantly edge as opposed to basal plane and are caused by the sonication process; i.e. when graphene sheets are cut creating new edges [74, 105, 106]. Films have been prepared by vacuum filtration onto porous membranes having an average DC conductivity of $1.8 \pm 0.1 \times 10^4$ S/m (Figure 1.16) [105].

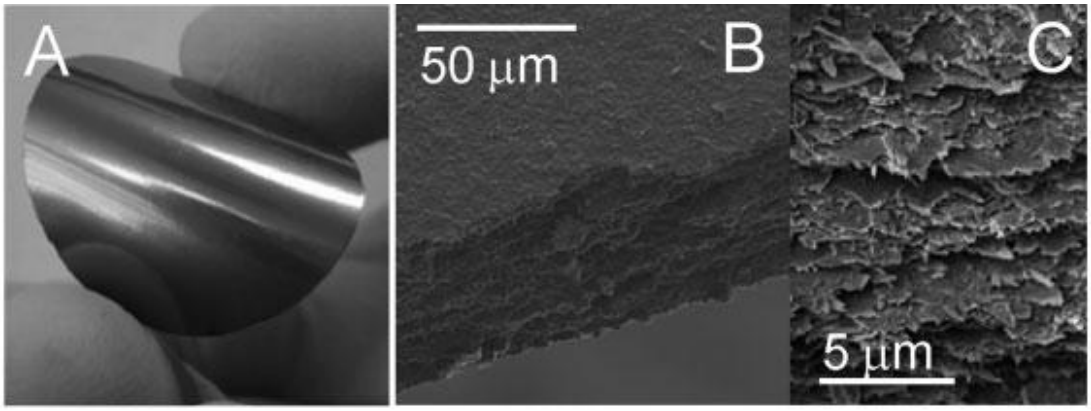

Figure 1.16 A) Free standing film of graphene prepared by solvent-assisted exfoliation, B and C) SEM images of the edge of the film shown in A. Reproduced from [105] with permission from John Wiley & Sons, Inc.

1.4.2 Graphene for thermocell applications

rGO has been shown to have fast electron transfer rates for a variety of redox species. Of note is its performance in the ferri-/ferro-cyanide system that attained a peak separation (anodic/cathodic peaks) in cyclic voltammograms of 65 mV [108]. As mentioned in Section 1.3, said redox couple is important in thermocell applications as it possesses a high Seebeck coefficient.

Recently, Kang et al. investigated the use of rGO as electrode materials for thermocells [35]. They employed the same thermocell (Figure 1.9) and similar conditions (mentioned in Section 1.3.2) for the evaluation of SWNT and P-SWNT as electrodes. Despite the many attractive properties of rGO, it was only able to generate a mass power density of 3.87 W/kg, roughly 57 % less than the value attained through the use of P-SWNT. This could be explained by the high ohmic resistance of rGO measured by EIS, which was 35.6 Ω. The ~55% increase in ohmic resistance (compared to P-SWNT) may be attributed to the residual oxygen

containing functional groups on the rGO lattice. Furthermore, the sheet-like structure of rGO may impede diffusion of the redox couple in and out of the electrode.

1.5 Carbon cloth

Carbon cloth (Figure 1.17) consists of carbon fibres that are woven in the form of cloth [109, 110]. Due to the vascular structure of these materials they possess a large internal surface area. This translates to an increase of electroactive sites per geometric area as compared to a flat electrode. The good electrical conductivity of carbon cloth has led to its use in several electrochemical applications; supercapacitors, biosensors, and biofuel cells to name a few [109, 111-113].

These woven carbon fibres have been used with nano-structured carbon materials in order to further enhance the number of electroactive sites. CNTs and graphene have been successfully deposited on carbon cloth to produce flexible electrodes which exhibit improved performance [109, 114].

Carbon cloth is an attractive support material/scaffold for thermocell electrodes owing to its large electroactive area, low electrical resistance, light weight, high porosity, chemical and thermal stability, good mechanical strength, and high degree of flexibility [115]. A large active area is desired in thermocell applications as it facilitates generation of a high exchange current density between the electrode and electrolyte; which leads to increased power density. The high conductivity is ideal for the electrochemical reactions necessary in thermocell operation as this would minimise the ohmic overpotential between the electrode and electrolyte. The chemical and mechanical stability will ensure that the electrode will

not degrade at the operating conditions of thermocells, particularly at elevated temperatures. The high porosity will facilitate the diffusion of ions in and out of the structure thus lowering the mass transport overpotential [35]. The high degree of flexibility of carbon cloth will allow thermocell devices to be fabricated that may harness waste heat from irregularly shaped surfaces.

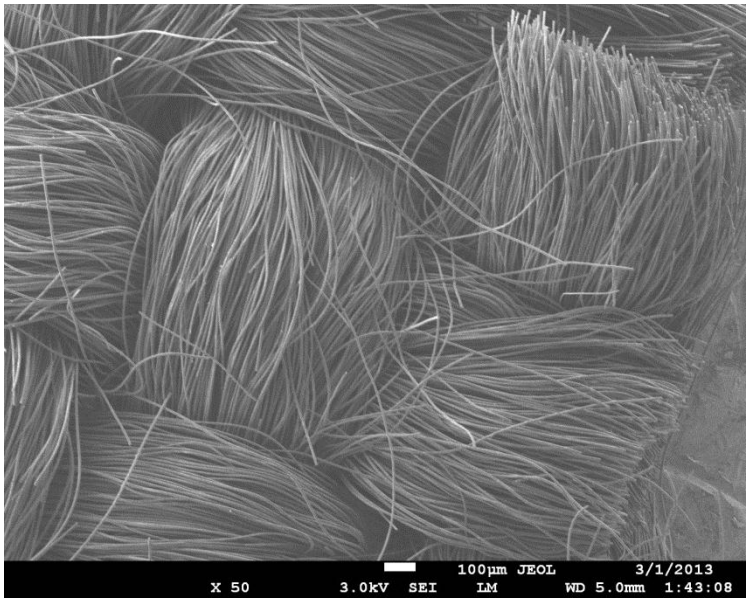

Figure 1.17 SEM image of carbon cloth.

1.6 Thesis objectives

This thesis work aims to develop carbon based electrodes for thermocell applications. The catalytic nature of CNTs and graphene may enable electron transfer rates similar to that of platinum. Concurrently, investigations will be made into the possibility of harnessing the nanostructure of these carbon materials to form porous electrodes on the macro-scale when formed into buckypapers. The use of porous electrodes may afford a larger electroactive area as opposed to the flat surface

of the widely studied platinum electrode. As can be predicted from the Tafel equations, a higher electroactive area would result in an increase in current generation capabilities of the thermocell.

CNTs, particularly SWNTs, are to be exfoliated using organic solvents. This method is selected as it has been shown that only mild sonication is needed to attain stable dispersions of SWNTs, minimising damage done to the tubes by cutting [51]. Graphene synthesis is to be achieved via exfoliation in the liquid phase by both chemical conversion and solvent assisted processes. Said methods are selected owing to their scalability. The synthesised graphene should be highly conductive and the surface area of the sheets should be easily accessible by the electrolyte to facilitate current generation. Composites of SWNTs and graphene will also be investigated in order to optimise the combination of composition and electrode thickness in thermocell applications. Benchmarking of the various carbon electrodes will be done using the widely studied ferri-/ferro-cyanide redox couple in water.

The use of vascular electrode structures to improve the thermopower conversion capabilities of thermocells will also be considered. Decoration of the vascular electrode with nano-carbons will also be investigated. The large internal surface area of vascular structures combined with nano-carbons may provide more sites for electron transfer and result in increased current and power density.

Cell design is an important aspect of thermocell power generation as it directly affects the power conversion efficiency. Another objective in this study is to enhance thermocell performance through the development of new cell and electrode configurations.

1.7 References

1. Kalogirou, S.A., *Solar thermal collectors and applications.* Progress in Energy and Combustion Science, 2004. **30**(3): p. 231-295.
2. Turner, J.A., *A Realizable Renewable Energy Future.* Science, 1999. **285**(5428): p. 687-689.
3. Noam, L., *Energy resources and use: The present (2008) situation and possible sustainable paths to the future.* Energy, 2010. **35**(6): p. 2631-2638.
4. Fronk, B.M., R. Neal, and S. Garimella, *Evolution of the Transition to a World Driven by Renewable Energy.* Journal of Energy Resources Technology, 2010. **132**(2): p. 021009-7.
5. Balat, M., *Security of energy supply in Turkey: Challenges and solutions.* Energy Conversion and Management, 2010. **51**(10): p. 1998-2011.
6. Usher, W. and N. Strachan, *An expert elicitation of climate, energy and economic uncertainties.* Energy Policy, 2013. **61**(0): p. 811-821.
7. Hall, P.J. and E.J. Bain, *Energy-storage technologies and electricity generation.* Energy Policy, 2008. **36**(12): p. 4352-4355.
8. Shukla, A.K., S. Sampath, and K. Vijayamohanan, *Electrochemical spercapacitors: Energy storage beyond batteries.* Current Science, 2000. **79**(29): p. 6.
9. Hall, P.J., et al., *Energy storage in electrochemical capacitors: designing functional materials to improve performance.* Energy & Environmental Science, 2010. **3**(9): p. 1238-1251.

10. Wartsila. *The world's most powerful reciprocating engine*. [cited 2012 May]; Available from: http://www.wartsila.com/en/engines/low-speed-engines/RT-flex96C.

11. Murakami, T., et al., *Thermoelectric Power of M-H Systems in Molten Salts and Application to M-H Thermogalvanic Cell.* Journal of The Electrochemical Society, 2003. **150**(7): p. A928-A932.

12. Wartanowicz, T., *The theoretical analysis of a molten salt thermocell as a thermoelectric generator.* Advanced Energy Conversion, 1964. **4**(3): p. 149-158.

13. Dincer, I., *On thermal energy storage systems and applications in buildings.* Energy and Buildings, 2002. **34**(4): p. 377-388.

14. Bell, L.E., *Cooling, Heating, Generating Power, and Recovering Waste Heat with Thermoelectric Systems.* Science, 2008. **321**(5895): p. 1457-1461.

15. Ujihara, M., G.P. Carman, and D.G. Lee, *Thermal energy harvesting device using ferromagnetic materials.* Applied Physics Letters, 2007. **91**(9): p. 093508-3.

16. Vining, C.B., *An inconvenient truth about thermoelectrics.* Nat Mater, 2009. **8**(2): p. 83-85.

17. Kuzminskii, Y.V., V.A. Zasukha, and G.Y. Kuzminskaya, *Thermoelectric effects in electrochemical systems. Nonconventional thermogalvanic cells.* Journal of Power Sources, 1994. **52**(2): p. 231-242.

18. Quickenden, T.I. and Y. Mua, *The Power Conversion Efficiencies of a Thermogalvanic Cell Operated in Three Different Orientations.* Journal of The Electrochemical Society, 1995. **142**(11): p. 3652-3659.

19. Hertz, H.G. and S.K. Ratkje, *Theory of Thermocells.* Journal of The Electrochemical Society, 1989. **136**(6): p. 1698-1704.

20. Quickenden, T.I. and Y. Mua, *A Review of Power Generation in Aqueous Thermogalvanic Cells.* Journal of The Electrochemical Society, 1995. **142**(11): p. 3985-3994.

21. deBethune, A.J., T.S. Licht, and N. Swendeman, *The Temperature Coefficients of Electrode Potentials: The Isothermal and Thermal Coefficients—The Standard Ionic Entropy of Electrochemical Transport of the Hydrogen Ion.* Journal of The Electrochemical Society, 1959. **106**(7): p. 616-625.

22. Hornut, J.M. and A. Storck, *Experimental and theoretical analysis of a thermogalvanic undivided flow cell with two aqueous electrolytes at different temperatures.* Journal of Applied Electrochemistry, 1991. **21**(12): p. 1103-1113.

23. Shindo, K., M. Arakawa, and T. Hirai, *Effect of non-graphitized carbon electrodes on the electrochemical characteristics of a thermocell with a Br2/Br− redox couple.* Journal of Power Sources, 1998. **70**(2): p. 228-234.

24. Romano, M., et al., *Novel carbon materials for thermal energy harvesting.* Journal of Thermal Analysis and Calorimetry, 2012. **109**(3): p. 1229-1235.

25. Goncalves, R. and T. Ikeshoji, *Comparative studies of a thermoelectric converter by a thermogalvanic cell with a mixture of concentrated potassium ferrocyanide and potassium ferricyanide aqueous solutions at great temperature differences.* J. Braz. Chem. Soc, 1992. **3**(3): p. 4.

26. Hu, R., et al., *Harvesting Waste Thermal Energy Using a Carbon-Nanotube-Based Thermo-Electrochemical Cell.* Nano Letters, 2010. **10**(3): p. 838-846.

27. Bonetti, M., et al., *Huge Seebeck coefficients in nonaqueous electrolytes.* The Journal of Chemical Physics, 2011. **134**(11): p. 114513-8.

28. Agar, J.N. and W.G. Breck, *Thermal diffusion in non-isothermal cells. Part 1.-Theoretical relations and experiments on solutions of thallous salts.* Transactions of the Faraday Society, 1957. **53**(0): p. 167-178.

29. Burrows, B., *Discharge Behavior of Redox Thermogalvanic Cells.* Journal of The Electrochemical Society, 1976. **123**(2): p. 154-159.

30. Quickenden, T.I. and C.F. Vernon, *Thermogalvanic conversion of heat to electricity.* Solar Energy, 1986. **36**(1): p. 63-72.

31. Artjom V, S., *Theoretical study of thermogalvanic cells in steady state.* Electrochimica Acta, 1994. **39**(4): p. 597-609.

32. Anderson L, B., A. Greenberg S, and B. Adams G, *Thermally and Photochemically Regenerative Electrochemical Systems*, in *Regenerative EMF Cells*. 1967, AMERICAN CHEMICAL SOCIETY. p. 213-276.

33. Bockris, J.O.M. and A.K.N. Reddy, *Modern electrochemistry: an introduction to an interdisciplinary area*. 1970: Plenum Press.

34. Mua, Y. and T.I. Quickenden, *Power Conversion Efficiency, Electrode Separation, and Overpotential in the Ferricyanide/Ferrocyanide Thermogalvanic Cell.* Journal of The Electrochemical Society, 1996. **143**(8): p. 2558-2564.

35. Kang, T.J., et al., *Electrical Power From Nanotube and Graphene Electrochemical Thermal Energy Harvesters.* Advanced Functional Materials, 2012. **22**(3): p. 477-489.

36. Salazar, P.F., S. Kumar, and B.A. Cola, *Nitrogen- and Boron-Doped Carbon Nanotube Electrodes in a Thermo-Electrochemical Cell.* Journal of The Electrochemical Society, 2012. **159**(5): p. B483-B488.

37. Iijima, S., *Helical microtubules of graphitic carbon.* Nature, 1991. **354**(6348): p. 56-58.

38. *Chemical biology excercises with carbon nanostructures for the design of intracellular therapeutics*. [cited 2013 03/Feb]; Available from: http://www.biogeo.uw.edu.pl/nukleotyd/archwium/513-chemical-biology-excercises-with-carbon-nanostructures-for-the-design-of-intracellular-therapeutics.

39. Antiohos, D., et al., *Electrochemical investigation of carbon nanotube nanoweb architecture in biological media.* Electrochemistry Communications, 2010. **12**(11): p. 1471-1474.

40. Landi, B.J., et al., *Carbon nanotubes for lithium ion batteries.* Energy & Environmental Science, 2009. **2**(6): p. 638-654.

41. Wang, C., et al., *Proton Exchange Membrane Fuel Cells with Carbon Nanotube Based Electrodes.* Nano Letters, 2003. **4**(2): p. 345-348.

42. Baughman, R.H., A.A. Zakhidov, and W.A. de Heer, *Carbon Nanotubes--the Route Toward Applications.* Science, 2002. **297**(5582): p. 787-792.

43. *Foldvari Group, Research Program: Drug Delivery, University of Waterloo*. [cited 2013 04 Feb]; Available from: https://uwaterloo.ca/foldvari-group/research-program/drug-delivery.

44. Nugent, J.M., et al., *Fast Electron Transfer Kinetics on Multiwalled Carbon Nanotube Microbundle Electrodes.* Nano Letters, 2001. **1**(2): p. 87-91.

45. Peigney, A., et al., *Specific surface area of carbon nanotubes and bundles of carbon nanotubes.* Carbon, 2001. **39**(4): p. 507-514.

46. Inoue, S., et al., *Capillary Condensation of N2 on Multiwall Carbon Nanotubes.* The Journal of Physical Chemistry B, 1998. **102**(24): p. 4689-4692.

47. Eswaramoorthy, M., R. Sen, and C.N.R. Rao, *A study of micropores in single-walled carbon nanotubes by the adsorption of gases and vapors.* Chemical Physics Letters, 1999. **304**(3–4): p. 207-210.

48. Romano, M.S., et al. *Novel Carbon Nanomaterials for Thermal Energy Converters*. in *International Society of Electrochemistry 10th Spring Meeting* 2012. Perth, Australia.

49. Coleman, J.N., *Liquid-Phase Exfoliation of Nanotubes and Graphene.* Advanced Functional Materials, 2009. **19**(23): p. 3680-3695.

50. Bergin, S.D., et al., *Multicomponent Solubility Parameters for Single-Walled Carbon Nanotube−Solvent Mixtures.* ACS Nano, 2009. **3**(8): p. 2340-2350.

51. Bergin, S.D., et al., *Towards Solutions of Single-Walled Carbon Nanotubes in Common Solvents.* Advanced Materials, 2008. **20**(10): p. 1876-1881.

52. Israelachvili, J., *Intermolecular and Surface Forces*. 1991: Academic Press, London.

53. White, B., et al., *Zeta-Potential Measurements of Surfactant-Wrapped Individual Single-Walled Carbon Nanotubes.* The Journal of Physical Chemistry C, 2007. **111**(37): p. 13684-13690.

54. Hunter, R., *Introduction to Modern Colloid Science*. 1994, Oxford: Oxford Science Publications.

55. Sun, Z., et al., *Quantitative Evaluation of Surfactant-stabilized Single-walled Carbon Nanotubes: Dispersion Quality and Its Correlation with Zeta Potential.* The Journal of Physical Chemistry C, 2008. **112**(29): p. 10692-10699.

56. Liu, J., et al., *Fullerene Pipes.* Science, 1998. **280**(5367): p. 1253-1256.

57. Geng, H.-Z., et al., *Absorption spectroscopy of surfactant-dispersed carbon nanotube film: Modulation of electronic structures.* Chemical Physics Letters, 2008. **455**(4–6): p. 275-278.

58. Antiohos, D., et al., *Carbon Nanotubes for Energy Applications*, in *Carbon Nanotubes for Energy Applications, Syntheses and Applications of Carbon Nanotubes and Their Composites*, D.S. Suzuki, Editor. 2013, INTECH.

59. Chen, J., et al., *Flexible, Aligned Carbon Nanotube/Conducting Polymer Electrodes for a Lithium-Ion Battery.* Chemistry of Materials, 2007. **19**(15): p. 3595-3597.

60. Wei, B.Q., et al., *Assembly of Highly Organized Carbon Nanotube Architectures by Chemical Vapor Deposition.* Chemistry of Materials, 2003. **15**(8): p. 1598-1606.

61. Chen, J., et al., *Direct Growth of Flexible Carbon Nanotube Electrodes.* Advanced Materials, 2008. **20**(3): p. 566-570.

62. Banks, C.E., et al., *Investigation of modified basal plane pyrolytic graphite electrodes: definitive evidence for the electrocatalytic properties of the ends of carbon nanotubes.* Chemical Communications, 2004(16): p. 1804-1805.

63. Chun, K.-Y., H.S. Lee, and C.J. Lee, *Nitrogen doping effects on the structure behavior and the field emission performance of double-walled carbon nanotubes.* Carbon, 2009. **47**(1): p. 169-177.

64. Charlier, J.C., et al., *Enhanced Electron Field Emission in B-doped Carbon Nanotubes.* Nano Letters, 2002. **2**(11): p. 1191-1195.

65. Deng, C., et al., *Electrochemical detection of l-cysteine using a boron-doped carbon nanotube-modified electrode.* Electrochimica Acta, 2009. **54**(12): p. 3298-3302.

66. Panchakarla, L.S., A. Govindaraj, and C.N.R. Rao, *Nitrogen- and Boron-Doped Double-Walled Carbon Nanotubes.* ACS Nano, 2007. **1**(5): p. 494-500.

67. Gong, K., et al., *Nitrogen-Doped Carbon Nanotube Arrays with High Electrocatalytic Activity for Oxygen Reduction.* Science, 2009. **323**(5915): p. 760-764.

68. Terrones, M., et al., *N-doping and coalescence of carbon nanotubes: synthesis and electronic properties.* Applied Physics A: Materials Science & Processing, 2002. **74**(3): p. 355-361.

69. Lee, Y.T., et al., *Growth of Vertically Aligned Nitrogen-Doped Carbon Nanotubes: Control of the Nitrogen Content over the Temperature Range 900−1100 °C.* The Journal of Physical Chemistry B, 2003. **107**(47): p. 12958-12963.

70. Banks, C.E. and R.G. Compton, *Exploring the electrocatalytic sites of carbon nanotubes for NADH detection: an edge plane pyrolytic graphite electrode study.* Analyst, 2005. **130**(9): p. 1232-1239.

71. Deng, C., et al., *Boron-doped carbon nanotubes modified electrode for electroanalysis of NADH.* Electrochemistry Communications, 2008. **10**(6): p. 907-909.

72. D. Strmcnik, et al., *The role of non-covalent interactions in electrocatalytic fuel-cell reactions on platinum.* Nat Chem, 2009. **1**(6): p. 466-472.

73. Li, D., et al., *Processable aqueous dispersions of graphene nanosheets.* Nat Nano, 2008. **3**(2): p. 101-105.

74. Lotya, M., et al., *High-Concentration, Surfactant-Stabilized Graphene Dispersions.* ACS Nano, 2010. **4**(6): p. 3155-3162.

75. Lee, C., et al., *Measurement of the Elastic Properties and Intrinsic Strength of Monolayer Graphene.* Science, 2008. **321**(5887): p. 385-388.

76. Nair, R.R., et al., *Fine Structure Constant Defines Visual Transparency of Graphene.* Science, 2008. **320**(5881): p. 1308-1308.

77. Bolotin, K.I., et al., *Ultrahigh electron mobility in suspended graphene.* Solid State Communications, 2008. **146**(9–10): p. 351-355.

78. Stoller, M.D., et al., *Graphene-Based Ultracapacitors.* Nano Letters, 2008. **8**(10): p. 3498-3502.

79. Wu, Q., et al., *Supercapacitors Based on Flexible Graphene/Polyaniline Nanofiber Composite Films.* ACS Nano, 2010. **4**(4): p. 1963-1970.

80. Yoo, E., et al., *Large Reversible Li Storage of Graphene Nanosheet Families for Use in Rechargeable Lithium Ion Batteries.* Nano Letters, 2008. **8**(8): p. 2277-2282.

81. Scheuermann, G.M., et al., *Palladium Nanoparticles on Graphite Oxide and Its Functionalized Graphene Derivatives as Highly Active Catalysts for the Suzuki−Miyaura Coupling Reaction.* Journal of the American Chemical Society, 2009. **131**(23): p. 8262-8270.

82. Robinson, J.T., et al., *Reduced Graphene Oxide Molecular Sensors.* Nano Letters, 2008. **8**(10): p. 3137-3140.

83. Park, S., et al., *Biocompatible, Robust Free-Standing Paper Composed of a TWEEN/Graphene Composite.* Advanced Materials, 2010. **22**(15): p. 1736-1740.

84. Xu, Y., et al., *Three-Dimensional Self-Assembly of Graphene Oxide and DNA into Multifunctional Hydrogels.* ACS Nano, 2010. **4**(12): p. 7358-7362.

85. Wei, D. and Y. Liu, *Controllable Synthesis of Graphene and Its Applications.* Advanced Materials, 2010. **22**(30): p. 3225-3241.

86. Eizenberg, M. and J.M. Blakely, *Carbon monolayer phase condensation on Ni(111).* Surface Science, 1979. **82**(1): p. 228-236.

87. Novoselov, K.S., et al., *Electric Field Effect in Atomically Thin Carbon Films.* Science, 2004. **306**(5696): p. 666-669.

88. Eda, G. and M. Chhowalla, *Graphene Patchwork.* ACS Nano, 2011. **5**(6): p. 4265-4268.

89. Liang, X., Z. Fu, and S.Y. Chou, *Graphene Transistors Fabricated via Transfer-Printing In Device Active-Areas on Large Wafer.* Nano Letters, 2007. **7**(12): p. 3840-3844.

90. Park, S., et al., *Colloidal Suspensions of Highly Reduced Graphene Oxide in a Wide Variety of Organic Solvents.* Nano Letters, 2009. **9**(4): p. 1593-1597.

91. McAllister, M.J., et al., *Single Sheet Functionalized Graphene by Oxidation and Thermal Expansion of Graphite.* Chemistry of Materials, 2007. **19**(18): p. 4396-4404.

92. Stankovich, S., et al., *Synthesis of graphene-based nanosheets via chemical reduction of exfoliated graphite oxide.* Carbon, 2007. **45**(7): p. 1558-1565.

93. Hummers, W.S. and R.E. Offeman, *Preparation of Graphitic Oxide.* Journal of the American Chemical Society, 1958. **80**(6): p. 1339-1339.

94. Staudenmaier, L., *Verfahren zur Darstellung der Graphitsäure.* Berichte der deutschen chemischen Gesellschaft, 1898. **31**(2): p. 1481-1487.

95. Brodie, B.C., *On the Atomic Weight of Graphite.* Philosophical Transactions of the Royal Society of London, 1859. **149**(ArticleType: research-article / Full publication date: 1859 /): p. 249-259.

96. Hontoria-Lucas, C., et al., *Study of oxygen-containing groups in a series of graphite oxides: physical and chemical characterization.* Carbon, 1995. **33**(11): p. 1585-1592.

97. Stankovich, S., et al., *Stable aqueous dispersions of graphitic nanoplatelets via the reduction of exfoliated graphite oxide in the presence of poly(sodium 4-styrenesulfonate).* Journal of Materials Chemistry, 2006. **16**(2): p. 155-158.

98. da Silva, M., et al., *Synthesis and characterization of CeO_2–graphene composite.* Journal of Thermal Analysis and Calorimetry, 2012. **107**(1): p. 257-263.

99. Park, S. and R.S. Ruoff, *Chemical methods for the production of graphenes.* Nat Nano, 2010. **5**(4): p. 309-309.

100. Schniepp, H.C., et al., *Functionalized Single Graphene Sheets Derived from Splitting Graphite Oxide.* The Journal of Physical Chemistry B, 2006. **110**(17): p. 8535-8539.

101. Dreyer, D.R., et al., *The chemistry of graphene oxide.* Chemical Society Reviews, 2010. **39**(1): p. 228-240.

102. Kudin, K.N., et al., *Raman Spectra of Graphite Oxide and Functionalized Graphene Sheets.* Nano Letters, 2007. **8**(1): p. 36-41.

103. Kang, H., et al., *Restoring electrical conductivity of dielectrophoretically assembled graphite oxide sheets by thermal and chemical reduction techniques.* Carbon, 2009. **47**(6): p. 1520-1525.

104. Hernandez, Y., et al., *High-yield production of graphene by liquid-phase exfoliation of graphite.* Nat Nano, 2008. **3**(9): p. 563-568.

105. Khan, U., et al., *High-Concentration Solvent Exfoliation of Graphene.* Small, 2010. **6**(7): p. 864-871.

106. Lotya, M., et al., *Liquid Phase Production of Graphene by Exfoliation of Graphite in Surfactant/Water Solutions.* Journal of the American Chemical Society, 2009. **131**(10): p. 3611-3620.

107. De, S., et al., *Flexible, Transparent, Conducting Films of Randomly Stacked Graphene from Surfactant-Stabilized, Oxide-Free Graphene Dispersions.* Small, 2010. **6**(3): p. 458-464.

108. Tang, L., et al., *Preparation, Structure, and Electrochemical Properties of Reduced Graphene Sheet Films.* Advanced Functional Materials, 2009. **19**(17): p. 2782-2789.

109. Wang, S. and R.A.W. Dryfe, *Graphene oxide-assisted deposition of carbon nanotubes on carbon cloth as advanced binder-free electrodes for flexible supercapacitors.* Journal of Materials Chemistry A, 2013. **1**(17): p. 5279-5283.

110. Hand, R., et al., *The Carbon Cloth Electrode.* Journal of The Electrochemical Society, 1972. **119**(1): p. 74.

111. Wang, S., et al., *Highly porous graphene on carbon cloth as advanced electrodes for flexible all-solid-state supercapacitors.* Nano Energy, 2013. **2**(4): p. 530-536.

112. Barsan, M.M., et al., *Carbon nanotube modified carbon cloth electrodes: Characterisation and application as biosensors.* Electrochimica Acta, 2012. **85**(0): p. 203-209.

113. Haddad, R., et al., *Carbon Cloth/Carbon Nanotube Electrodes for Biofuel Cells Development.* Electroanalysis, 2013. **25**(1): p. 59-67.

114. Liu, N., et al., *Enhanced field emission from three-dimensional patterned carbon nanotube arrays grown on flexible carbon cloth.* Journal of Materials Chemistry, 2012. **22**(8): p. 3478-3484.

115. Chen, Y.-C., et al., *Highly flexible supercapacitors with manganese oxide nanosheet/carbon cloth electrode.* Electrochimica Acta, 2011. **56**(20): p. 7124-7130.

CHAPTER 2

Experimental Theory and Methodologies

2.1 Reagents and Materials

The various reagents, their grade, and company from which the reagents were sourced for use in this study are shown in Table 2.1.

Table 2.1 Various reagents used in this study

Reagent name	Grade	Company
Natural graphite		Bay Carbon
Sulfuric acid	Analytical reagent	Ajax Finechem
Potassium persulfate	ACS reagent	Sigma-Aldrich
Phosphorus pentoxide	ACS reagent	Sigma-Aldrich
Potassium permanganate	ACS reagent	Sigma-Aldrich
Hydrogen peroxide	Analytical reagent	Ajax Finechem
Hydrochloric acid	Analytical reagent	Ajax Finechem
Hydrazine monohydrate	Reagent grade	Sigma-Aldrich
Ammonia	Analytical reagent	Ajax Finechem
Potassium hexacyanoferrate (III)	ACS reagent	Sigma-Aldrich
Potassium hexacyanoferrate (II) trihydrate	ACS reagent	Sigma-Aldrich
Single-walled carbon nanotubes (HiPco)		Continental Carbon Technologies Inc
1-cyclohexyl-2-pyrrolidone	99%	Sigma-Aldrich
Sodium nitrate	Analytical reagent	Ajax Finechem

2.2 Characterisation of materials

A plethora of characterisation techniques were utilised to determine the physical and chemical properties of the materials used in this thesis. Presented in this section are the theory and settings used for each technique.

2.2.1 Four point probe

Sheet resistance measurements of all carbon electrodes were taken using a JANDEL RM3 four point probe (Figure 2.1a). This technique utilises four terminals arranged as shown in Figure 2.1b. The outer pair of probes supplies the current while the inner pair measures the voltage. Through the use of four terminals the impedance contribution of wiring and contact resistance is eliminated (as compared to two point probing, wherein the current and voltage are measured in the same wire) thus increasing the accuracy of this measurement [1].

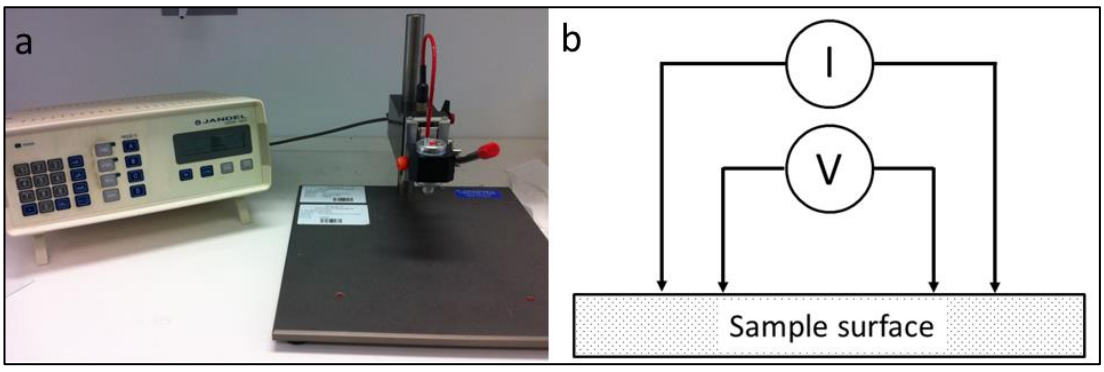

Figure 2.1 a) JANDEL RM3 four point probe, and b) schematic diagram of the operation of the four point probe used

2.2.2 Thermogravimetric analysis

Thermogravimetric analysis (TGA) is a thermal analysis method wherein the mass of a sample is measured (through the use of a precision balance) in response to changes in temperature. The atmosphere in the sample chamber (furnace) and temperature profile; i.e. heating rate, can be modified by the user; depending on the desired data and material being tested. The changes in sample mass may be used to quantify water content and/or chemical functionalities in the material being tested [2]. TGA was done on the GO and CRGO samples in air with a heating rate of 2 ^{o}C/minute from room temperature to 900 ^{o}C using a TA Instruments Q500 TGA (Figure 2.2).

Figure 2.2 TA Instruments Q500 TGA

2.2.3 Ultraviolet-Visible spectroscopy

Ultraviolet-Visible spectroscopy (UV-Vis) involves the use of light in the visible and adjacent ranges to induce changes in a sample's nuclear spin, molecular vibration or electronic states [3]. Said changes occur due to the absorption of certain wavelengths of light. When photons of visible or near ultraviolet are absorbed by molecular species, electronic transitions occur, i.e. electrons move from the ground (or lower) states to excited states. The amount of light/number of photons absorbed is dictated by the concentration of species able to absorb the light [4]. The Beer-Lambert law (Equation 2.1) provides a good correlation between sample concentration and intensity of absorption for a given path length [5].

$$A = log\frac{I_o}{I} = \varepsilon bc \qquad \text{Equation 2.1}$$

Where A is the absorbance, I_o is the intensity of light entering the solution, I is the light intensity leaving the solution, ε is the molar absorptivity, b is the path length in cm and c is the molar concentration.

UV-Vis was carried out on the GO, CRGO and rGO dispersions using a Shimadzu UV-1800 spectrophotometer (Figure 2.3).

Figure 2.3 Shimadzu UV-1800 UV-Vis spectrophotometer. Image courtesy of Shimadzu Corporation, Kyoto, Japan [6]

2.2.4 Thermal conductivity analyser

Thermal conductivity of samples was measured using a TCi Thermal Conductivity Analyzer (Figure 2.4). This instrument uses a modified transient plane source technique to rapidly determine thermal conductivity in a non-destructive fashion. The sample is placed in contact with the instrument's sensor, whereupon a predetermined current is applied to the sensor's heating element. The heat generated causes a rise in temperature (typically smaller than 2 ^{o}C) at the sample-sensor interface. This increase in temperature induces variations in the voltage drop of the sensor element. The rate at which the sensor voltage increases is used to measure the thermal properties of the sample. For example: a highly thermally insulative material would have a steeper voltage rise [7].

Figure 2.4 TCi Thermal conductivity analyzer

2.2.5 Solution electrical conductivity

Solution conductivity is determined by measuring the AC resistance between two electrodes. The TPS smartCHEM-Lab (Figure 2.5) was used to measure the conductivity of various electrolyte solutions at room temperature [8].

Figure 2.5 TPS smartCHEM-Lab. Adapted from [9]

2.2.6 Rheometer

The response or how a liquid or slurry flows upon application of forces can be ascertained by a rheometer. There are two general types of rheometers: rotational or shear rheometers (the applied shear stress or shear strain is controlled) and extensional rheometers (that apply extensional stress or extensional strain). The former was employed in this study using the cone and plate method to determine the viscosity of various electrolytes (AR-G2 rheometer) [10]. The cone used had a diameter of 40 mm and a 2^{o} cone angle (Figure 2.6).

Figure 2.6 AR-G2 rheometer

2.2.7 Raman spectroscopy

The Raman effect occurs when light impinges upon a molecule and said molecule is excited from the ground state to a virtual energy state. A photon is emitted by the molecule when it relaxes, whereupon it returns to a different

rotational or vibrational state. The emitted photon will have a different frequency as compared to the excitation wavelength due to the energy gradient between the original and new state. Raman spectroscopy uses this principle to obtain information on the rotational, vibrational, and other lower frequency modes of a sample. It must be noted that inelastic scattering of monochromatic light is the basis of these measurements (Figure 2.7). Elastic or Rayleigh scattering is used for calibration of the Raman system.

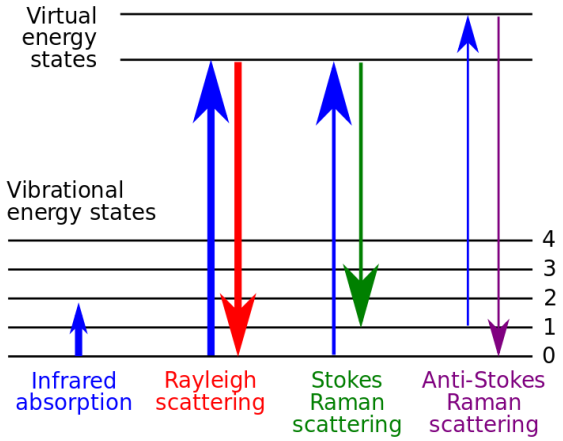

Figure 2.7 Schematic of the states involved in Raman spectroscopy. Adapted from [11]

The Raman spectra (Figure 2.8) for various sp^2 based carbon materials have peaks that are quite similar. For SWNTs, the first vibrational responses (known as the RBM peaks) are induced by the radial expansion and contraction (aka breathing) of the tubes/bundles of tubes and appear between 100 cm^{-1} and 400 cm^{-1} [12, 13]. The concentric layers which make up MWNTs dampen vibrations between 100 cm^{-1} and 400 cm^{-1}, which is why the RBM peaks do not appear in the Raman spectra of MWNTs [14]. The peak that appears between wavelengths of 1300 cm^{-1} and

1400 cm^{-1} is known as the disorder or D band, and corresponds to sp^3 carbons within the material. The peak between wavelengths of 1550 cm^{-1} and 1610 cm^{-1} is induced by the sp^2 carbons in the sample and is named the graphitic or G band [15, 16]. The ratio between the D and G band provides insight as to the amounts of sp^3 and sp^2 carbons present; i.e. a lower D:G ratio indicates less defects are present in the carbon sample [17]. The peak around 2700 cm^{-1} (G') is the second harmonic of the D band [15, 16].

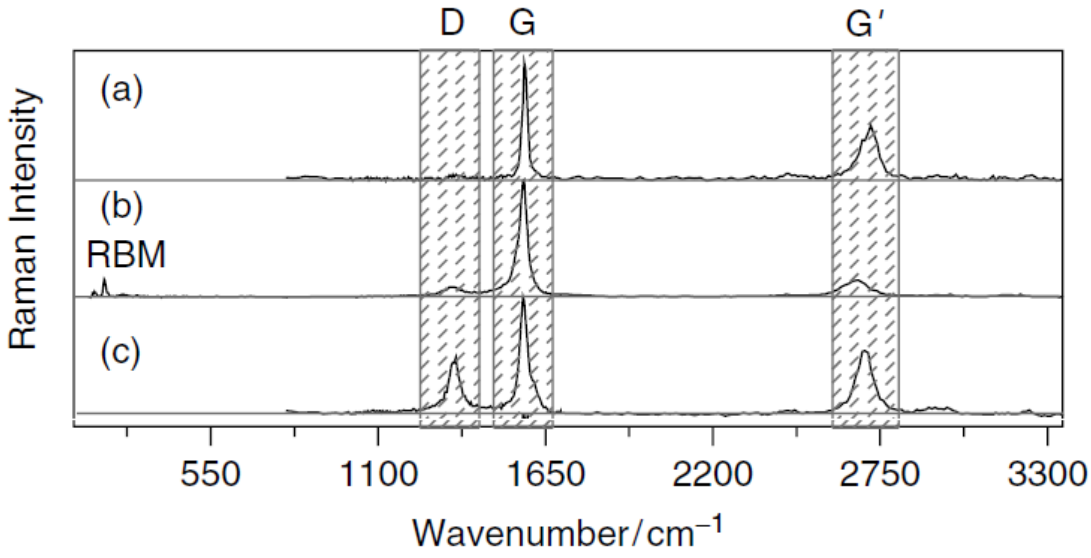

Figure 2.8 Raman spectra of a) graphite, b) single-, and c) multi-walled carbon nanotubes. Adapted from [18] with permission from John Wiley & Sons, Inc.

The surface functionalities of the various carbon materials used in this study were probed using a Jobin Yvon HR800 confocal Raman spectrometer (Figure 2.9) with a 632.8 nm diode laser excitation on a 300 lines/mm grating. A 50x magnification wide angle objective was used. A SiO_2 signal was used to calibrate the 632.8 nm laser.

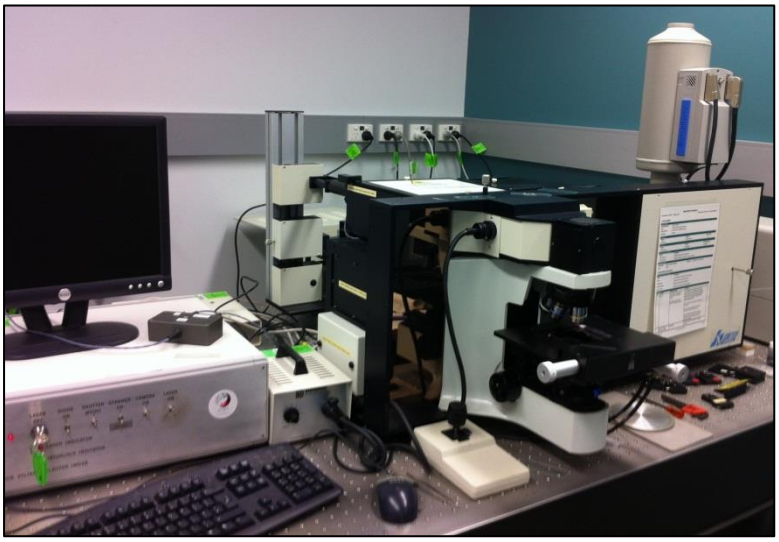

Figure 2.9 Jobin Yvon HR800 confocal Raman spectrometer

2.2.8 Scanning electron microscopy

A scanning electron microscope (SEM) uses a beam of electrons to obtain information on a sample's surface morphology and composition [19]. The beam is scanned in a raster pattern along the sample. Signals generated from the interaction between the electrons and atoms of the sample are collected and used to produce an image [20].

A Jeol7500 field emission scanning electron microscope (Figure 2.10) was used to study the morphology of the various carbon materials used. Typical setting utilised were an accelerating voltage of 3 kV, probe current of 8 mA, and a working distance between 3 to 8 mm. Samples were adhered to the sample holder using double-sided conductive carbon tape and silver paste.

Figure 2.10 Jeol7500 field emission scanning electron microscope

2.2.9 Cyclic voltammetry

An electroanalytical technique employed to probe the redox behaviour of the various electrodes used in this study is cyclic voltammetry (CV). It involves sweeping the potential of the working electrode back and forth between two pre-set values (Figure 2.11). The working electrode is normally the electrode being investigated and its potential is controlled relative to a reference electrode. The current at the working electrode is measured during the potential scan. A third electrode, called an auxiliary or counter electrode, is used to protect the reference electrode from excessive amounts of current [21]. CV can be used to obtain qualitative information on electrode reaction mechanisms as well as quantitative data on charge transfer reactions.

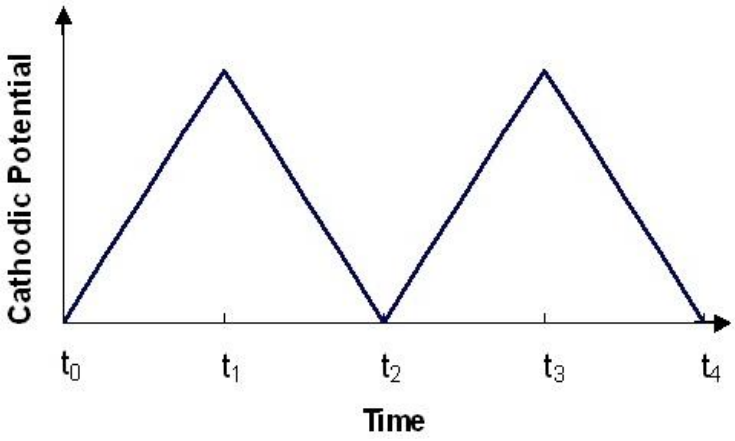

Figure 2.11 Typical potential waveform used in cyclic voltammetry. Adapted from [22]

An EDAQ Potentiostat e-corder 401 (Figure 2.12) was used to perform CV in 0.01 M $K_3Fe(CN)_6$ with 0.1 M $NaNO_3$ as the supporting electrolyte in de-ionised water. The potential was measured against a Ag/AgCl reference electrode at room temperature. A three-electrode setup was employed with a high surface area platinum mesh set as the counter electrode. Data analysis was carried out using eDaq EChem software V 2.0.7.

Figure 2.12 EDAQ Potentiostat e-corder 401

2.10 Plasma treatment

Surface modification of all the electrodes used in this study was achieved through the use of a PDC plasma cleaner (Figure 2.13). Plasma, the fourth state of matter, is a partially ionised gas that is composed of neutral atoms, ions and electrons. Plasma treatment may be used to clean, activate, or modify surfaces depending on the process gas employed. One advantage of this method is that it only affects the surface of a material and bulk properties remain unchanged [23]. Through the use of air and a 20 minutes plasma treatment duration, the surface of the electrode was made hydrophilic. This allowed the aqueous based electrolyte to readily interact with the electrode surface (a detailed discussion on this is presented in Section 2.3 of this chapter).

Figure 2.13 PDC plasma cleaner

2.2.10 Contact angle goniometer

The wettability of a solid surface is quantified by its contact angle (Θ_c). It is measured through the liquid at the three phase boundary where solid, liquid, and gas interact, as shown in Figure 2.14 [24]. It is strongly dependent on the interfacial tensions between the three interfaces involved and can be expressed as shown in Equation 2.2:

$$\gamma_{SG} = \gamma_{SL} + \gamma_{LG}\cos\theta_C \qquad \text{Equation 2.2}$$

Where $\gamma_{SG}$is the interfacial tension between solid and gas, $\gamma_{SL}$is the interfacial tension between solid and liquid, $\gamma_{LG}$is the interfacial tension between liquid and gas. A lower contact angle indicates a greater degree of hydrophilicity of the solid surface.

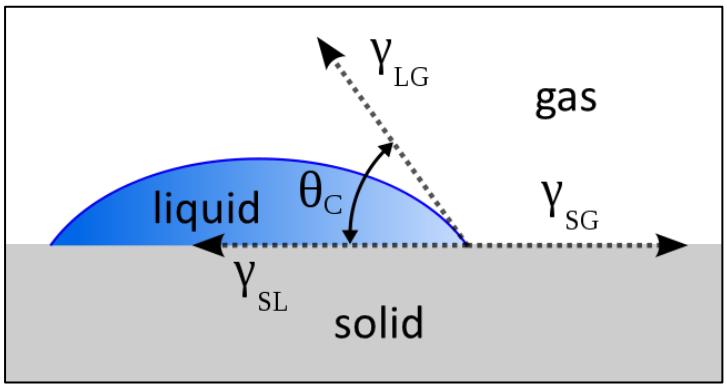

Figure 2.14 A schematic of a contact angle measurement showing the three phase boundary where solid, liquid, and gas interact. Adapted from [25]

A dataphysics OCA contact angle goniometer was used to measure the static contact angle of water on the surface of the various carbon electrodes used. This was to ensure that the electrodes used were of a maximum degree of hyrophilicity, thus ensuring maximum interaction with the electrolyte.

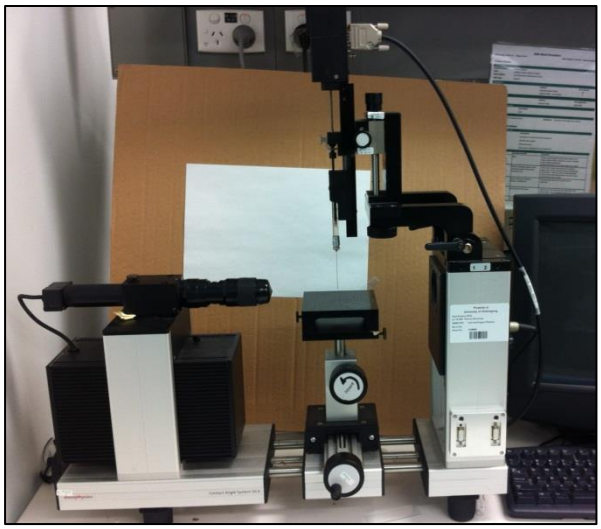

Figure 2.15 Dataphysics OCA contact angle goniometer

2.2.11 Contact profilometer

To accurately determine the thickness of electrodes used, a VeecoDektak 150 (Figure 2.16) stylus profilometer was employed. It involves placing a stylus in contact with the surface of the sample then moving it laterally for a specific distance (beyond the edge of the sample). The change in vertical position of the stylus as it is being moved laterally gives the height of the electrodes.

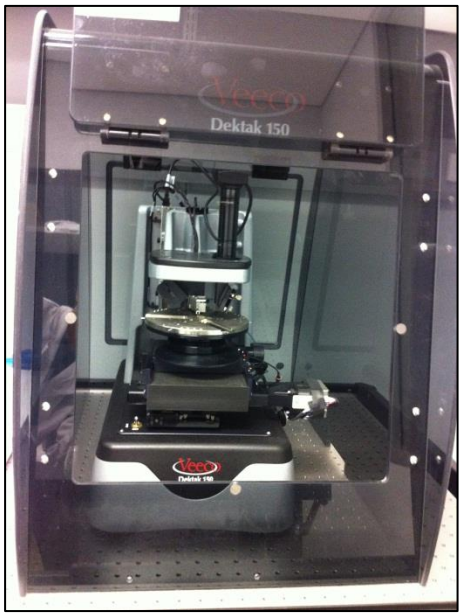

Figure 2.16 VeecoDektak 150 stylus profilometer

2.2.12 Electrochemical impedance spectroscopy

Electrochemical impedance spectroscopy (EIS) was used in this study to complement the data obtained via CV. This method involves applying an alternating current potential to the working electrode and measuring the current response. Small excitation signals are used (1 to 10 mV) to induce a response that is pseudo-linear [26]. This is important as linear or pseudo-linear systems exhibit a sinusoidal current response at the same frequency to a sinusoidal applied potential albeit at a different phase (Figure 2.17) [27]. Information on the electrochemical processes occurring within the cell is extracted from the changes in phase shift that occur at different frequencies [28, 29].

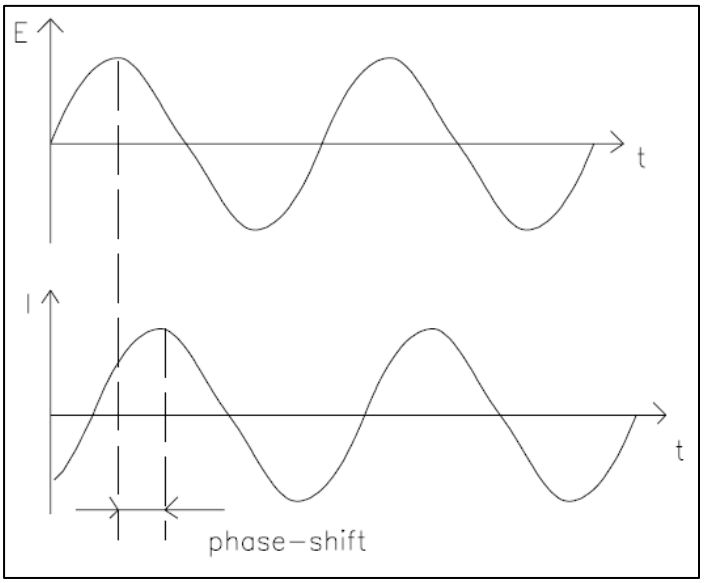

Figure 2.17 Sinusoidal current response showing a phase shift in response to a sinusoidal applied potential Adapted from [26]

For this study, EIS was used to quantify resistive properties of the various electrodes used. A Gamry Instruments V.5.58 was employed in the frequency range of 100 kHz-10 mHz with an AC amplitude of 10 mV. Three-electrode tests were run at room temperature with a Ag/AgCl reference electrode and platinum mesh counter electrode. The electrolyte used was 0.01 M $K_3Fe(CN)_6$ with 0.1 M $NaNO_3$ as the supporting electrolyte in de-ionised water.

2.2.13 Thermocell testing

For thermal energy harvesting experiments, heat was applied to one half of the cell through the use of an Omegalux Rope Heater FGR-060 connected to a TCA Control Box (accuracy ± 1 ^{o}C) that has 48 x 48 Controller with PID control action and 25 amp Solid State relay (Figure 2.18a). The other half of the thermocell was cooled using circulating liquid supplied by a Thermoline Scientific BL-30

refrigerated circulating bath (Figure 2.18b). The temperature was monitored using a Omega HH801 hand held digital thermometer (Figure 2.18c) with a resolution of 0.1 ^{o}C. PFA coated Type K thermocouples (Omega) were used in conjunction with said thermometer.

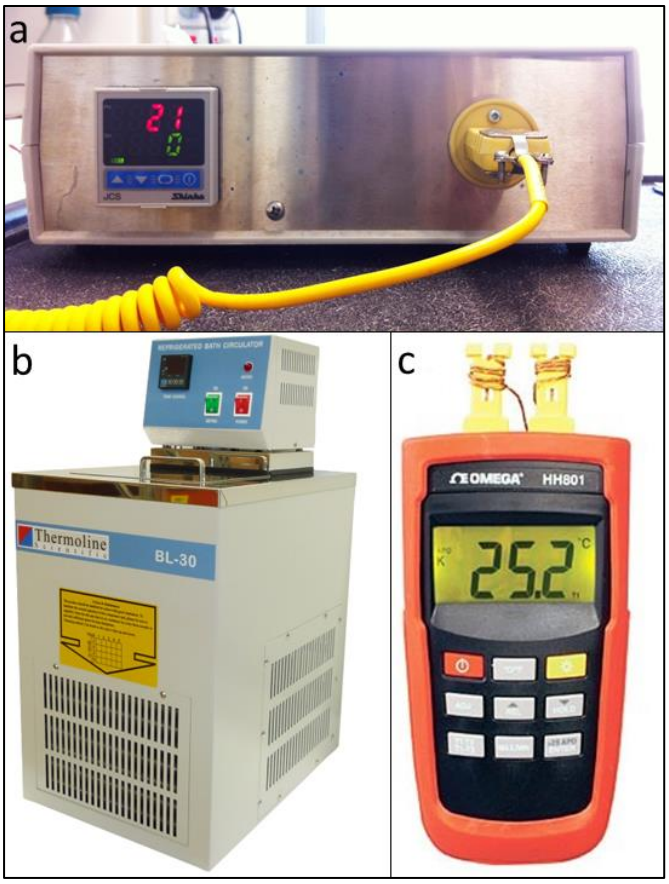

Figure 2.18 a) TCA Control Box used to control the heating coil temperature, b) Thermoline Scientific BL-30 refrigerated circulating bath. Adapted from [30]. c) Omega HH801 digital thermometer. Adapted from [31].

Current density-Voltage (J-V) curves were generated using a Keithley 2400 sourcemeter (Figure 2.19) and customised LabView software.

Figure 2.19 Keithley 2400 sourcemeter

2.3 Reducing hydrophobicity of electrodes

All electrodes used in this study were subjected to plasma treatment prior to use in aqueous electrolytes. This is to ensure that interaction between the electrode and electrolyte was maximised. The typical change in contact angle of a carbon electrode (chemically reduced graphene oxide) with plasma treatment is shown in Figure 2.20. After 20 minutes the contact angle is zero, implying maximum wettability of the carbon films. To verify that the plasma treatment was not degrading the structure of the carbon electrode, thus making it insulating, the sheet resistance was monitored. As can be seen in Figure 2.20, the sheet resistance remains unchanged despite prolonged plasma treatment.

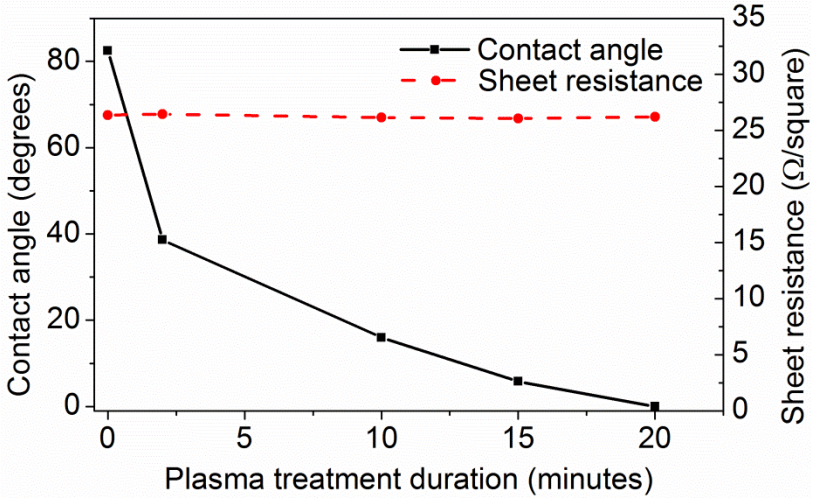

Figure 2.20 Changes in contact angle and sheet resistance with respect to plasma treatment duration for a chemically reduced graphene oxide film.

2.4 3D printing of thermocells (applied in Chapter 4)

3D printing is an additive manufacturing process that can be used to quickly fabricate a physical part or assembly. This technique of rapid prototyping starts off with geometric data as a 3D solid, generated using computer aided design (CAD) software. The 3D printer then "slices" the geometric model into layers, which are then scanned into lines generating 2D drawings. These drawings will be the path with which the machine follows when it lays down successive layers of liquid, powder, etc in order to build up the physical model. These layers are automatically joined during the manufacturing process thus creating the finished product [32].

An Objet Connex 350 (Figure 2.21) was used to print custom designed thermocells. This 3D printer uses the Polyjet technology which is analogous to inkjet document printing. However instead of using ink, a layer of photopolymer (MED 610 was used in this study) is jetted onto the build tray, which is then cured by UV light. These layers are built up one at a time to create the 3D model [33].

Figure 2.21 Objet Connex 350 used to print thermocells

2.5 Exfoliation of SWNT and reduced graphene oxide (applied in Chapter 5)

SWNT and reduced graphene oxide (rGO) were dispersed in 1-cyclohexyl-2-pyrrolidone (CHP). CHP was selected as only mild sonication conditions are necessary in order to facilitate SWNT exfoliation thus reducing the damage to the tubes by cutting [34]. 10 mg of SWNT or rGO powder was weighed out and oven dried at 100 ^{o}C overnight. Removal of moisture from the nano-carbon powder is critical to attain a high degree of exfoliation. 10 ml of CHP was then added to the dried nano-carbon. The dispersion was then subjected to probe sonication (Branson probe sonifier, Figure 2.22a) for 30 minutes using a microtip (Figure 2.22b) at 30 % amplitude and 1 sec on, 1 sec off pulse settings. Bath sonication (Branson B1500R-MT, Figure 2.22c) was then used for 1 hour wherein a recirculating pump was used

for cooling the vessel to ensure that the sample did not heat up. The sample was then exposed to probe sonication again, using the same settings mentioned previously.

Figure 2.22 a) Branson digital probe sonifier controller and b) microtip. c) Branson B1500R-MT bath sonicator

The dispersion was left overnight to allow re-agreggation to occur after which mild centrifugation (Eppendorf Centrifuge 5415 D, Figure 2.23) was done for 90 minutes at 2500 rcf to remove large aggregates. Determination of the concentration of the supernatant is discussed in the next section.

Figure 2.23 Eppendorf Centrifuge 5415 D

2.6 Determination of carbon dispersion concentration (applied in Chapter 5)

The concentration of the SWNT and rGO dispersions after centrifugation was determined via UV-vis. Various material characteristics may be determined from the absorption of light through the use of the Beer-Lambert law (Equation 2.1).The absorbance at 660 nm of SWNT dispersions of known concentration was measured by Giordani et al. They determined α_{660} to be 3264 ml/mg-m [35].

The UV-vis spectra of various rGO dispersions is shown in Figure 2.24A. The absorbance per unit length of said rGO dispersions was measured at a wavelength of 550 nm. The extinction coefficient was determined to be 27 421 ml/mg-m.

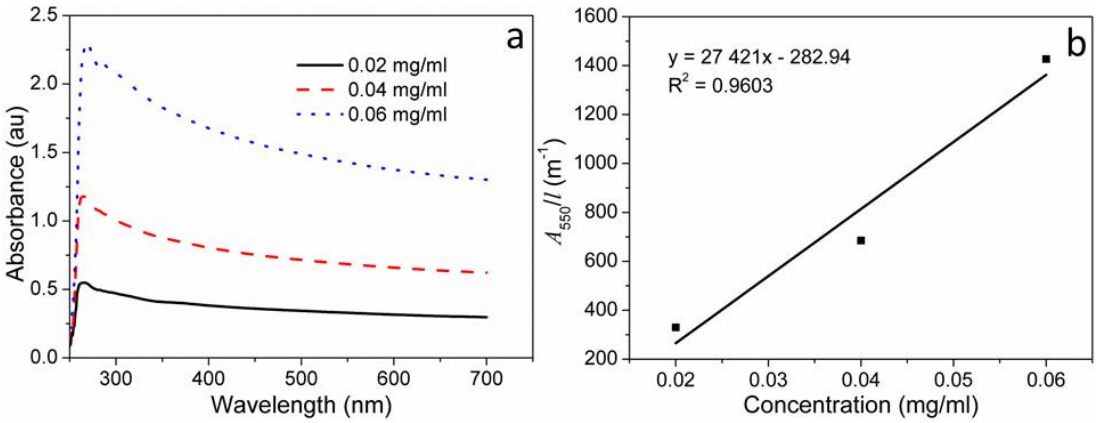

Figure 2.24 a) UV-vis spectra of rGO dispersions, and b) absorbance per unit length measured at $\lambda = 550$ nm

2.7 References

1. microworld. *Four point probe measurement*. [cited 2013 21 May]; Available from: http://www.four-point-probe.eu/#/welcome/3241794.
2. PerkinElmer. *TGA-A Beginners Guide*. [cited 2013 21 May]; Available from: http://www.perkinelmer.com/CMSResources/Images/44-74556GDE_TGABeginnersGuide.pdf.
3. Reusch, W. *Visible and Ultraviolet Spectroscopy*. 2013 [cited 2013 May]; Available from: http://www2.chemistry.msu.edu/faculty/reusch/virttxtjml/spectrpy/uv-vis/spectrum.htm.
4. Reusch, W. *UV-Visible Spectroscopy*. 2013; Available from: http://www2.chemistry.msu.edu/faculty/reusch/virttxtjml/spectrpy/uv-vis/uvspec.htm#uv1.
5. Skoog, D., D. West, and J. Holler, *Fundamentals of Analytical Chemistry*. 7th ed. 1996: Saunders College Publishing.

6. Shimadzu. *UV-1800 UV-Vis Spectrophotometer*. 2012 [cited 2013 June]; Available from: http://www.ssi.shimadzu.com/products/product.cfm?product=uv1800.

7. *C-Therm Technologies Ltd.C-Therm Technologies-Products*. Available from: http://www.ctherm.com/products/tci_thermal_conductivity

8. TPS. *smartCHEM-Lab operators manual*. 2002 [cited 2013 May]; Available from: http://www.tps.com.au/handbooks/smartCHEM_LABv1_01.pdf.

9. Ltd, T.P. *TPS Products*. 2013 [cited 2013 June]; Available from: http://www.tps.com.au/products/combination/smartchem-lab_image.htm.

10. Instruments, T. *ARES-G2 Rheometer*. 2013; Available from: http://www.tainstruments.com/product.aspx?id=29&n=1&siteid=11.

11. *Raman spectroscopy*. 2013 [cited 2013 May]; Available from: http://en.wikipedia.org/wiki/Raman_spectroscopy.

12. Dresselhaus, M.S., et al., *Raman spectroscopy of carbon nanotubes.* Physics Reports, 2005. **409**(2): p. 47-99.

13. Salzmann, C.G., et al., *The Role of Carboxylated Carbonaceous Fragments in the Functionalization and Spectroscopy of a Single-Walled Carbon-Nanotube Material.* Advanced Materials, 2007. **19**(6): p. 883-887.

14. Yu, Z. and L. Brus, *Rayleigh and Raman Scattering from Individual Carbon Nanotube Bundles.* The Journal of Physical Chemistry B, 2001. **105**(6): p. 1123-1134.

15. Dresselhaus, M.S., et al., *Raman spectroscopy on one isolated carbon nanotube.* Physica B: Condensed Matter, 2002. **323**(1–4): p. 15-20.

16. Rao, A.M., et al., *Diameter-Selective Raman Scattering from Vibrational Modes in Carbon Nanotubes.* Science, 1997. **275**(5297): p. 187-191.

17. Khan, U., et al., *High-Concentration Solvent Exfoliation of Graphene.* Small, 2010. **6**(7): p. 864-871.

18. Santangelo, S., et al., *Evaluation of crystalline perfection degree of multi-walled carbon nanotubes: correlations between thermal kinetic analysis and micro-Raman spectroscopy.* Journal of Raman Spectroscopy, 2011. **42**(4): p. 593-602.

19. Schweitzer, J. *Scanning Electron Microscope*. 2013 [cited 2013 May]; Available from: http://www.purdue.edu/rem/rs/sem.htm.

20. Mogk, D. *Scanning Electron Microscopy*. 2012 [cited 2013 May]; Available from: http://serc.carleton.edu/research_education/geochemsheets/techniques/SEM.html.

21. Kissinger, P.T. and W.R. Heineman, *Cyclic voltammetry.* Journal of Chemical Education, 1983. **60**(9): p. 702.

22. *Cyclic Voltammetry*. 2013 [cited 2013 May]; Available from: http://en.wikipedia.org/wiki/Cyclic_voltammetry.

23. Plasma, H. *About Plasma: General Plasma Information*. 2011 [cited 2013; Available from: http://www.harrickplasma.com/plasma.php.

24. Associates, O.R. *Contact Angle Measurement System*. Available from: http://www.orbitresearch.org/contact-angle-measurement-system.html.

25. *Goniometer*. 2013 [cited 2013 May]; Available from: http://en.wikipedia.org/wiki/Goniometer.

26. Instruments, G. *Basics of Electrochemical Impedance Spectroscopy*. 2010 [cited 2013 May]; Available from: http://www.gamry.com/assets/Application-Notes/Basics-of-EIS.pdf.

27. Reece, C. *An Introduction to Electrochemical Impedance Spectroscopy*. [cited 2013 May]; Available from: https://www.jlab.org/conferences/tfsrf/Thursday/Th2_1-EIS%20intro%20Reece.pdf.

28. Park, S.-M. and J.-S. Yoo, *Peer Reviewed: Electrochemical Impedance Spectroscopy for Better Electrochemical Measurements.* Analytical Chemistry, 2003. **75**(21): p. 455 A-461 A.

29. Lasia, A., *Electrochemical Impedance Spectroscopy and its Applications*, in *Modern Aspects of Electrochemistry*, B.E. Conway, J.O.M. Bockris, and R. White, Editors. 2002, Springer US. p. 143-248.

30. Thermoline. *Refrigerated Circulating Baths*. 2012 September 2012 [cited 2013 June]; Available from: http://www.thermoline.com.au/catalogues/2012/refrigerated_circulated_baths.pdf.

31. Omega. *Omega Hand held digital thermometers*. HH800 series [cited 2013; Available from: http://www.omega.com/pptst/HH800.html.

32. Physics.org. *How does 3D printing work*. [cited 2013; Available from: http://www.physics.org/article-questions.asp?id=120.

33. Stratasys. *How PolyJet 3D Printing Works*. 2013 [cited 2013; Available from: http://www.stratasys.com/3d-printers/technology/polyjet-technology.

34. Bergin, S.D., et al., *New Solvents for Nanotubes: Approaching the Dispersibility of Surfactants.* The Journal of Physical Chemistry C, 2009. **114**(1): p. 231-237.

35. Giordani, S., et al., *Debundling of Single-Walled Nanotubes by Dilution: Observation of Large Populations of Individual Nanotubes in Amide Solvent Dispersions.* The Journal of Physical Chemistry B, 2006. **110**(32): p. 15708-15718.

CHAPTER 3

Electrolyte Investigation for Thermocells

3.1 Introductory remarks

When current is drawn from an electrochemical cell, the effects on potential difference may be plotted as shown in Figure 3.1. Said curves describe the current delivery capabilities of fuel cells [1], storage batteries, photoelectrochemical cells [2], and thermogalvanic cells [3, 4]. Typical thermocell behaviour would be that represented by the curve ABCD. The effect of activation overpotential accounts for the initial decline in potential difference from the equilibrium potential (point A) to point B. The linear portion (point B to point C) is representative of the ohmic overpotential. At high currents, mass transport overpotential effects (drawing current produces net electrode reactions that induce an accumulation of reaction products and depletion of reactants) cause the sharp decrease from point C to point D. For ideal thermocells, (dashed line in Figure 3.1) activation overpotential or ohmic overpotential would be negligible so as not to decrease the potential difference delivered by the cell from its equilibrium value. Furthermore, the mass transport overpotential effects are represented by a vertical drop from point E to point D; i.e. mass transport overpotential limits the amount of current that can be drawn from the thermocell.

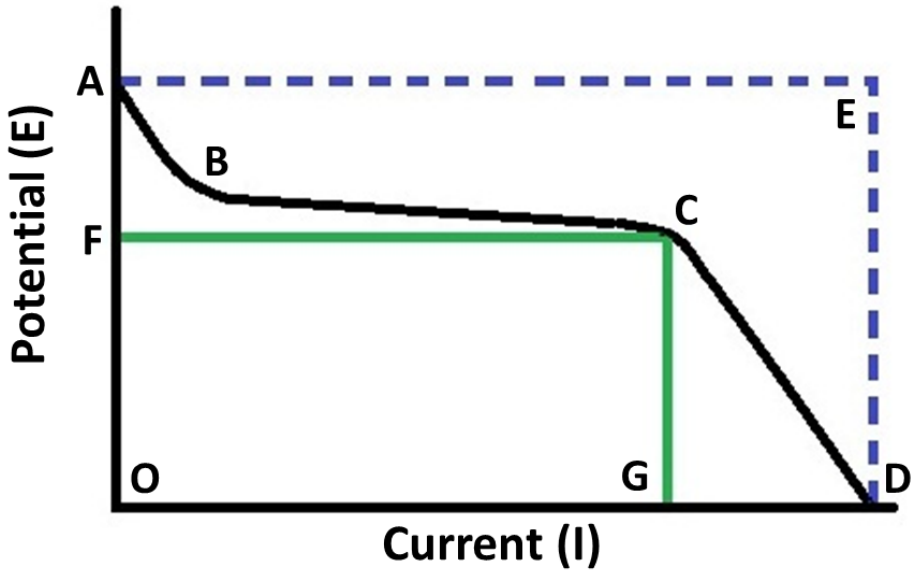

Figure 3.1 Potential-current (E-I) curves for thermogalvanic cells. Line ABCD depicts typical, while line AED represents ideal thermocell behaviour.

Consider the behaviour of a typical thermocell, the power delivered is maximum (P_{max}) at point C. Thermocell power conversion efficiency is at its highest when the area of the rectangle FCGO (subtended by the E-I curve of a typical thermocell in Figure 3.1) is maximised [5]. This happens when the potential and amount of current delivered at P_{max} is large. The requirements to ensure maximum thermocell power conversion efficiency are: 1) an electrolyte that has a high Seebeck coefficient. This will yield a large potential difference for a given temperature gradient; i.e. line OF is larger for electrolytes with a high Seebeck coefficient for a given activation overpotential [3, 6]. 2) The three overpotentials (activation, ohmic and mass transport) need to be kept to a minimum in order to ensure that the current delivery capability of the thermocell is maximised; i.e. line FC will be as long as possible [5]. 3) The ratio of the flux of charge carriers between the anode and cathode (electrical conductivity, σ) to the flux of heat flowing from the hot to cold

electrode (thermal conductivity, *K*) should be as large as possible. Solvents with high ionic conductivity but low thermal conductivity are ideal [7].

A list of the Seebeck coefficient of various redox couples is presented in (Table 3.1). The highest values reported are those for the neptunium and plutonium couples. However, the hazards of handling said couples have prevented their use in thermocell applications.

Table 3.1 Seebeck coefficient of various redox couples

Electrode Reaction	Seebeck Coefficient (mV/K)	Reference
$Ra \leftrightarrow Ra^{2+} + e^-$	0.28	[8]
$H(g) \leftrightarrow H^+ + e^-$	1.382	[8]
$Fe \leftrightarrow Fe^{2+} + 2e^-$	0.932	[8]
$Cu + I^- \leftrightarrow CuI + e^-$	0.671	[8]
$Ag + Br^- \leftrightarrow AgBr + e^-$	0.363	[8]
$Ag + Cl \leftrightarrow AgCl + e^-$	0.213	[8]
$Cu \leftrightarrow Cu^{2+} + 2e^-$	0.879	[8]
$U^{3+} \leftrightarrow U^{4+} + e^-$	1.02	[8]
$Fe^{2+} \leftrightarrow Fe^{3+} + e^-$	0.771	[8]
$Pb^{2+} + 2H_2O \leftrightarrow PbO_2 + 4H^+ + 2e^-$	0.633	[8]
$Zn + 4CN^- \leftrightarrow Zn(CN)_4^{2-} + 2e^-$	1.19	[8]
$Fe(CN)_6^{3-} \leftrightarrow Fe(CN)_6^{4-} + e^-$	1.4	[9]
$Np^{3+} \leftrightarrow Np^{4+} + e^-$	2-2.25	[10]
$Pu^{4+} \leftrightarrow Pu^{3+} + e^-$	2-2.25	[10]

Of note is the $Fe(CN)_6^{3-}/Fe(CN)_6^{4-}$ redox couple, which reversibly exchanges one electron per iron atom and produces a large reaction entropy. This system has one of the highest reported Seebeck coefficients for aqueous systems and a large exchange current [11]. It is for these reasons that $Fe(CN)_6^{3-}/Fe(CN)_6^{4-}$ has been extensively studied in thermocell applications [12-16].

3.2 Chapter aims

In this chapter, electrolyte ($K_3Fe(CN)_6/K_4Fe(CN)_6$) concentration is varied in order to investigate the effect this would have on thermo-power conversion capability. Particularly, the ionic and thermal conductivity of the various electrolyte concentrations is ascertained. The performance of chemically reduced graphene oxide (CRGO) as thermocell electrodes is also determined. The results are then compared to that of platinum in order to ascertain whether CRGO would be a viable electrode material for thermogalvanic cells.

3.3 Experimental setup

3.3.1 Chemically reduced graphene oxide synthesis

A schematic of the CRGO synthesis procedure is depicted in Figure 3.2.

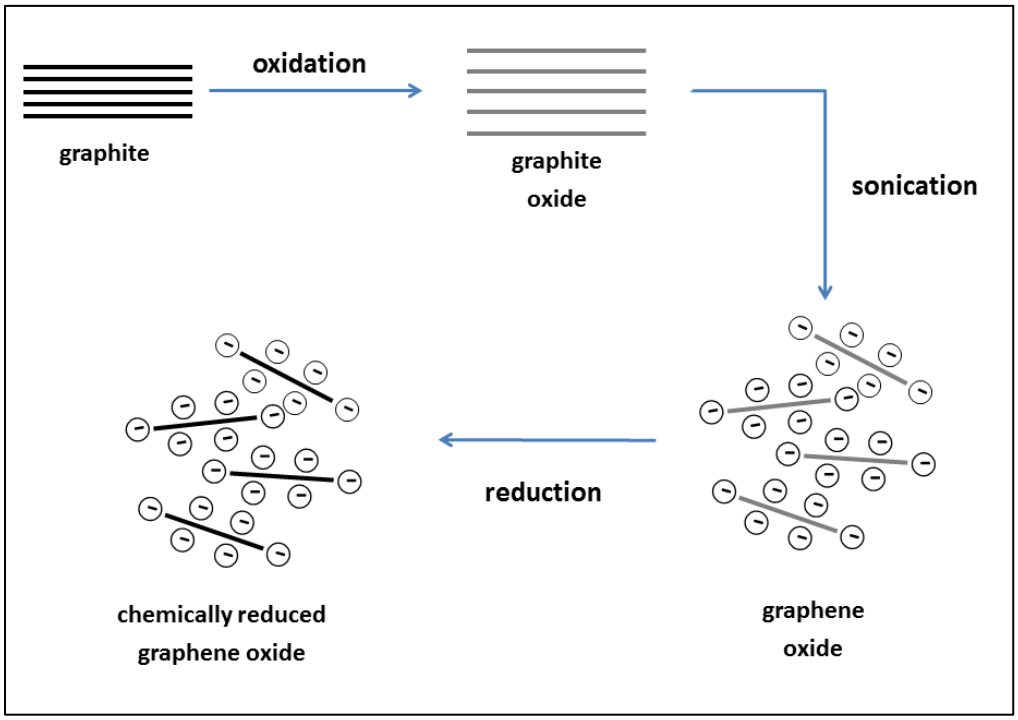

Figure 3.2 A schematic of the chemically reduced graphene oxide synthesis procedure

Graphite oxide (GO) was synthesised using a modified Hummers method wherein natural graphite was subjected to two oxidation steps. This was done to ensure complete oxidation, i.e. avoid particles that had a graphite oxide shell and graphite core. The initial oxidation step was as follows: 15 ml concentrated H_2SO_4, 5 g $K_2S_2O_8$ and 5 g P_2O_5 were mixed in a three-necked round bottom flask that was immersed in an oil bath at room temperature. The reaction temperature was then increased to 80 ^oC after which 10 g of Bay Carbon natural graphite powder was introduced to the mixture. The reaction was kept at 80 ^oC for 20 minutes then allowed to cool to room temperature. The mixture was then washed with de-ionised water and filtered until the filtrate was pH neutral; the resulting filtrand being pre-oxidized graphite.

The second oxidation step was carried out by cooling 230 ml of H_2SO_4, in a round bottomed flask using an ice and water bath, to 0 ^oC. The pre-oxidized graphite was then added followed by 30 g $KMnO_4$, these reactants were added slowly to ensure the temperature did not rise above 20 ^oC. The reaction temperature was then raised to 35 ^oC and maintained for 2 hours. 460 ml of de-ionised water was then added very slowly to prevent an excessive rise in temperature. The reaction was then allowed to cool to room temperature. 1400 ml of de-ionised water was added followed by 25 ml of 30 % H_2O_2; this induced a colour change in the mixture, making it bright yellow (Figure 3.3). The H_2O_2 is added after hydrolysis to decompose the permanganate ions into manganese (IV) ions. The reaction was stirred for 15 minutes to allow complete oxidation to occur.

Figure 3.3 Typical reaction vessel used in the synthesis of chemically reduced graphene oxide. Addition of H_2O_2 induces a colour change, making the slurry turn bright yellow as shown.

The mixture was then centrifuged (Sigma 4-15) at 3500 rpm for 30 minutes. The sediments were collected and mixed with 3650 ml of 1:10 concentrated HCl:de-ionised water solution for 15 minutes then centrifuged at 3500 rpm for 30 minutes. Washing with HCl ensures that no manganese hydroxides form, which may get trapped between the graphene layers. Repeated "washing" of the sediments was done as follows: the sediments were collected and mixed with de-ionised water followed by centrifuging at 3500 rpm. This "washing" procedure was repeated until the pH of the supernatant reached a value of 4; yielding sediment that is GO.

GO was dispersed in de-ionised water to obtain a 200 ml solution at 0.5 wt %. Said solution was subjected to probe sonication (Branson Probe Sonifier)

for 2 hours using an 8 second on/off pulse setting thus exfoliating the GO, resulting in graphene oxide. The 200 ml solution was then diluted to 2 L, resulting in a 0.05 wt % graphene oxide dispersion, which was also subjected to probe sonication for 2 hours using the same pulse settings (8 seconds on/off).

Chemical reduction of the 2 L graphene oxide dispersion was done as follows: 400 μL of hydrazine, 6 ml of ammonia and 50 ml of H_2O were mixed then added to the 2 L graphene oxide dispersion. The temperature was then raised to 90 ^oC and left for 40 minutes with constant stirring to allow the reduction to reach completion. The resulting chemically reduced graphene oxide dispersion was then allowed to cool to room temperature.

3.3.2 Thermocell testing

CRGO films were prepared by vacuum filtration onto a polyvinylidene fluoride membrane (0.1 μm pore size). These films were then re-sized and used as electrodes that were 1.5 cm x 0.5 cm and approximately 1.8 μm thick (Figure 3.4). Silver paste was used to attach the CRGO film to a platinum wire.

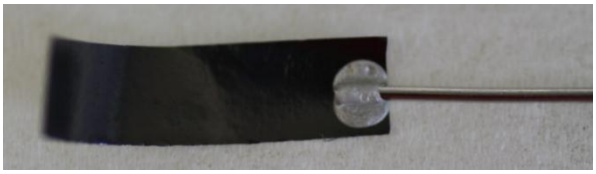

Figure 3.4 CRGO electrode used in thermal harvesting experiments. Silver paste ensures good electrical contact between the film and platinum wire.

Thermal harvesting experiments were carried out using an in-house designed H-shaped cell (Figure 3.5) with a separation distance of 10 cm wherein one half-cell

was cooled using circulating liquid and the other was heated using an Omegalux rope heater (accuracy ± 1 ^{o}C) connected to a TCA Control Box that has 48 x 48 Controller with PID control action and 25 amp Solid State relay.

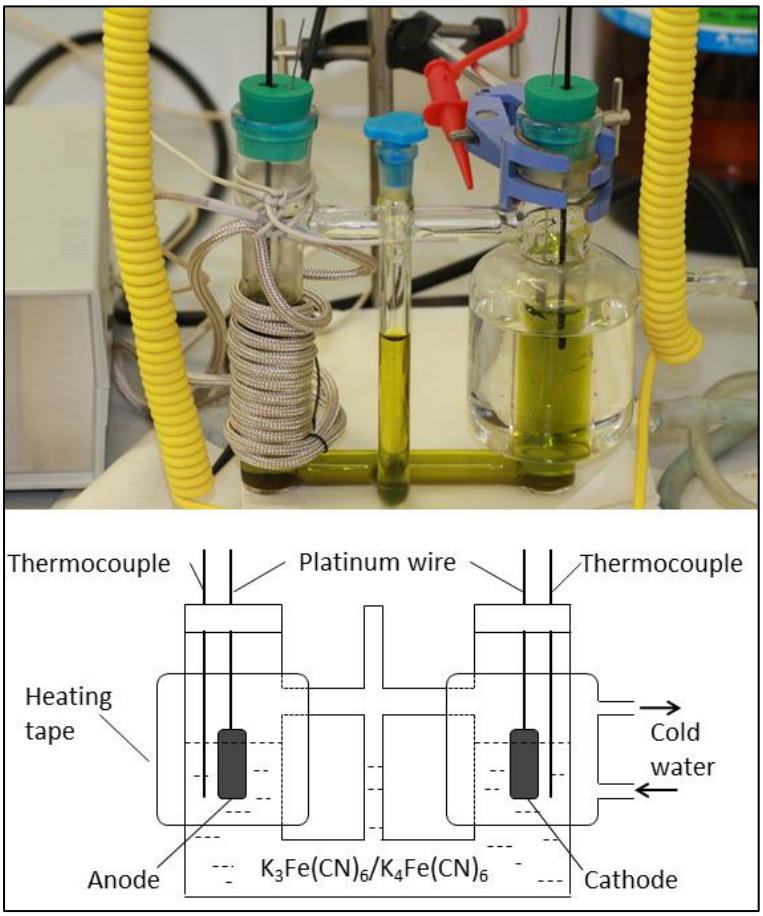

Figure 3.5 Photo and schematic of the H-Cell used in thermal harvesting experiments

The temperature difference between the two sides was varied from 10 ^{o}C to 60 ^{o}C at 10 ^{o}C intervals. Teflon PFA coated thermocouple probes were positioned beside the electrodes to monitor the temperature in both sides of the cell. The electrolyte used was $K_3Fe(CN)_6/K_4Fe(CN)_6$ in aqueous media with concentrations of 0.1, 0.2, 0.3 and 0.4 mol/L. The maximum electrolyte concentration was set to 0.4 mol/L as this is the saturation point of $K_3Fe(CN)_6/K_4Fe(CN)_6$ in water.

3.3.3 Characterisation

Ultraviolet-Visible Spectroscopy (UV-Vis) was performed on the graphene oxide and CRGO dispersions using a Shimadzu UV-3600 spectrophotometer. The graphene oxide and CRGO films were subjected to thermogravimetric analysis in air using a TA Instruments Q500 TGA. The samples were heated from room temperature to 900 ^{o}C at a rate of 2 ^{o}C/minute. A JANDEL RM3 four point probe was used to obtain sheet resistance measurements. Film morphology was investigated through the use of a JEOL JSM-7500FA Field Emission Scanning Electron Microscope

The ionic conductivity and viscosity of the various $K_3Fe(CN)_6/K_4Fe(CN)_6$ solutions was measured using a TPS smartCHEM-Lab and AR-G2 Rheometer respectively. Thermal conductivity measurements were carried out using a C-Therm TCi Thermal Conductivity Analyzer (C-Therm Technologies Ltd., Canada) [17].

3.4 Results and discussion

3.4.1 Chemically reduced graphene oxide synthesis

The sheet resistance of graphene oxide films having a thickness of 1.8 μm could not be measured owing to its very high value; i.e. the films were very resistive. During the oxidation step, hydroxyl, epoxy, ether, diol, and ketone groups are introduced on the basal planes and edges of the graphene oxide [18]. While said functional groups allow the formation of stable graphene oxide dispersions in water,

they disrupt the π-conjugation. This disruption renders the graphene oxide electrically insulating and accounts for the high resistance[19].

The produced CRGO films had a thickness of 1.8 μm and a sheet resistance of 219.11 Ω/Square. The reduction of graphene oxide through the use of hydrazine facilitated the removal of the functional groups that were disrupting the π-conjugation within the CRGO sheets [20]. The restoration of sp^2 structure facilitates recovery of electrical conjugation and renders the CRGO film conductive [21].

TGA curves (Figure 3.6) of graphene oxide (sample mass: 0.395 mg) indicate a weight loss of 30.11 % around a temperature of 200 ^oC which may be attributed to the pyrolysis of oxygen containing functional groups forming CO, CO_2 and steam. Chemical reduction of graphene oxide with hydrazine removed the oxygen containing functional groups, which is evident in the lack of weight loss at 200 ^oC for the TGA curves of CRGO (sample mass: 0.465 mg) [20, 22]. CRGO also displays an abrupt mass loss at 548.8 ^oC wherein 83.83 % of the sample decomposes. Graphene oxide, on the other hand starts decomposing at 410.8 ^oC, a temperature that is almost 40 ^oC lower than CRGO. This disparity may be ascribed to the difference in structure for these two carbon materials. The oxygen containing functional groups in graphene oxide diminish the integrity of the sp^2 system which lowers its thermal stability and also leads to total decomposition. Hydrazine reduction in CRGO restores the sp^2 system which leads to its higher thermal stability [23].

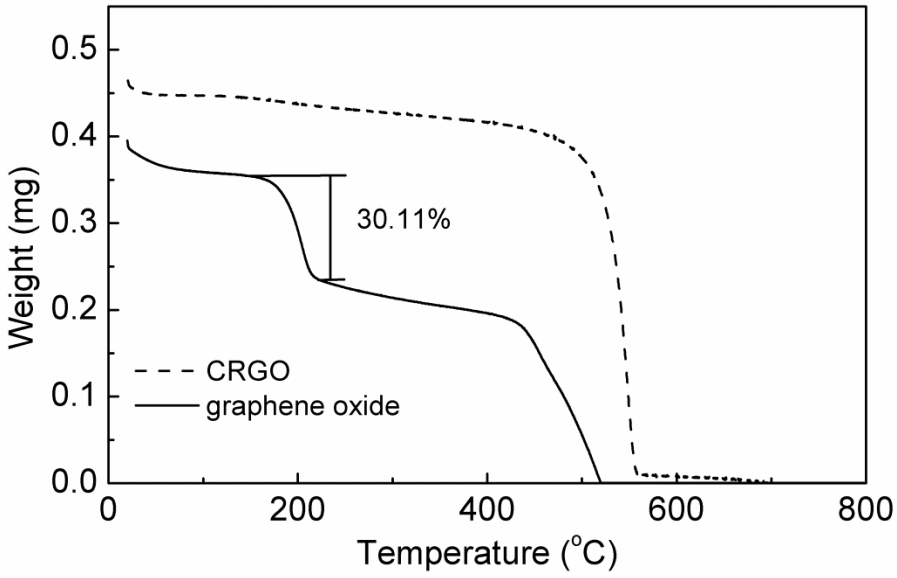

Figure 3.6 Themogravimetric analysis of CRGO and graphene oxide films heated at a rate of 2 ^{o}C/minute.

The position of the largest peak (λ_{max}) in the UV-Vis spectra of the graphene oxide and CRGO dispersions provides insight to the degree of electronic conjugation. A higher λ_{max} results when there are more $\pi \rightarrow \pi^*$ transitions (electronic conjugation) because less energy needs to be used for the electronic transition [24]. The redshift in the absorption peak in the UV-Vis (Figure 3.7) of CRGO (267 nm) as compared to graphene oxide (232 nm) indicates a restoration of electronic conjugation; i.e. removal of oxygen containing functional groups due to the chemical reduction with hydrazine. A shoulder around 300 nm is present in the graphene oxide sample which may be attributed to the $n \rightarrow \pi^*$ transitions of the carbonyl groups [24]. Said shoulder is not present in the CRGO sample, another indicator of the successful reduction process. The increased absorbance of the CRGO sample as compared to the graphene oxide sample indicates that the former has a more regular carbon framework; i.e. more aromatic rings [24].

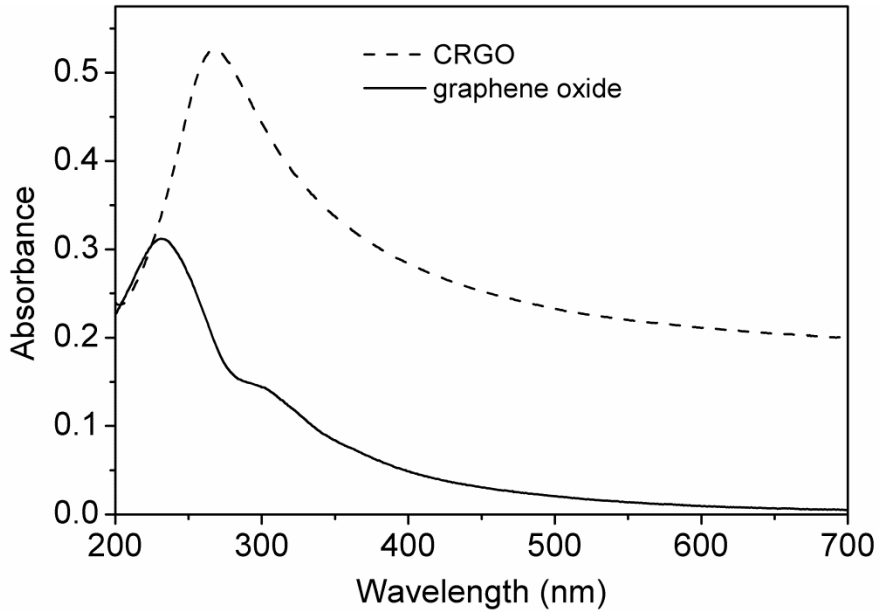

Figure 3.7 UV-Vis spectra of CRGO and graphene oxide dispersions reveal a redshift in the absorption peak of the former; which is indicative of a restoration of electronic conjugation.

3.4.2 Optimisation of $K_3Fe(CN)_6/K_4Fe(CN)_6$ concentration

Thermocell testing (Figure 3.8) shows that the mass current density (I_{mass}) increases as the $K_3Fe(CN)_6/K_4Fe(CN)_6$ concentration is raised. The maximum I_{mass} of 1207.37 A/kg was obtained using 0.4 M solution (the saturation point of $K_3Fe(CN)_6/K_4Fe(CN)_6$ in water). The augmentation of I_{mass} with electrolyte concentration is brought about by two reasons: first, higher $K_3Fe(CN)_6/K_4Fe(CN)_6$ decreases the ohmic overpotential of the thermocell, this is the dominant contributor to cell resistance and will be discussed in detail later [25]. Second, an increase in electrolyte concentration increases the availability of species to carry out the redox reactions as required to generate the short circuit current.

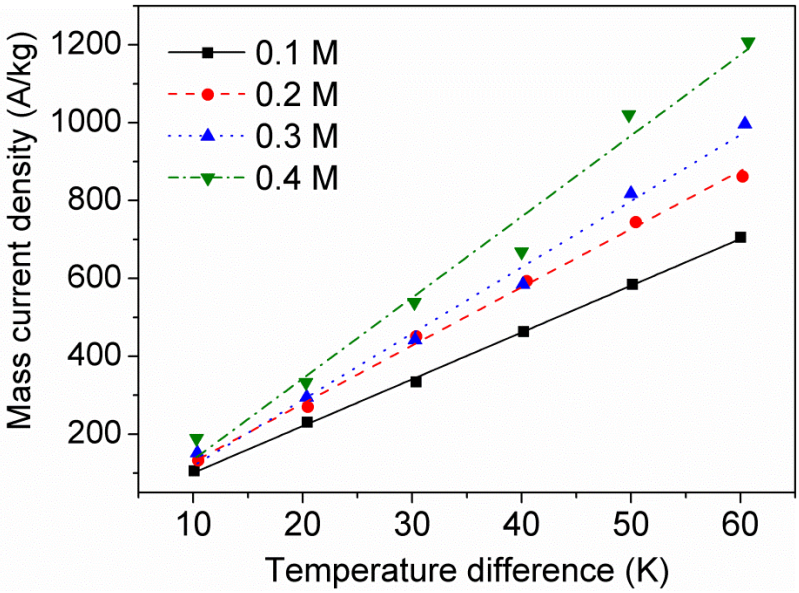

Figure 3.8 Dependence of I_{mass} (using CRGO electrodes) on increasing thermal gradients. I_{mass} also scales with $K_3Fe(CN)_6/K_4Fe(CN)_6$ concentration.

Plots of open circuit voltage (V_{oc}) at different electrolyte concentration (Figure 3.9) do not show much variation. The average V_{oc} at a temperature difference of 60 K is 83.88 mV, giving a Seebeck coefficient of 1.39 mV/K; a value that is in good agreement with literature [12].

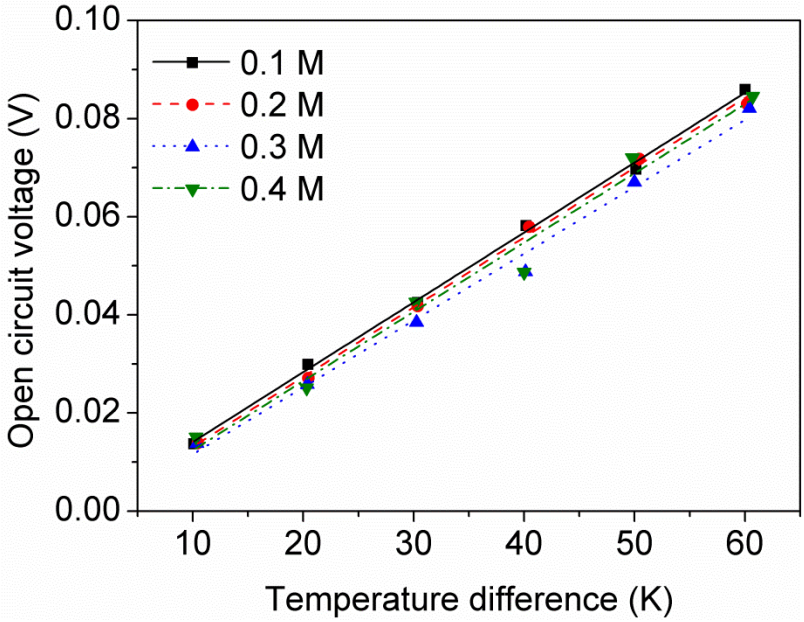

Figure 3.9 Dependence of V_{oc} (using CRGO electrodes) on increasing thermal gradients. Variation in $K_3Fe(CN)_6/K_4Fe(CN)_6$ concentration produces no change in V_{oc}.

The measured values of the Seebeck coefficient against electrolyte concentration is expected since the amounts of redox mediator used was equimolar and the Seebeck coefficient is dictated by the thermodynamics of the redox couple as given by Equation 3.1 [5]:

$$S = \frac{\Delta V}{\Delta T} = \frac{S_B - S_A}{nF} \qquad \text{Equation 3.1}$$

Where S is the Seebeck coefficient of a hypothetical redox couple A ↔ ne- + B, ΔV represents the electrode potential, ΔT is temperature difference between electrodes, S_A and S_B are the partial molar entropies of species A and B respectively, n is the number of electrons involved in the redox reaction and F is Faraday's constant.

As mentioned in Chapter 1, the power conversion efficiency of thermogalvanic systems can be expressed as [5]:

$$\Phi = \frac{0.25\, V_{oc} I_{sc}}{KA\left(\frac{\Delta T}{d}\right)} \qquad \text{Equation 3.2}$$

Using Equation 3.2, power conversion efficiency at the various electrolyte concentrations were calculated and are presented in Figure 3.10. Said figure shows that the power conversion efficiency (measured at ΔT = 60 K) scales with concentration of the redox mediator. The highest value obtained for the thermocell used in this study was 0.00825% at an electrolyte concentration of 0.4 M.

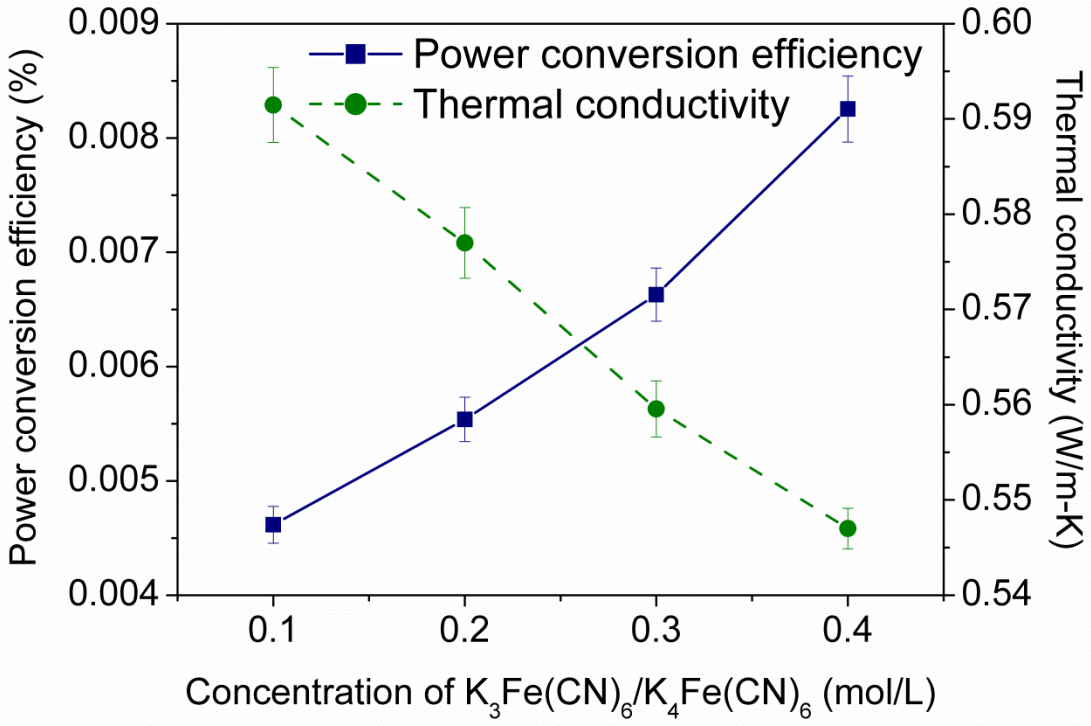

Figure 3.10 Power conversion efficiency measured at a thermal gradient of 60 K, and thermal conductivity measured at room temperature, of increasing concentrations of $K_3Fe(CN)_6/K_4Fe(CN)_6$ solutions.

Figure 3.10 depicts that the thermal conductivity of the electrolyte decreases as the concentration of the redox mediator is increased. This is one explanation as to why power conversion efficiency scales with electrolyte concentration. Despite the fact that an increase in temperature induces a rise in thermal conductivity of the $K_3Fe(CN)_6/K_4Fe(CN)_6$ solutions at roughly the same rate (Figure 3.11); the 0.4 M solution still has the most desirable thermal conductivity for thermocell electrolyte applications. The thermal conductivity for the 0.4 M solution ranges from 0.547 W/m-K (at room temperature) up to 0.586 W/m-K (at 80^{o}C), values that are lower than the minimum thermal conductivity of the 0.1 M solution which ranges from 0.591 W/m-K (at room temperature) to 0.643 W/m-K (at 80^{o}C). The lower thermal conductivity of the 0.4 M $K_3Fe(CN)_6/K_4Fe(CN)_6$ solution inhibits the thermal flux from the hot to the cold electrode and maximizes the power conversion efficiency by allowing a larger thermal gradient to be maintained between the two electrodes.

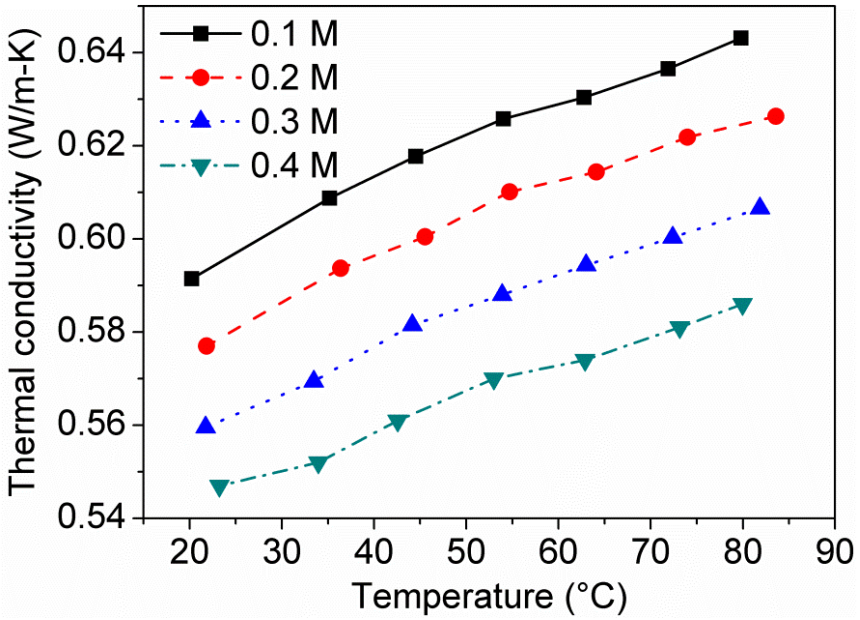

Figure 3.11 Thermal conductivity of various concentrations of $K_3Fe(CN)_6/K_4Fe(CN)_6$ solutions at increasing temperature.

Viscosity measurements were performed on the various concentrations of $K_3Fe(CN)_6/K_4Fe(CN)_6$ to further understand their effects on thermocell device performance. In order to establish the shear rate, the viscosity of a 0.4 M solution of $K_3Fe(CN)_6/K_4Fe(CN)_6$ at room temperature was monitored while the shear rate was varied from 1 to 100 s^{-1}. The results of this initial experiment (inset of Figure 3.12) reveal that changes in viscosity are negligible after a shear rate of 70 s^{-1}.

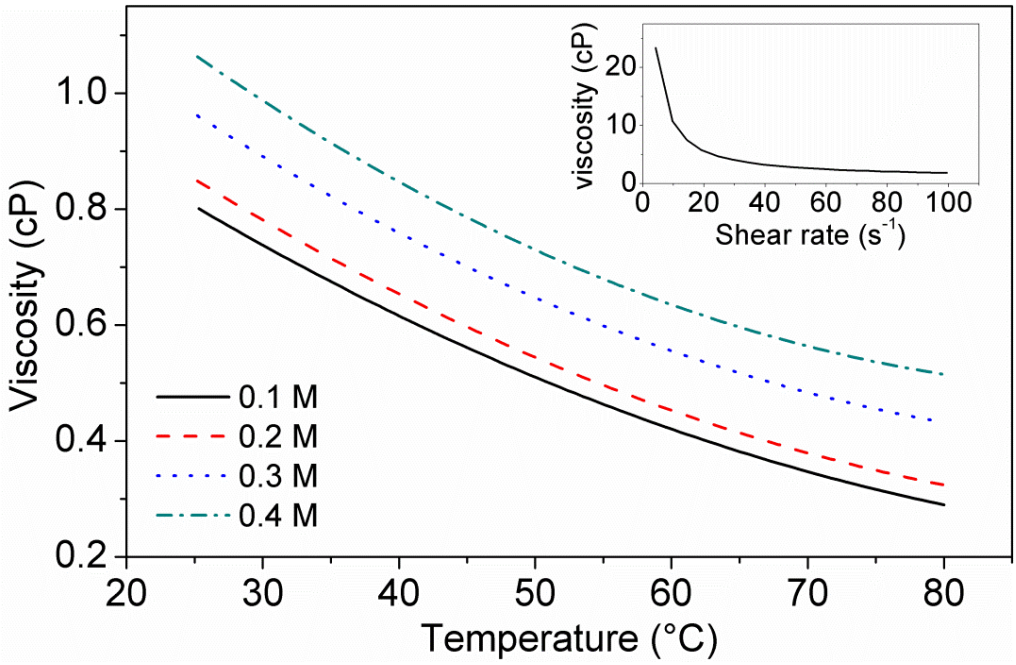

Figure 3.12 Viscosity of various concentrations of $K_3Fe(CN)_6/K_4Fe(CN)_6$ solutions at increasing temperature; Inset: viscosity at various shear rates for 0.4 M $K_3Fe(CN)_6/K_4Fe(CN)_6$

Using the established shear rate of 100 s^{-1}, the temperature of the various $K_3Fe(CN)_6/K_4Fe(CN)_6$ solutions was ramped from 25 ^oC to 80 ^oC while the viscosity was measured. Results (Figure 3.12) indicate that the viscosity is directly proportional to the redox mediator concentration; i.e. higher concentrations have higher viscosity values. Owing to the fact that convection dominates heat transfer in liquids, a solution with increased viscosity would have diminished convective currents flowing. This decreased rate of heat transfer across the electrolyte is desirable in thermogalvanic cells as it would result in an increase in power conversion efficiency.

For all the concentrations of the $K_3Fe(CN)_6/K_4Fe(CN)_6$ solutions, viscosity decreases as the solution temperature is increased. A molecule must attain a minimum amount of energy for it to escape from its neighbours and move in a

liquid. At elevated temperatures, the speed of molecules in a liquid is increased hence a decrease in the time molecules spend in contact with their nearest neighbours occurs. In other words, the increased molecular kinetic energy at higher temperatures offsets the intermolecular forces of attraction and this allows the liquid to flow more freely. These results are also in agreement with Equation 3.3, which depicts the temperature dependence of the coefficient of viscosity, a parameter that is inversely proportional to the mobility of molecules in a liquid [26].

$$\eta \propto e^{\frac{Ea}{RT}} \qquad \text{Equation 3.3}$$

Where η is the coefficient of viscosity, *Ea* is the activation energy, *R* is the universal gas constant and *T* is temperature. The inverse relationship between viscosity and temperature implies that mass transfer via diffusion and convection will occur more readily at elevated temperatures.

As mentioned previously, to ensure maximum power conversion efficiency the mass transfer overpotential must be kept to a minimum. In a physical sense, this means that reaction products formed at the cold electrode must travel (via diffusion and convection) to the hot side and vice versa. The unavailability of reactants at the electrodes (ferricyanide at the cold cathode, ferrocyanide at the hot anode) will result in decreased values of I_{mass}. Thus higher operating temperatures are better for thermocells due to the increase in mass transfer; i.e. mass transfer occurs fast enough in the thermocell to sustain the redox reactions taking place.

Despite increased viscosity at higher electrolyte concentrations, which impedes mass transport by convection, the mass power density produced by the

thermocell increases. This is brought about by scaling of the solution conductivity with concentration (63.4 mS/cm at 0.1 M as compared to 292 mS/cm at 0.4 M) as shown in Figure 3.13. The fact that mass power density is increased at higher electrolyte concentrations (Figure 3.13) indicates that ohmic resistance in the cell has a greater effect on the overall cell performance than mass transfer.

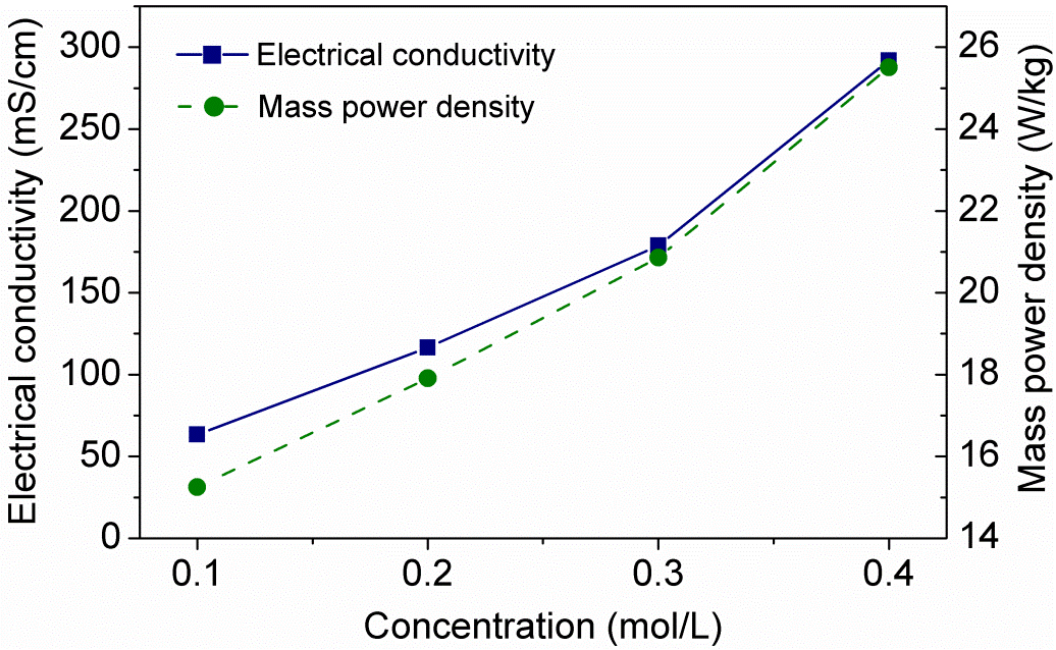

Figure 3.13 Electrical conductivity and mass power density measured at increasing concentrations of $K_3Fe(CN)_6/K_4Fe(CN)_6$ solutions.

3.4.3 Comparison of chemically reduced graphene oxide with platinum as thermocell electrodes

Thermocell tests (Figure 3.14) were run using CRGO and platinum electrodes in a 0.4 M $K_3Fe(CN)_6/K_4Fe(CN)_6$ solution in order to compare the performance of the two materials. The maximum mass power density obtained using CRGO electrodes was 25.51 W/kg at a temperature difference of 60 K. For platinum

electrodes the maximum power density (ΔT = 60 K) obtained was only 0.067 W/kg, a value lower by three orders of magnitude.

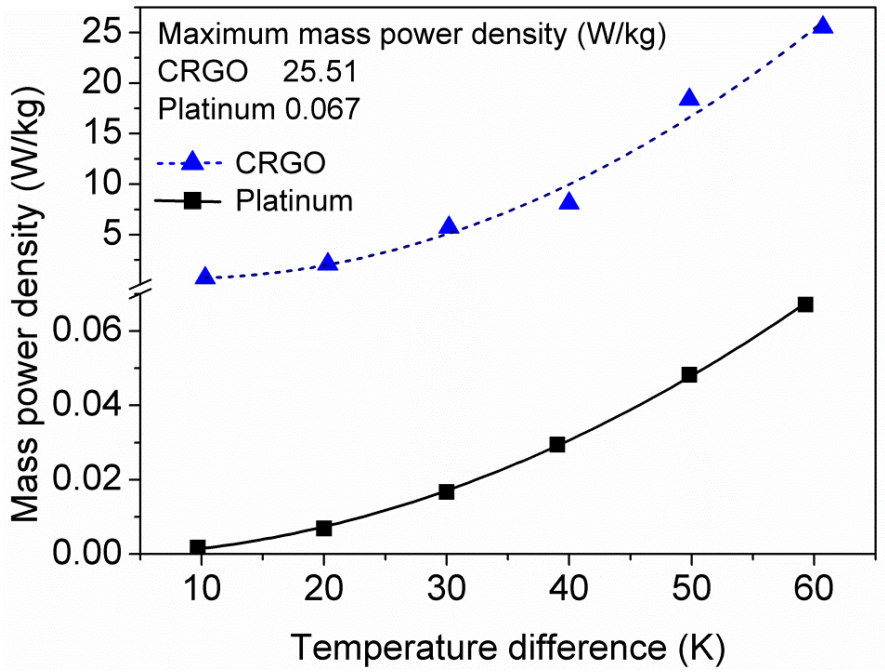

Figure 3.14 Mass power density at increasing thermal gradients obtained using CRGO and platinum electrodes. Electrolyte used: 0.4 M $K_3Fe(CN)_6/K_4Fe(CN)_6$.

An SEM image of the CRGO electrode surface (Figure 3.15A) reveals a relatively flat surface with a sheet-like structure apparent. Although CRGO sheets restack upon vacuum filtration [27], the cross-section of the film (Figure 3.15B) reveals a morphology that is more porous than that of a flat platinum sheet. This increased porosity (compared to platinum) allows greater interaction between the electrode and electrolyte; i.e. more sites are available for the redox reactions to occur. It is surmised that this increased accessible surface area accounts for the higher mass power density of the CRGO as compared to platinum.

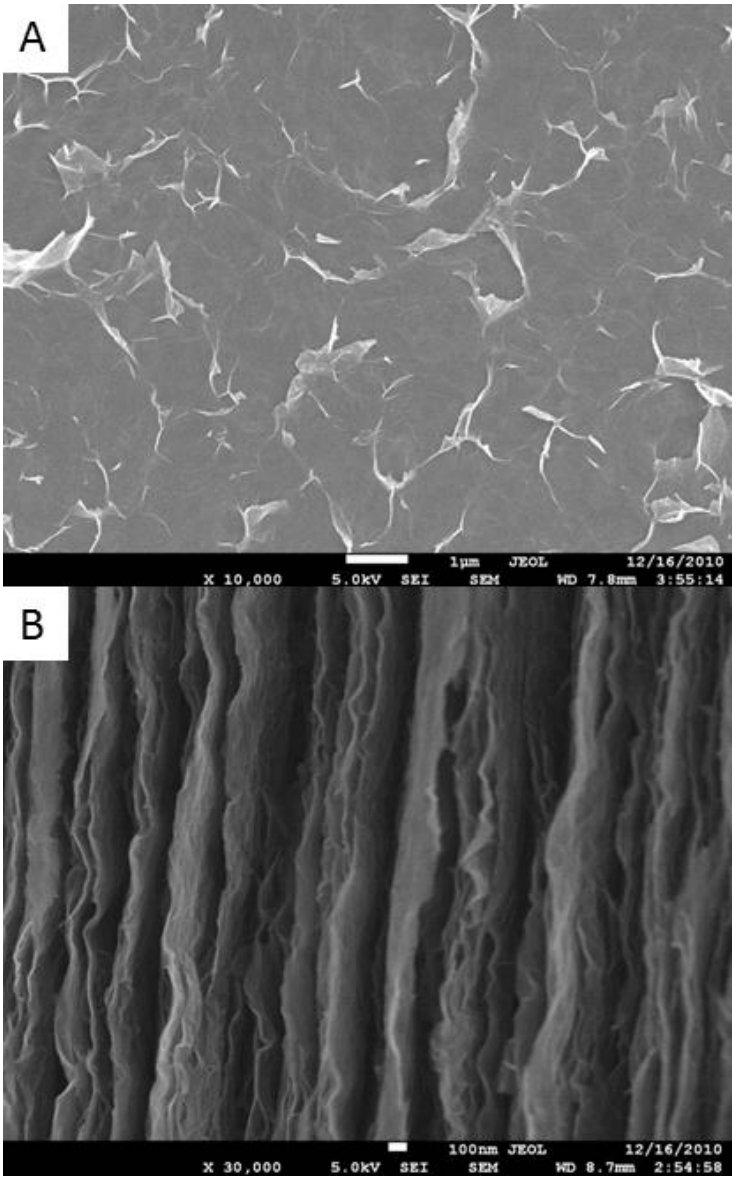

Figure 3.15 SEM images of A) surface and B) cross-section of the CRGO electrode.

Comparison of the mass current density generated by the CRGO and platinum electrodes (Figure 3.16) provides further evidence of the porous nature of the former. The maximum mass current density (attained at ΔT = 60 K) is 1207.37 A/kg for CRGO and only 3.12 A/kg for platinum. Again, the higher I_{mass} may be attributed to the larger electroactive surface area of CRGO. Comparison of V_{oc} at different temperatures of both materials (Figure 3.17) indicates very similar profiles. The

measured Seebeck coefficient of CRGO is 1.41 mV/K and 1.47 mV/K for platinum. This similarity is expected as V_{oc} is mainly dictated by the thermodynamics of the redox couple [5]. The fact that V_{oc} is the same for both materials implies that the higher values of power density is brought about by the greater I_{mass} attained through the use of CRGO electrodes.

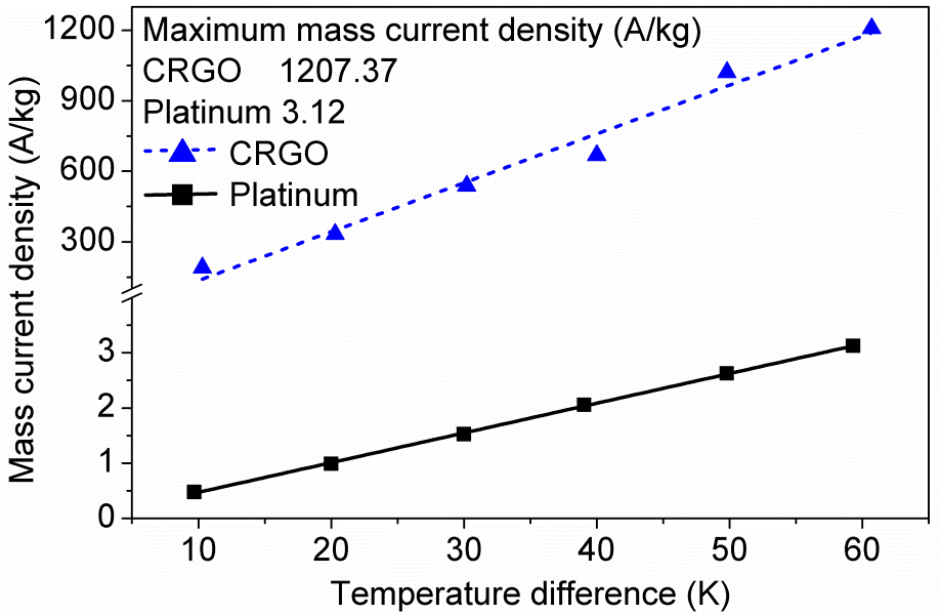

Figure 3.16 Mass current density at increasing thermal gradients obtained using CRGO and platinum electrodes. Electrolyte used: 0.4 M $K_3Fe(CN)_6/K_4Fe(CN)_6$.

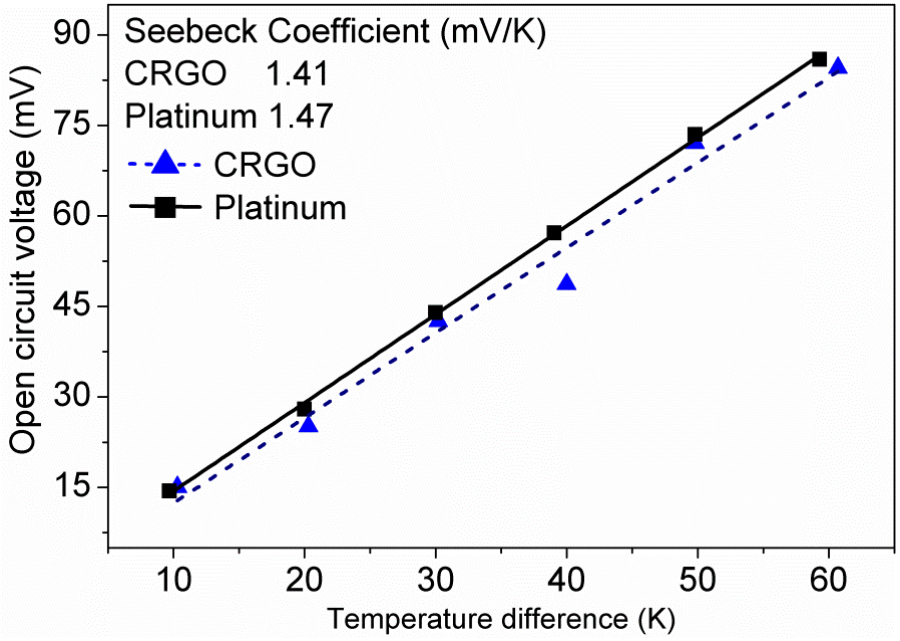

Figure 3.17 Open circuit voltage at increasing thermal gradients obtained using CRGO and platinum electrodes. Electrolyte used: 0.4 M $K_3Fe(CN)_6/K_4Fe(CN)_6$.

As mentioned in Chapter 1, standardisation of thermocell power conversion efficiency measurements may be done by comparing values obtained to those obtained if a Carnot engine was used at the same operating conditions (temperature) using the following equation [5]:

$$\Phi_r = \frac{\Phi_{thermogalvanic\ cell\ operating\ at\ \Delta T}}{\Phi_{Carnot\ engine\ operating\ at\ \Delta T}} \qquad \text{Equation 3.4}$$

Using CRGO electrodes and an electrolyte concentration of 0.4 M $K_3Fe(CN)_6/K_4Fe(CN)_6$ the efficiency relative to a Carnot engine is 0.012 %. The efficiency needs to be at around 2 to 5 % of the Carnot maximum for commercial viability [5]. However, the thickness of the film (1.8μm) must be taken into account. Thermocell efficiency calculations are based on the geometric area and

not the mass of the electrode (Equation 3.2). Increasing the CRGO film thickness may result in a larger electroactive surface area (due to its porous nature) while maintaining the geometric area. It is surmised that this may result in larger values of I_{mass}, power density and power conversion efficiency.

3.5 Conclusion

Increasing the concentration of the $K_3Fe(CN)_6/K_4Fe(CN)_6$ redox mediator results in a decrease in the thermal conductivity of the electrolyte which maximises the temperature gradient between the two electrodes. Despite the fact that viscosity scales with concentration, which hinders mass transport between the two electrodes, the decrease in the ohmic overpotential (as electrolyte concentration is increased) has a greater effect on the thermal cell performance which results in higher short circuit currents produced, thus leading to better mass power density. The combined effect of these factors results in improved power conversion efficiency of the thermal cell. CRGO is a feasible electrode material for thermogalvanic cells as it produces high mass power density due to its large electroactive surface area as compared to flat electrodes. Increasing the CRGO electrode thickness may augment the power delivery capability of thermocells by providing more sites where redox reactions may occur.

3.6 References

1. Bockris, J.O.M. and A.K.N. Reddy, *Modern electrochemistry: an introduction to an interdisciplinary area*. 1970: Plenum Press.

2. Quickenden, T.I. and G.K. Yim, *The power conversion efficiency of the gold-rhodamine B-bold photoelectrochemical cell.* Solar Energy, 1977. **19**(3): p. 283-289.

3. Quickenden, T.I. and C.F. Vernon, *Thermogalvanic conversion of heat to electricity.* Solar Energy, 1986. **36**(1): p. 63-72.

4. Shindo, K., M. Arakawa, and T. Hirai, *Effect of non-graphitized carbon electrodes on the electrochemical characteristics of a thermocell with a Br_2/Br^- redox couple.* Journal of Power Sources, 1998. **70**(2): p. 228-234.

5. Quickenden, T.I. and Y. Mua, *A Review of Power Generation in Aqueous Thermogalvanic Cells.* Journal of The Electrochemical Society, 1995. **142**(11): p. 3985-3994.

6. Bonetti, M., et al., *Huge Seebeck coefficients in nonaqueous electrolytes.* The Journal of Chemical Physics, 2011. **134**(11): p. 114513-8.

7. Artjom V, S., *Theoretical study of thermogalvanic cells in steady state.* Electrochimica Acta, 1994. **39**(4): p. 597-609.

8. deBethune, A.J., T.S. Licht, and N. Swendeman, *The Temperature Coefficients of Electrode Potentials: The Isothermal and Thermal Coefficients—The Standard Ionic Entropy of Electrochemical Transport of the Hydrogen Ion.* Journal of The Electrochemical Society, 1959. **106**(7): p. 616-625.

9. Kang, T.J., et al., *Electrical Power From Nanotube and Graphene Electrochemical Thermal Energy Harvesters.* 2011: p. - n/a.

10. Blanc, P. and C. Madic, *Thermoelectric properties of M^{4+}/M^{3+} and MO^{22+}/MO^{2+} redox couples of neptunium and plutonium in aqueous $HClO_4$ and HNO_3 media.* Inorganica Chimica Acta, 1984. **94**(1–3): p. 134-136.

11. Nugent, J.M., et al., *Fast Electron Transfer Kinetics on Multiwalled Carbon Nanotube Microbundle Electrodes.* Nano Letters, 2001. **1**(2): p. 87-91.

12. Hu, R., et al., *Harvesting Waste Thermal Energy Using a Carbon-Nanotube-Based Thermo-Electrochemical Cell.* Nano Letters, 2010. **10**(3): p. 838-846.

13. Salazar, P.F., S. Kumar, and B.A. Cola, *Nitrogen- and Boron-Doped Carbon Nanotube Electrodes in a Thermo-Electrochemical Cell.* Journal of The Electrochemical Society, 2012. **159**(5): p. B483-B488.

14. Hornut, J.M. and A. Storck, *Experimental and theoretical analysis of a thermogalvanic undivided flow cell with two aqueous electrolytes at different temperatures.* Journal of Applied Electrochemistry, 1991. **21**(12): p. 1103-1113.

15. Goncalves, R. and T. Ikeshoji, *Comparative studies of a thermoelectric converter by a thermogalvanic cell with a mixture of concentrated potassium ferrocyanide and potassium ferricyanide aqueous solutions at great temperature differences.* J. Braz. Chem. Soc, 1992. **3**(3): p. 4.

16. Burrows, B., *Discharge Behavior of Redox Thermogalvanic Cells.* Journal of The Electrochemical Society, 1976. **123**(2): p. 154-159.

17. *C-Therm Technologies Ltd.C-Therm Technologies-Products*. Available from: http://www.ctherm.com/products/tci_thermal_conductivity

18. Hontoria-Lucas, C., et al., *Study of oxygen-containing groups in a series of graphite oxides: physical and chemical characterization.* Carbon, 1995. **33**(11): p. 1585-1592.

19. Coleman, J.N., *Liquid-Phase Exfoliation of Nanotubes and Graphene.* Advanced Functional Materials, 2009. **19**(23): p. 3680-3695.

20. Stankovich, S., et al., *Synthesis of graphene-based nanosheets via chemical reduction of exfoliated graphite oxide.* Carbon, 2007. **45**(7): p. 1558-1565.

21. Park, S., et al., *Colloidal Suspensions of Highly Reduced Graphene Oxide in a Wide Variety of Organic Solvents.* Nano Letters, 2009. **9**(4): p. 1593-1597.

22. Lerf, A., et al., *Structure of Graphite Oxide Revisited.* The Journal of Physical Chemistry B, 1998. **102**(23): p. 4477-4482.

23. da Silva, M., et al., *Synthesis and characterization of CeO_2–graphene composite.* Journal of Thermal Analysis and Calorimetry, 2012. **107**(1): p. 257-263.

24. Marcano, D.C., et al., *Improved Synthesis of Graphene Oxide.* ACS Nano, 2010. **4**(8): p. 4806-4814.

25. Mua, Y. and T.I. Quickenden, *Power Conversion Efficiency, Electrode Separation, and Overpotential in the Ferricyanide/Ferrocyanide Thermogalvanic Cell.* Journal of The Electrochemical Society, 1996. **143**(8): p. 2558-2564.

26. Atkins, P. and J.d. Paula, *Physical Chemistry*. 7th ed. 2002, New York: Oxford University Press.

27. Chen, H., et al., *Mechanically Strong, Electrically Conductive, and Biocompatible Graphene Paper*. Advanced Materials, 2008. **20**(18): p. 3557-3561.

CHAPTER 4

Comparison of Various Cell Configurations for Thermal Harvesting

4.1 Introductory remarks

As mentioned in Chapter 1, ohmic and mass transport overpotentials need to be minimised in order to attain maximal thermocell power conversion efficiency. The negative effects of these two overpotentials can be mitigated through proper cell configuration. When electrodes are placed far apart, ohmic overpotential is dominated by the electrolyte resistance. This is especially true when nano-carbon electrodes are used as it has been shown that the resistivity of aqueous electrolytes are 2 to 3 orders of magnitude higher than said electrode material [1]. Furthermore, mass transport overpotential is maximised as ions will need to travel great distances between electrodes. By decreasing the inter-electrode separation, an increase in generated power will be observed as both ohmic and mass transport overpotentials will decrease [2]. However, a short distance between the anode and cathode translates to large thermal flux between electrodes. This thermal flux results in low power conversion efficiency as it will be harder to maintain a large thermal gradient in the cell [3]. A balance between power density and power conversion efficiency can be achieved with proper thermocell design.

The development of flexible electrodes for electrochemical applications has paved the way for innovative cell designs for thermal energy conversion. Contact

resistance in thermocells can be significantly reduced by growing CNT forests onto the cell housing. Scrolled electrodes to mitigate heat loss and flexible thermocells that can be wrapped around cooling/heating pipes have been achievable through flexible CNT electrodes [4].

4.1.1 Scrolled electrodes for thermocells

As mentioned in Chapter 1, thermocells using platinum electrodes without circulation of the electrolyte are only able to attain an efficiency relative to a Carnot engine of around 0.5 % [5]. This is mainly due to the small surface area available for the redox reactions to occur on platinum. Through the use of MWNT buckypaper scrolled electrodes, the relative efficiency was increased by almost three fold; yielding a record 1.4 % relative to a Carnot engine [4]. Aside from the larger electroactive area available in the MWNT buckypaper, it is surmised that the scrolled electrode configuration reduces the heat loss channel. Small inter-electrode separations are desirable as the mass transport overpotential is minimized [3]. However, a shorter distance between electrodes requires a larger thermal input to maintain the same thermal gradient, thus reducing thermocell efficiency. Since the scrolled electrode configuration mitigates heat loss, a large thermal gradient can be maintained despite a small inter-electrode separation, thus enhancing both mass transport and efficiency. A schematic diagram of the scrolled electrode thermocell is shown in Figure 4.1. MWNT buckypapers (weighing 0.5 mg) were rolled into a scroll with a diameter of 0.3 cm and placed inside a glass tube. The electrodes were immersed in 0.4 M $K_3Fe(CN)_6/K_4Fe(CN)_6$ solution and kept 5 cm apart. Using T_{hot} =

65 ^{o}C and T_{cold} = 5 ^{o}C, an areal power density of 1.8 W/m^2 was obtained. The power density may be normalised to the temperature gradient to take into account the variation in ΔT used by different systems by using $P_{max}/\Delta T^2$ [4]. Using scrolled electrodes, a normalised power density of 5 x 10^{-4} W/m^2-K^2 and power conversion efficiency of 0.24 % was achieved.

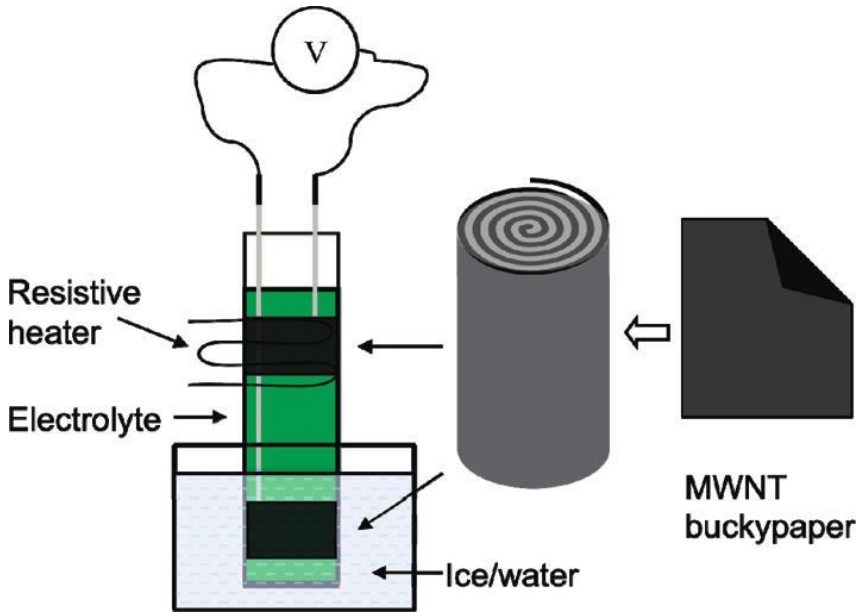

Figure 4.1 Scrolled electrodes for thermocell applications. Reprinted from [4] with permission from American Chemical Society

4.1.2 Coin type thermocells

Thin coin type thermocells which could be powered by extremely low thermal gradients were developed using MWNTs. Nomex separators saturated with 0.4 M $K_3Fe(CN)_6/K_4Fe(CN)_6$ was used to keep the electrodes apart (Figure 4.2).Coin cells fabricated using MWNT buckypaper electrodes and exposed to a thermal gradient of 45 ^{o}C generated an areal power density of 0.389 W/m^2 (equivalent to $P_{max}/\Delta T^2$ of 1.92 x 10^{-4} W/m^2-K^2). Coin cells with electrodes made of MWNT

forests around 100 μm tall, grown directly on the internal stainless steel surface of the packaging substrate using a trilayer catalyst (30 nm Ti, 10 nm Al, 2 nm Fe) plasma enhanced CVD method was also developed. The areal power density generated at a thermal gradient of 60 ^{o}C was 0.980 W/m^2, giving $P_{max}/\Delta T^2$ = 2.72 x 10^{-4} W/m^2-K^2. The larger normalised power density of the coin cell with MWNT forest electrodes is due to its nanotube alignment, which promotes electrolyte diffusion, and the lower thermal (0.01 cm^2-K/W) and electrical resistance at the MWNT forest/substrate junction [6]. The thermal resistance for MWNT buckypapers is around 0.05 cm^2-K/W which leads to larger loss of thermal energy at the electrode/substrate junction and 30 % less power conversion efficiency [7].

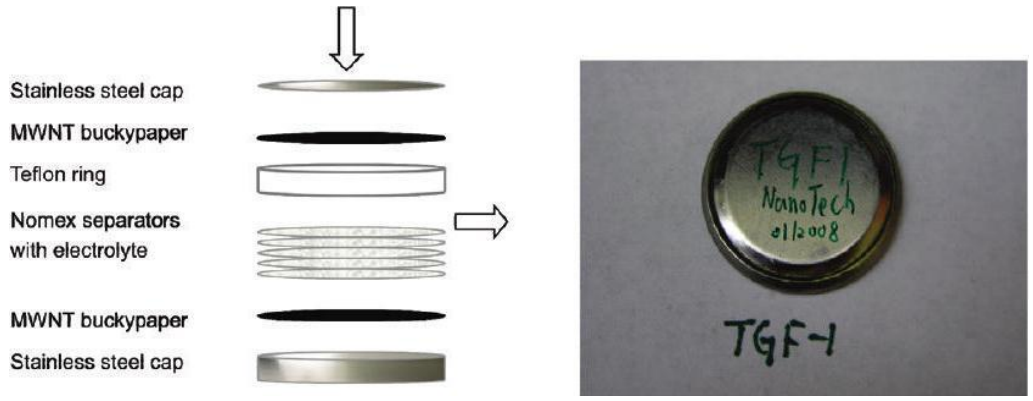

Figure 4.2 Coin type thermocell. Reprinted from [4] with permission from American Chemical Society

4.1.3 Flexible thermocell

Thermocell applications are not limited to situations wherein waste heat is harvested from flat surfaces. Several scenarios exist in which heat may be recovered from irregularly shaped surfaces, such as in heating/cooling pipes in power plants

and car exhaust pipes. One electrode can be placed in contact with the heating/cooling pipe and the other electrode's temperature will be regulated by the surrounding environment. Recently, Hu et al. developed a flexible thermocell [4]. The schematic layout (Figure 4.3a) shows that two layers of Nomex HT 4848 are used to separate the two MWNT buckypaper electrodes. The estimated distance between electrodes is 2 mm. The entire assembly is encased in a stainless steel sheet and held in place by glue and clamps. 0.4 M $K_3Fe(CN)_6/K_4Fe(CN)_6$ solution is injected using a syringe to saturate the Nomex separator with electrolyte, after which the hole is sealed. By wrapping the flexible cell around a cooling pipe with a resistive heater then wrapped around it (Figure 4.3b), an areal power density of 0.039 W/m^2 was generated. A maximum V_{oc} of 21 mV was attained. Using the Seebeck coefficient of the electrolyte (1.4 mV/K) the V_{oc} is equivalent to a thermal gradient of 15 ^oC across the two electrodes. Despite the small separation distance, a relatively large temperature gradient was attained because of the Nomex separator employed. Through the use of this flexible thermocell a $P_{max}/\Delta T^2$ of 1.8 x 10^{-4} W/m^2-K^2 was achieved.

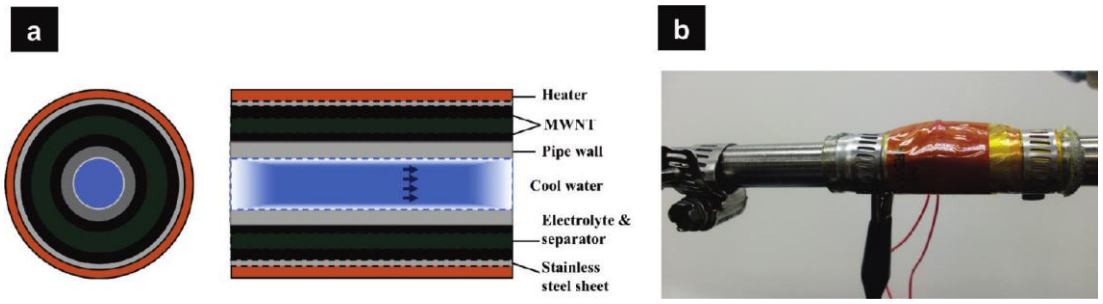

Figure 4.3 a) Schematic and b) photo of a flexible thermocell that can be wrapped around cooling/heating pipes. Reprinted from [4] with permission from American Chemical Society.

4.2 Chapter Aims

In this chapter, various cell designs will be compared in order to determine the optimum configuration for thermocell applications. Unless otherwise stated, power output using thin platinum electrodes will be done so as to obtain results that will not be complicated by accumulation of reaction products that occur inside porous electrodes [2]. Mass transport overpotential in various cell designs will be ascertained by comparing the current output relative to the thermal gradient. Power conversion efficiency will be determined and used to benchmark the various cell configurations

4.3 Experimental setup

Heating and cooling of all cell configurations was done as described previously (Chapter 2, Experimental Theory and Methodology) unless otherwise stated. Platinum electrodes 99.9 % pure and 0.001 inch thick were used in all experiments in this chapter unless stated otherwise. All thermocell configurations were evaluated using 0.4 M $K_3Fe(CN)_6/K_4Fe(CN)_6$ solutions as this has the optimum combination of thermal and ionic conductivity for thermal harvesting [8].

4.4 Results and discussion

4.4.1 H-shaped thermocell

This particular thermocell design is useful as a benchmark to compare against work being done by other groups as they report similar cell configurations in their work [4, 9]. The H-shaped thermocell (Figure 4.4) had the 0.75 cm^2 platinum electrodes spaced 10 cm apart. Thermocouples positioned close to the electrodes were used to monitor/control the temperatures in each half-cell. A quick evaluation of this cell design is to obtain the Seebeck coefficient of the electrolyte and compare it against previously reported values. Keeping T_{cold} constant at 20 ^oC, the V_{oc} was measured at increasing thermal gradients (Figure 4.5). The Seebeck coefficient obtained was 1.47 mV/K, which is in good agreement with values reported in literature (1.4 mV/K) [10, 11].

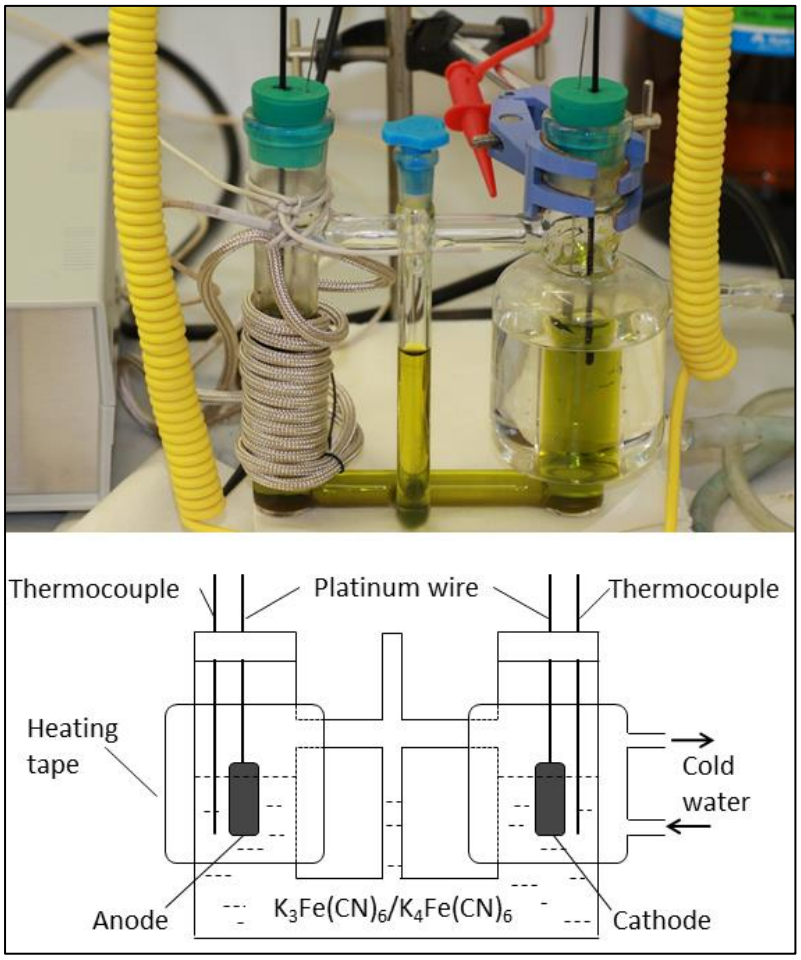

Figure 4.4 Photo and schematic of the H-shaped thermocell

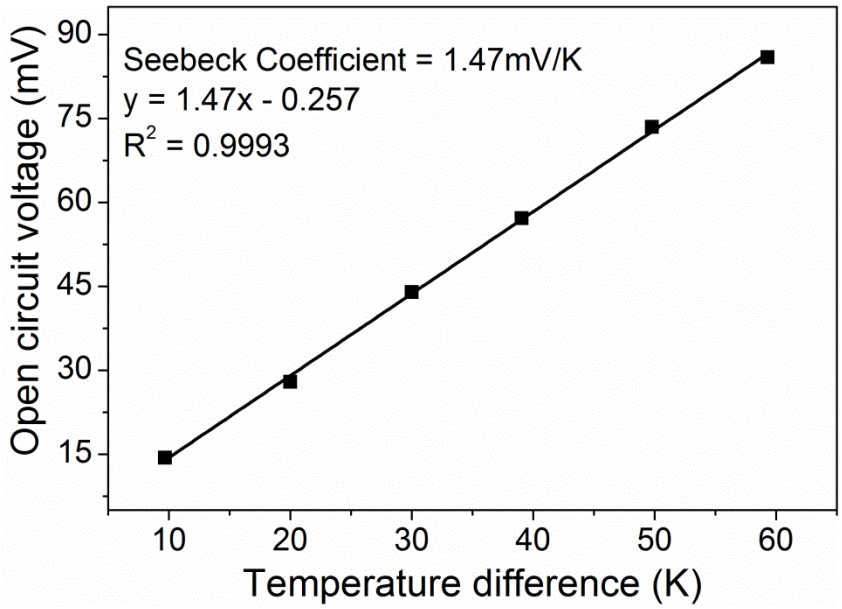

Figure 4.5 Seebeck coefficient of 0.4 M $K_3Fe(CN)_6/K_4Fe(CN)_6$ measured using the H-shaped thermocell with platinum electrodes.

Using T_{hot} = 80 ^oC and T_{cold} = 20 ^oC, an areal current density of 4.54 A/m^2 and areal power density of 95.3 mW/m^2 was attained (Figure 4.6). Normalising both current and power density to the thermal gradient gives $I_{max}/\Delta T$ = 0.076 A/m^2-K and $P_{max}/\Delta T^2$ = 2.65 x 10^{-5} W/m^2-K^2 respectively. Using a similar cell design and platinum electrodes, Hu et al. reported a $I_{max}/\Delta T$ of 0.81 A/m^2-K and $P_{max}/\Delta T^2$ of 2.8 x 10^{-4} W/m^2-K^2 [4]. Both values are higher than that obtained in this experiment by about an order of magnitude. The disparity can be accounted for by the electrode separation used by Hu et al. (5 cm), which is half that used here. This decreased distance between electrodes lowers the mass transport overpotential (as evidenced by the higher $I_{max}/\Delta T$) and increases power output. The power conversion efficiency (Φ) measured using the H-shaped thermocell was 0.029 %, which corresponds to an efficiency relative to a Carnot engine (Φ_r) of 0.171 %.

It must be noted that a relatively large amount of electrolyte is required for the H-shaped cell (around 60 ml). Experiments wherein it would be very costly to produce large amounts of the electrolyte, i.e. involving ionic liquids, would not be feasible to run in this thermocell. The electrode spacing is also quite large for this cell configuration, which leads to decreased power output owing to the large mass transfer overpotential. These limitations need to be addressed to efficiently harness waste thermal energy.

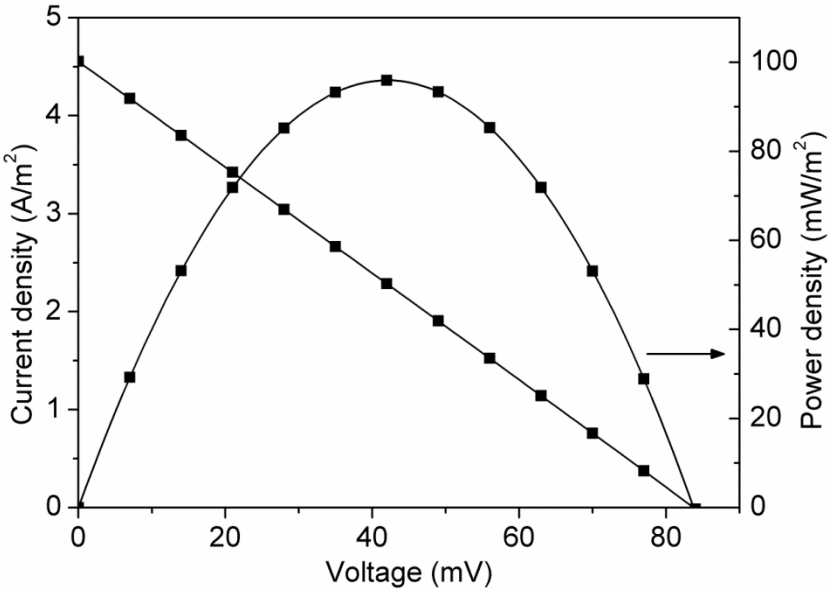

Figure 4.6 J-V curves generated using the H-shaped thermocell with platinum electrodes, T_{hot} = 80 ^{o}C and T_{cold} = 20 ^{o}C.

4.4.2 U-shaped thermocell

The possibility of using a thermocell that utilises a small volume of electrolyte was explored using a U-shaped thermocell (Figure 4.7). As mentioned in the previous section (4.4.1), this could be used in experiments wherein the amount of electrolyte available for testing is limited. Platinum electrodes with an area of

0.7 cm^2 were separated by a distance of 2 cm for this particular cell configuration. The amount of electrolyte needed was around 2 ml. Measurement of the Seebeck coefficient of the 0.4 M $K_3Fe(CN)_6/K_4Fe(CN)_6$ used yielded a value of 1.41 mV/K (Figure 4.8), which is in good agreement with literature [10, 11].

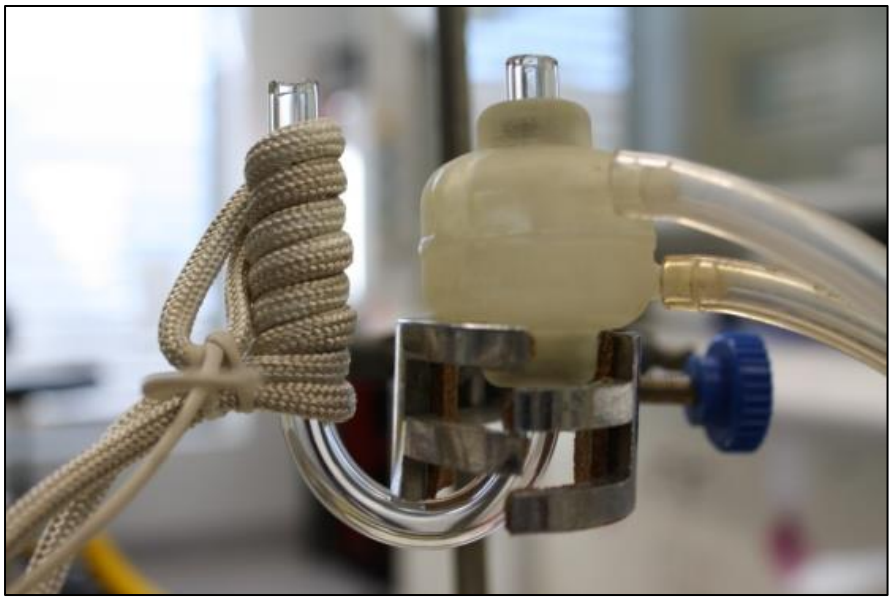

Figure 4.7 Assembled U-shaped thermocell showing the cooling jacket and heating rope

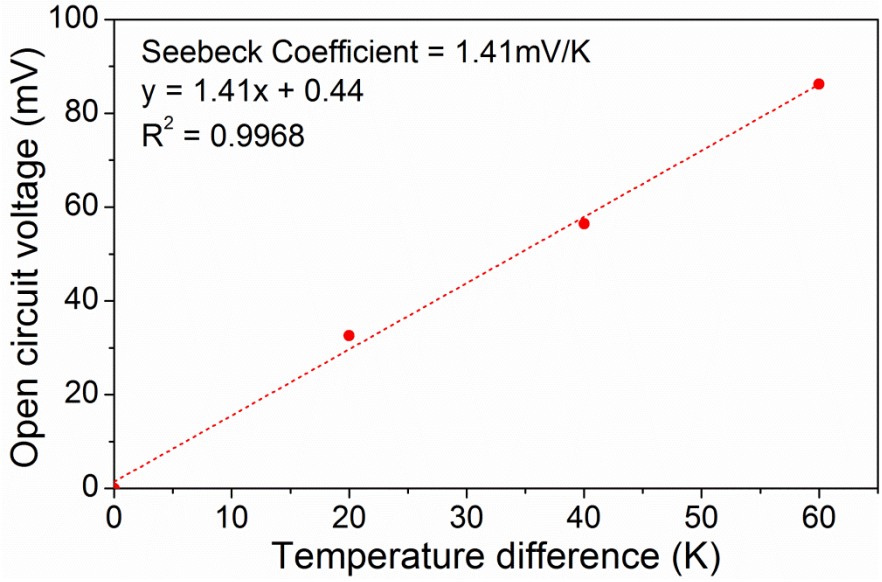

Figure 4.8 Seebeck coefficient of 0.4 M $K_3Fe(CN)_6/K_4Fe(CN)_6$ measured using the U-shaped thermocell with platinum electrodes.

Using a thermal gradient of 60 ^oC, with T_{hot} = 80 ^oC and T_{cold} = 20 ^oC, areal current density of 4.19 A/m^2 and areal power density of 90.7 mW/m^2 were measured. Normalising both values to the temperature gradient yielded $I_{max}/\Delta T$ = 0.070 A/m^2-K and $P_{max}/\Delta T^2$ = 2.52 x 10^{-5} W/m^2-K^2. These values indicate that the power output at the settings used of the U-shaped and H-shaped thermocells are similar. The smaller electrode separation in the U-shaped cell was expected to augment the power density as reaction products produced at the cathode have to travel only a shorter distance to reach the anode (and vice versa) [2, 3]. It is surmised that the position of the electrodes, wherein they are situated above the bend in the U-shaped thermocell increased the mass transport overpotential thus resulting in the same current generation capabilities of both H and U-shaped cell. Ferricyanide formed at the hot side needs to travel down the bend in the cell and then ascend the tube to reach the cold side wherein it will be consumed. This is also true for the opposite reaction; i.e. that involving ferrocyanide. The hindrance to mass transport could have resulted in

accumulation of reaction products at the bottom of the cell thus reducing the current and power produced.

The Φ obtained when using the U-shaped cell (0.003 %) is an order of magnitude lower than that of the H-shaped cell (0.029 %). Similarly, the Φ_r (0.019 %) of the U-shaped cell is less than that of the H-shaped cell (0.171 %). This disparity is due to the close proximity of the electrodes in the U-shaped cell. It must be noted that while one half-cell is being heated, the other half-cell is being actively cooled. If active cooling was not employed then the thermal gradient in the U-shaped thermocell would be smaller than the H-shaped cell and thus yield a lower power density. Nevertheless, the U-shaped thermocell is a feasible option for evaluation of the Seebeck coefficient of electrolytes. The potential generated at a given thermal gradient is dependent on the entropy of the redox couple and is unaffected by the mass transport overpotential.

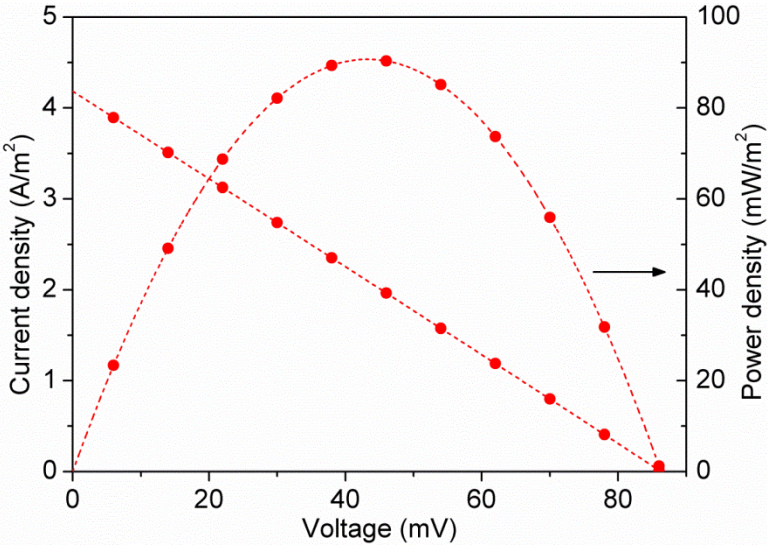

Figure 4.9 J-V curves generated using the U-shaped thermocell with platinum electrodes, T_{hot} = 80 ^{o}C and T_{cold} = 20 ^{o}C.

4.4.3 T-shaped thermocell

In order to efficiently harness waste heat, a cell configuration is needed that will not require the large electrolyte volume associated with the H-shaped thermocell and will not have issues associated with mass transport as was exhibited by the U-shaped thermocell. Ideally electrodes should be facing each other and separated by a relatively small distance [2]. The T-shaped thermocell was developed to address the limitations of the two previous thermocell designs. This thermocell (Figure 4.10) consisted of two stainless steel bars, a teflon T-piece (Swagelock) and a 2 cm long teflon spacer.

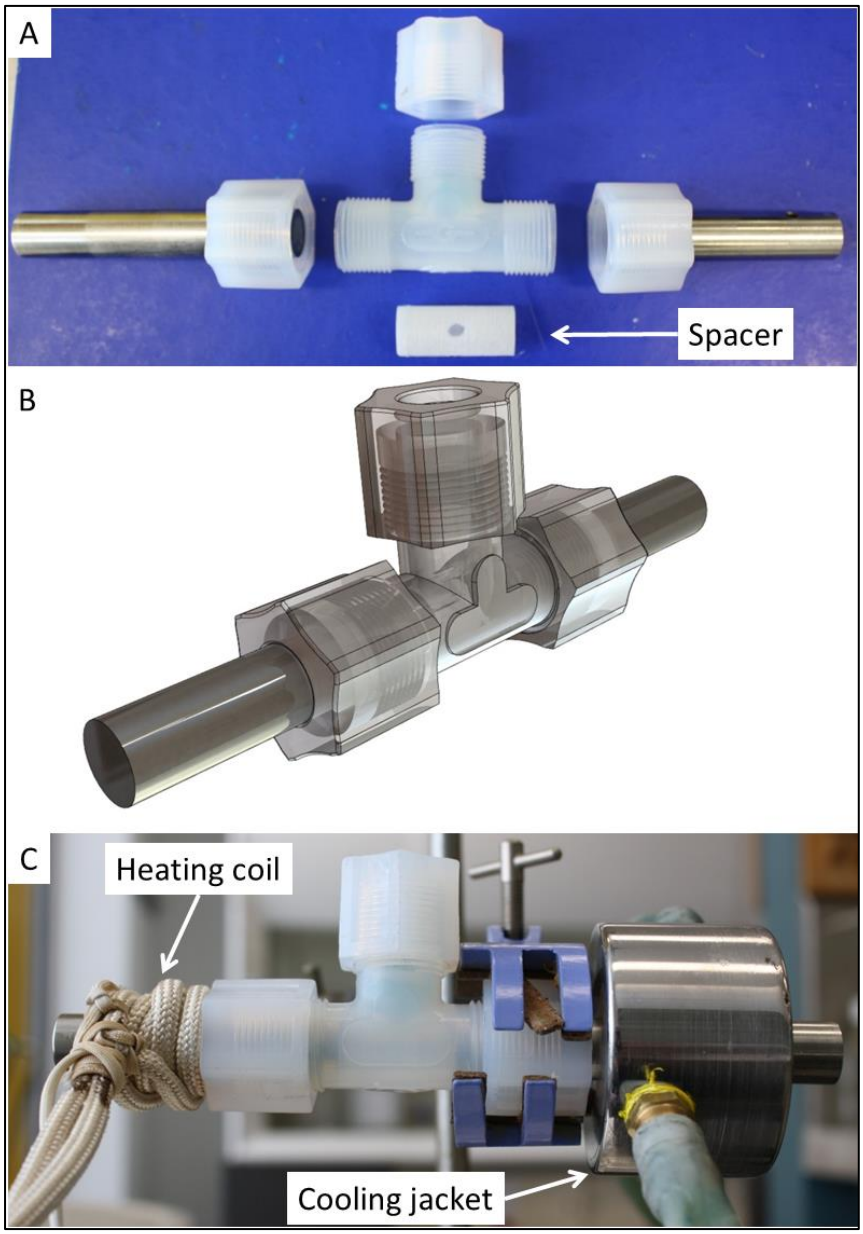

Figure 4.10 T-shaped thermocell: A) disassembled showing various components, B) schematic diagram, and C) assembled with heating coil and cooling jacket.

The 0.35 cm^2 platinum electrodes were sandwiched against the stainless steel bar and the teflon spacer and held in place by stainless steel mesh. A heating rope and cooling jacket were placed in contact with the stainless steel bars to actively maintain the thermal gradient. Thermocouples could not be placed adjacent to the electrodes without causing leakage in the thermocell. Instead, the temperature

gradient was calculated from the V_{oc} measured using the reported value of the Seebeck coefficient (1.4 mV/K) of the electrolyte (0.4 M $K_3Fe(CN)_6/K_4Fe(CN)_6$).

Applying a temperature of 100 ^oC to the hot side and 16 ^oC to the cold side of the thermocell resulted in V_{oc} = 43.8 mV (Figure 4.11) which corresponds to a ΔT of 31.3 ^oC; almost three times lower than the expected value (84 ^oC). The low thermal gradient was due to the close proximity of the two electrodes which allowed a large thermal flux between the hot and cold side. The process in which active cooling was applied also contributes to the diminished temperature gradient. The cooling jacket was positioned such that it was not near the electrode; thus allowing heat transfer across the cell. Thermal resistance due to inadequate contact between the heating rope/cooling jacket and their respective stainless steel bars also lessened the temperature difference in the cell.

Regardless of the low ΔT, it must be noted that the T-shaped thermocell attained the highest areal current and power density (17.48 A/m^2 and 198 mW/m^2 respectively) among the three cell configurations discussed so far. This corresponds to $I_{max}/\Delta T$ = 0.564 A/m^2-K and $P_{max}/\Delta T^2$ = 2.07 x 10^{-4} W/m^2-K^2. Both values are almost an order of magnitude higher than that attained by the two previous cell designs. Compared to the H-shaped cell, the T-shaped thermocell used a fifth of the electrode separation distance. The close proximity of the electrodes minimised the mass transfer overpotential as ions had to travel a short distance to get from one half-cell to the other. Despite having the same separation distance in both the T-shaped and U-shaped cell configuration, the latter had electrodes that were positioned such that convection cannot readily occur. As mentioned previously, the low current density in the U-shaped cell may be attributed to the accumulation of reaction

products at the bottom of the cell, thus the redox reactions necessary for thermal energy conversion did not occur readily. In the T-shaped thermocell both electrodes were facing each other and were on the same plane as that which diffusion occurs. The positioning of electrodes in this manner promoted convection in the cell and enhanced ion migration, evidenced by the significantly higher $I_{max}/\Delta T$ [12]. In other words, the enhanced performance of the T-shaped cell compared to the two previous cell configurations may be attributed to the ease with which reaction products formed at the anode could travel to the cathode (and vice versa). This allowed the redox reactions necessary for thermal energy conversion to readily occur, resulting in a large current and power density.

The T-shaped thermocell attained an Φ of 0.023 %, which corresponds to a Φ_r of 0.282 %. Comparison of the different Φ_r results reveals a 65 % improvement compared to the H-shaped cell and a remarkable 1384 % improvement compared to the U-shaped cell. The high current density coupled with the low effective thermal gradient in the T-shaped cell resulted in very efficient conversion of thermal energy. Owing to these advantages, the T-shaped thermocell is ideal for comparing the performances of various carbon-based electrode materials. The fact that this cell configuration uses very small amounts of electrolyte (around 2 ml) is also advantageous in that it can be used to test the thermocell performance of ionic liquids.

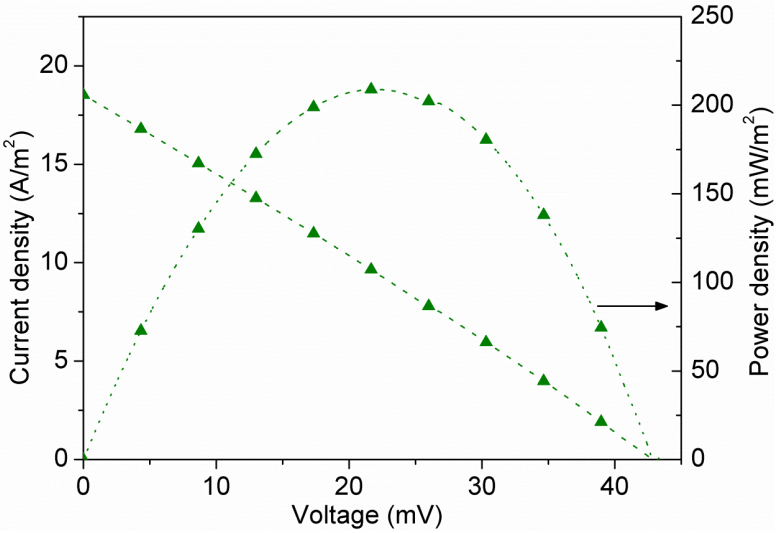

Figure 4.11 J-V curves generated using the T-shaped thermocell with platinum electrodes.

4.4.4 Series thermocell

It has been demonstrated that with the T-shaped thermocell appreciable amounts of power may be generated by these devices. However, for certain applications a significant quantity of voltage is required. For thermocells, the voltage generated is dependent on the structural entropy induced by ion and solvent interactions [13]. One way to augment the voltage produced is to connect these devices in series. A proof of this concept was demonstrated through the use of a thermocell with three electrode chambers, each capable of holding 3 ml of electrolyte (Figure 4.12A). The cell body (Figure 4.13A) was made of a polymer called MED 610 printed using an Objet Connex 350 3D Printer (a detailed discussion is provided in Chapter 2) [14]. Three pairs of titanium sheet electrodes, having dimensions of 1.5 cm x 0.5 cm, were immersed in 0.4 M $K_3Fe(CN)_6/K_4Fe(CN)_6$ and connected in series (Figure 4.12B). The spacing between anode and cathode was 2 cm. The temperature was regulated by peltier

modules with heat sinks attached (Figure 4.13B). The temperature was monitored by thermocouples that were also submerged in the electrolyte at the same distance from the peltier as the electrodes. Figure 4.12C shows the holes in the series thermocell cover wherein the thermocouples were inserted. The assembled device is shown in Figure 4.13C and D.

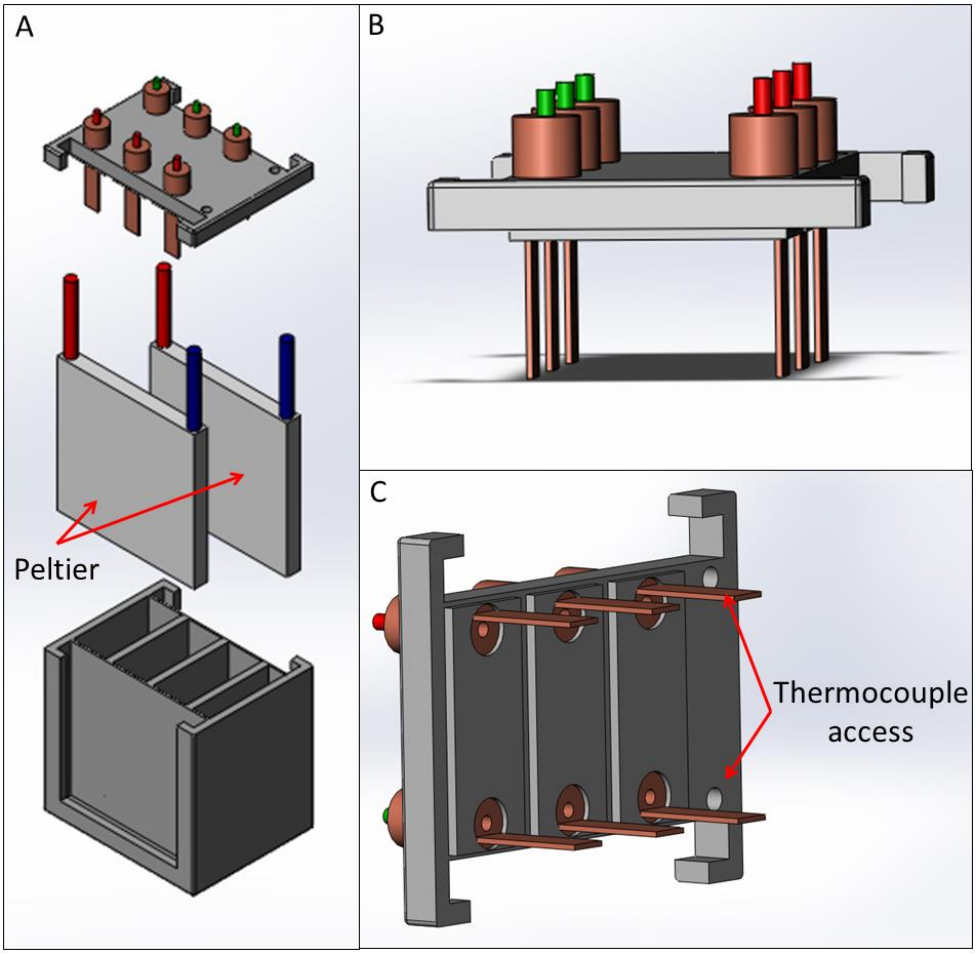

Figure 4.12 Schematic of the series thermocell showing: A) individual components, B) and C) the cover and electrodes

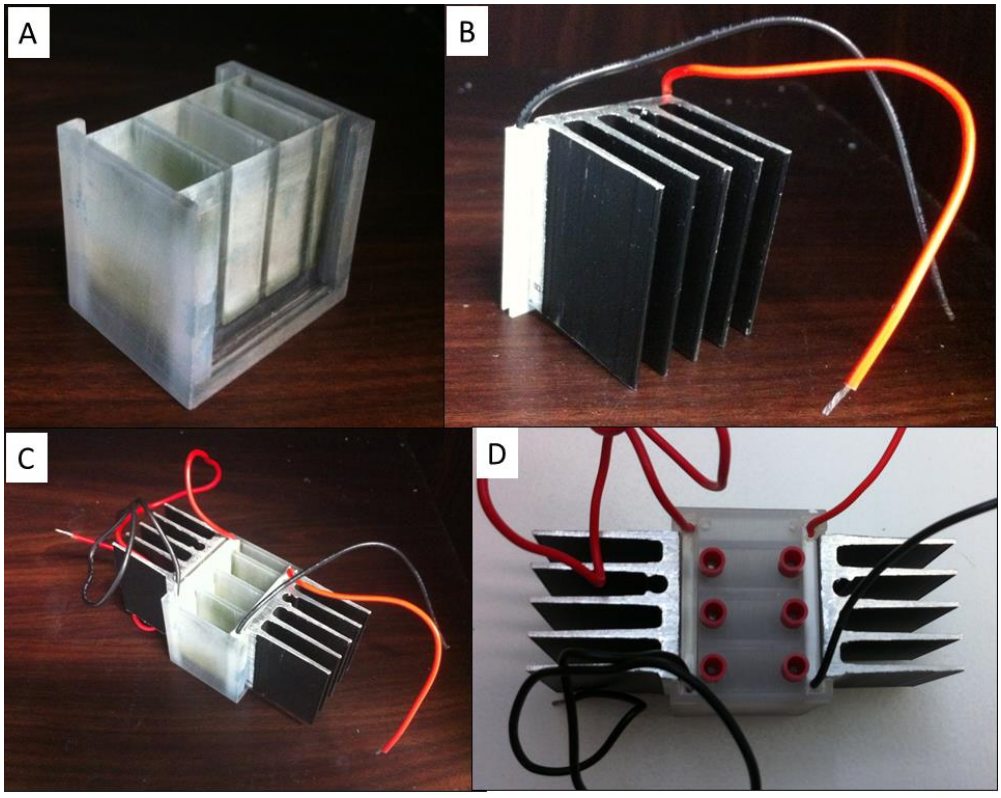

Figure 4.13 Photos of the series thermocell showing: A) electrolyte chambers, B) peltier with heatsink attached, C and D) various views of the assembled device

The temperature of the heating peltier was set to 50 ^{o}C and that of the cooling peltier was set to 20 ^{o}C. J-V curves (Figure 4.14) generated by each cell display similar values with V_{oc} at 3.85 mV, an areal current density of 2.70 A/m^2, and an areal power density of 2.66 mW/m^2. The V_{oc} corresponds to a ΔT of 2.75 ^{o}C, which is in good agreement with the measurements obtained from the thermocouples which were indicating T_{hot} = 33.3 ^{o}C and T_{cold} = 30.4 ^{o}C. Using the temperatures of the peltier modules, the thermal gradient should be around 30 ^{o}C. The low value of ΔT may be attributed to the material which the thermocell body is made of. Using a TCi Thermal Conductivity Analyzer, the thermal conductivity of MED 610 was measured to be 0.437 W/m-K [15]. The low thermal conductivity of MED 610 blocks most of the heat being supplied to the hot side of the thermocell. Instead of

obtaining a T_{hot} of 50 ^{o}C only 33.3 ^{o}C was measured. The low thermal conductivity also inhibits active cooling of the cold side; which is evidenced by the measured T_{cold} of 30.4 ^{o}C as opposed to the theoretical value of 20 ^{o}C. These factors resulted in a very low thermal gradient across the series thermocell.

Despite the low thermal gradient, J-V curves generated by the three cells in series (Figure 4.15) indicate a 3-fold increase in voltage, reaching up to 11.3 mV. The areal current density measured was 2.54 mA/cm^2. It must be noted that there is a slight drop in areal current density generated by the three cells in series as compared to that measured from each individual cell (2.70 A/m^2). This small decline in current may be attributed to ohmic losses, i.e. contact resistance. The areal power density measured was 6.73 mW/m^2, equivalent to $P_{max}/\Delta T^2$ of 8.90 x 10^{-4} W/m^2-K^2. The series thermocell attained an Φ of 0.009 %, which corresponds to a Φ_r of 0.997 %. The Φ_r achieved through the use of the series cell is a ~254 % improvement as compared to the T-shaped thermocell (Φ_r = 0.282 %). This marked increase indicates the feasibility of connecting thermocells in series. With the appropriate cell design, i.e. use of materials that conduct heat better than MED 610, the power output can be considerably augmented.

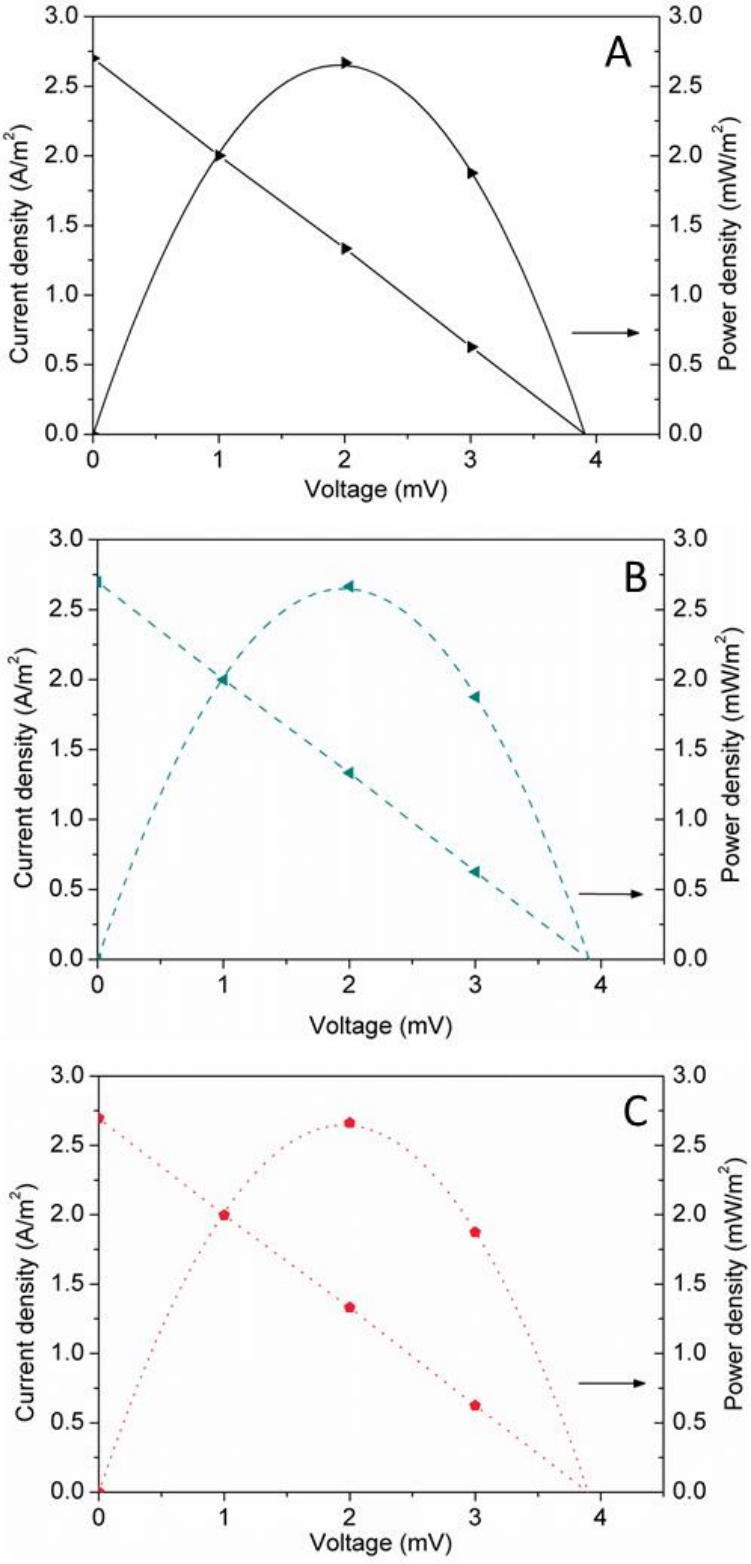

Figure 4.14 J-V curves generated by the individual chambers of the series thermocell with titanium electrodes

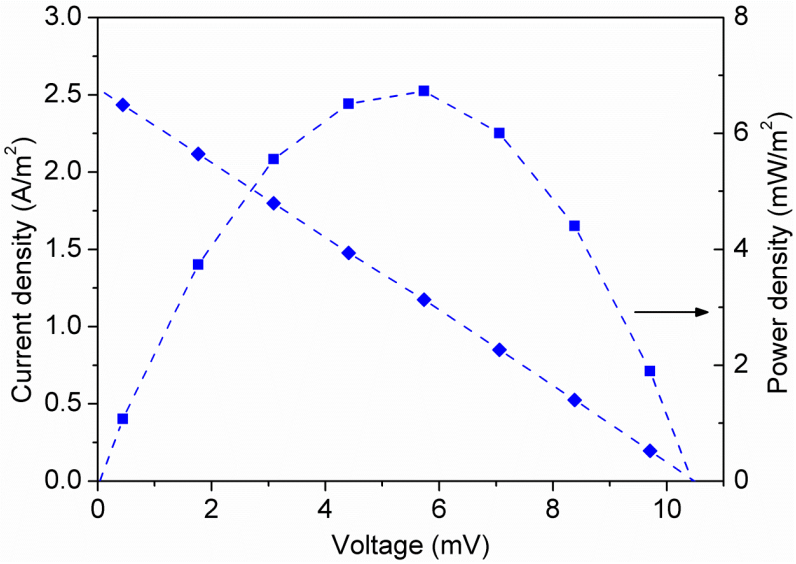

Figure 4.15 J-V curve generated by the series thermocell (three chambers connected in series) with titanium electrodes

4.5 Conclusion

A variety of thermocell configurations have been investigated using non-porous electrode materials. A summary of data obtained is provided in Table 4.1 below.

Table 4.1 Summary of data obtained from thermal harvesting experiments performed using various cell designs

Cell configuration	H-shaped thermocell	U-shaped thermocell	T-shaped thermocell	Series thermocell
ΔT (K)	60	60	31.3	2.9
Areal current density (A/m^2)	4.541	4.185	17.484	2.542
$I_{max}/\Delta T^2$ (A/m^2-K^2)	0.076	0.070	0.564	0.924
Areal power density (mW/m^2)	95.3	90.7	198	6.73
$P_{max}/\Delta T^2$ (W/m^2-K^2)	2.65×10^{-5}	2.52×10^{-5}	2.07×10^{-4}	8.90×10^{-4}
Φ (%)	0.029	0.003	0.023	0.009
Φ_r (%)	0.171	0.019	0.282	0.997

Cell configuration plays an important role in decreasing the mass transport overpotential. Electrodes should be positioned such that reaction products from the cathode are able to diffuse readily to the anode, and vice versa. If electrodes are not positioned in such a manner then the current and power generated by the thermocell will be decreased. The T-shaped thermocell generates the largest amount of power for a given thermal gradient among all the "single" cell designs considered. The fact that this cell configuration does not require extensive amounts of electrolyte makes it attractive for testing ionic liquids (which are expensive to produce in large amounts). By connecting thermocells in series, i.e. using the series cell, power output is significantly augmented. Further improvements in thermocell design will see these devices being used in practical applications to harvest waste heat.

4.6 References

1. Reddy, R., *Ionic liquids: How well do we know them?* Journal of Phase Equilibria and Diffusion, 2006. **27**(3): p. 210-211.
2. Kang, T.J., et al., *Electrical Power From Nanotube and Graphene Electrochemical Thermal Energy Harvesters.* Advanced Functional Materials, 2012. **22**(3): p. 477-489.
3. Mua, Y. and T.I. Quickenden, *Power Conversion Efficiency, Electrode Separation, and Overpotential in the Ferricyanide/Ferrocyanide Thermogalvanic Cell.* Journal of The Electrochemical Society, 1996. **143**(8): p. 2558-2564.
4. Hu, R., et al., *Harvesting Waste Thermal Energy Using a Carbon-Nanotube-Based Thermo-Electrochemical Cell.* Nano Letters, 2010. **10**(3): p. 838-846.
5. Quickenden, T.I. and Y. Mua, *A Review of Power Generation in Aqueous Thermogalvanic Cells.* Journal of The Electrochemical Society, 1995. **142**(11): p. 3985-3994.
6. Myounggu, P., et al., *Effects of a carbon nanotube layer on electrical contact resistance between copper substrates.* Nanotechnology, 2006. **17**(9): p. 2294.
7. Cola, B.A., et al., *Photoacoustic characterization of carbon nanotube array thermal interfaces.* Journal of Applied Physics, 2007. **101**(5): p. 054313-9.
8. Romano, M., et al., *Novel carbon materials for thermal energy harvesting.* Journal of Thermal Analysis and Calorimetry, 2012. **109**(3): p. 1229-1235.

9. Salazar, P.F., S. Kumar, and B.A. Cola, *Nitrogen- and Boron-Doped Carbon Nanotube Electrodes in a Thermo-Electrochemical Cell.* Journal of The Electrochemical Society, 2012. **159**(5): p. B483-B488.

10. Hirai, T., K. Shindo, and T. Ogata, *Charge and Discharge Characteristics of Thermochargeable Galvanic Cells with an* $[Fe(CN)6]^{4-}/[Fe(CN)6]^{3-}$ *Redox Couple.* Journal of The Electrochemical Society, 1996. **143**(4): p. 1305-1313.

11. Quickenden, T.I. and C.F. Vernon, *Thermogalvanic conversion of heat to electricity.* Solar Energy, 1986. **36**(1): p. 63-72.

12. Quickenden, T.I. and Y. Mua, *The Power Conversion Efficiencies of a Thermogalvanic Cell Operated in Three Different Orientations.* Journal of The Electrochemical Society, 1995. **142**(11): p. 3652-3659.

13. Bonetti, M., et al., *Huge Seebeck coefficients in nonaqueous electrolytes.* The Journal of Chemical Physics, 2011. **134**(11): p. 114513-8.

14. Stratasys. *How PolyJet 3D Printing Works.* 2013 [cited 2013; Available from: http://www.stratasys.com/3d-printers/technology/polyjet-technology.

15. *C-Therm Technologies Ltd.C-Therm Technologies-Products*. Available from: http://www.ctherm.com/products/tci_thermal_conductivity

CHAPTER 5

Nano-carbon Composite Electrodes and Vascular Electrodes for Thermocells

5.1 Introductory remarks

Initial research on thermocells has been focused on the use of platinum electrodes, the archetypal non-reactive catalytic material [1-3]. In order to make thermocells commercially viable, the electrode material needs to be replaced such that the price per Watt is minimised. Studies on the electrochemistry of carbon nanomaterials, namely carbon nanotubes (CNTs) and reduced graphene oxide (rGO), reveal that they exhibit fast electron transfer kinetics and Nernstian behaviour with the $K_3Fe(CN)_6/K_4Fe(CN)_6$ redox couple [4, 5]. These carbon materials have been studied individually in thermocell applications with promising results [6-8]. The main advantage of using carbon nanomaterials is the porous nature of the resulting electrode material; more so in CNTs than rGO [8]. Porous materials are desirable as they have a larger active area as opposed to flat electrodes, allowing the possibility of a higher exchange current density between the electrode and electrolyte. Thus porous electrodes facilitate the generation of larger net current densities than flat materials [7].

However, ion accessibility must also be taken into consideration. To ensure continuous generation of power in a thermocell, reaction products formed at one half-cell must be transported to the opposite side. If either electrode is not supplied

with the redox species needed for electron generation or consumption then power generation will diminish [9]. This mass transport effect is exacerbated in pure CNT and rGO electrodes owing to the tortuous nature of the former and sheet restacking in the latter [7].

Materials that possess a vascular structure may result in increased thermocell performance owing to their larger active area. Carbon cloth, which consists of carbon fibres that are woven in the form of cloth, is one such material [10]. It has several properties that make it attractive for thermocell electrode applications such as: low electrical resistance, light weight, high porosity, chemical and thermal stability, good mechanical strength, and high degree of flexibility [11].

5.2 Chapter Aims

In this chapter the porosity of thermocell electrodes is tailored through the use of CNTs, more specifically single-walled nanotubes (SWNT), and rGO composites. Upon optimising the electrode composition, the electrode thickness is varied in order to increase the electroactive surface area. Thermocell power conversion efficiency using the optimised carbon electrode is compared to that of platinum to gauge device performance.

The investigation of the use of carbon cloth as electrodes for thermocells is also done in this chapter. The best performing composite of SWNT and rGO is integrated into these vascular structures using various methods. Comparison of the thermocell performance resulting from the use of the different developed electrodes is done to determine the optimum electrode structure

5.3 Experimental setup

5.3.1 SWNT-rGO composite preparation

A schematic of the SWNT-rGO composite preparation procedure is shown in Figure 5.1.

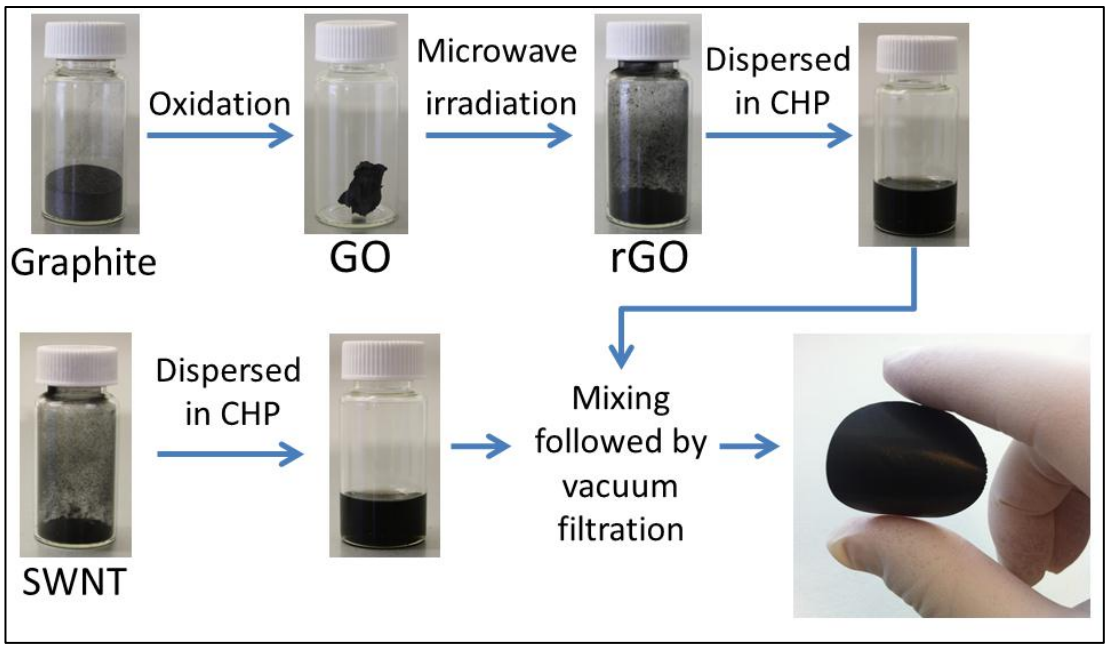

Figure 5.1 SWNT-rGO composite preparation procedure

SWNTs were dispersed using 1-cyclohexyl-2-pyrrolidone (CHP) at a concentration of 1 mg/ml using a combination of bath (Branson B1500R-MT) and probe sonication (Branson probe sonifier). More details on the dispersion procedure can be found in Chapter 2. CHP was selected because only mild sonication conditions are necessary in order to facilitate SWNT exfoliation, thus reducing the damage to the tubes by cutting [12]. The dispersion was left overnight for re-aggregation to occur after which mild centrifugation (Eppendorf Centrifuge 5415 D)

was done for 90 minutes at 2500 rcf to remove large aggregates. The concentration of the supernatant was determined via Ultraviolet-Visible Spectroscopy (UV-Vis) using a Shimadzu UV-1800 spectrophotometer. The sample was then diluted to a concentration of 0.4 mg/ml.

Graphene oxide (GO) was synthesized using a modified Hummers method developed by Marcano et. al. [13]. Exfoliation of the dried GO was done in two steps; it was first heated in a commercial microwave (Panasonic Inverter 'The Genius' 1200W ©) for 10 seconds. The effects of irradiation can clearly be seen in Figure 5.1, wherein the GO underwent a significant increase in volume after microwave exposure. This volume change was induced by the expulsion of moisture and other intercalated compounds in the GO structure [14, 15]. The resulting reduced graphene oxide (rGO) powder was then further exfoliated in CHP using a sonication procedure similar to that described in the previous section on SWNT dispersion.

In order to determine the optimum electrode composition for thermocell applications, SWNT-rGO composites were prepared in the ratios shown in Table 5.1. This was done by mixing dispersions of SWNT and rGO via bath sonication for 90 minutes. Films having a mass of 0.5 mg (1 μm thickness) were then made using vacuum filtration on Millipore polyvinylidene fluoride membrane with a pore size of 0.1 μm. Electrodes were then prepared with a geometric area of 0.785 cm^2.

Table 5.1 Composition of the SWNT-rGO electrodes used

wt % SWNT	100	95	90	80	0
wt % rGO	0	5	10	20	100

Once the ideal composition was determined, films of increasing thicknesses were prepared using the same method in order to fully optimise the composite electrode. Film thickness was controlled by increasing the mass of active material using the following settings: 0.5, 1, 2, 4, 6, and 10 mg, resulting in thicknesses (Veeco Dektak 150 optical profilometer) of: 1, 1.5, 2.5, 4.5, 6.5, and 10.5 μm. All films were plasma treated in air for 20 minutes to ensure complete wetting of the electrode.

5.3.2 Integration of the SWNT-rGO composite with the carbon cloth

The 90-10 composite was integrated with the commercially available carbon cloth by vacuum filtration and dip coating. Dip coating was done using 1, 5 and 10 layers. After dipping the carbon cloth in the 90-10 dispersion it was dried at 300 ^{o}C before adding another layer. Electrodes were also annealed at the same temperature prior to testing to ensure complete removal of the CHP.

5.3.3 Thermocell testing

For thermal harvesting experiments, one half of the cell was cooled using circulating liquid and the other half was heated using an Omegalux Rope Heater (accuracy ± 1 ^{o}C) connected to a TCA Control Box that has 48 x 48 Controller with PID control action and 25 amp Solid State relay. Thermocell testing was done using a T-shaped thermocell, as this was established in Chapter 4 to produce the highest power density of all cell configurations studied. A schematic of the T-shaped thermocell with the carbon composite electrode is shown in Figure 5.2. Electrodes

are held in place by stainless steel mesh. The temperature gradient used was ~31 ^{o}C and electrode separation was 2 cm. The electrolyte used in all thermal harvesting tests was 0.4 M $K_3Fe(CN)_6/K_4Fe(CN)_6$ in aqueous media. This concentration was selected as it has the ideal combination of thermal and electrical conductivity for thermocells; i.e. low thermal and high electrical conductivity [6]. Current density-Voltage (J-V) curves were generated using a Keithley 2400 sourcemeter and customised LabView software.

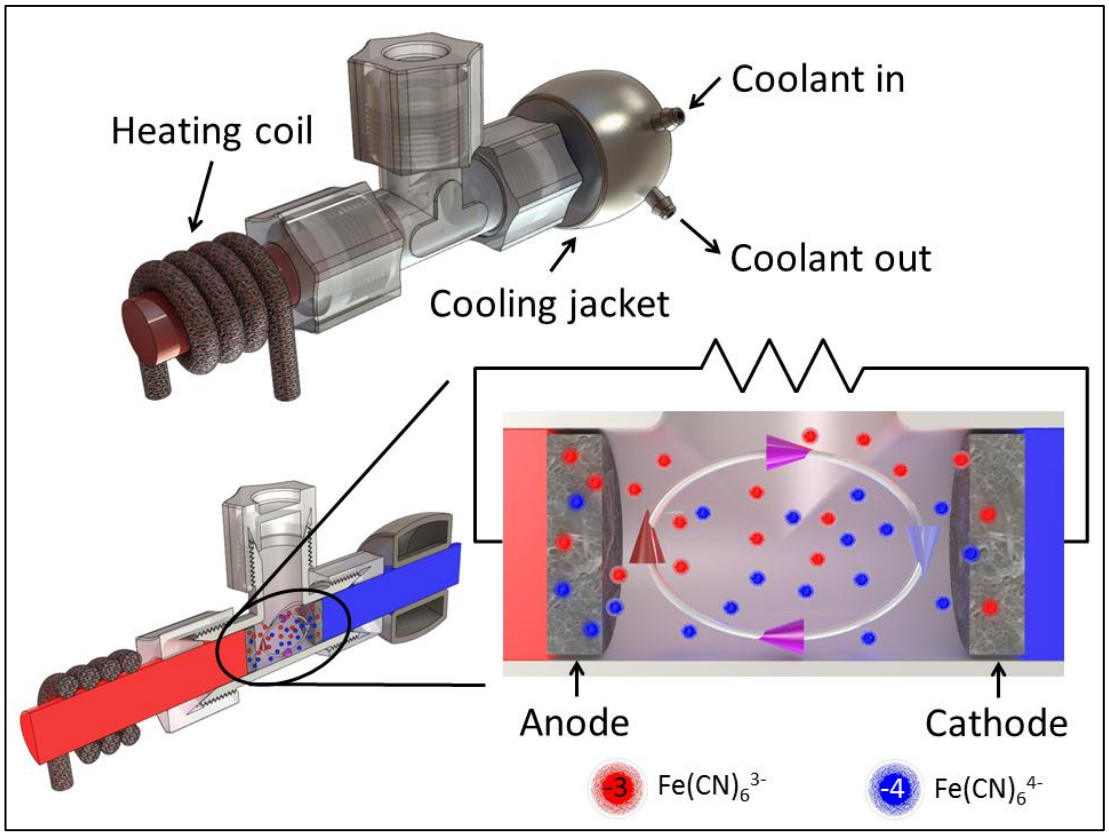

Figure 5.2 Schematic of a T-shaped thermocell with a carbon composite electrode

5.3.4 Characterisation

The structure of the electrodes was probed using a Raman JY HR800 spectrometer. Sample morphology was investigated using a JEOL JSM-7500FA Field Emission Scanning Electron Microscope (SEM). Cyclic voltammetry and electrochemical impedance spectroscopy (EIS) were done using an EDAQ Potentiostat e-corder 401 and Gamry Instruments V.5.58 respectively; wherein three-electrode tests were run at 20 ^{o}C with a Ag/AgCl reference electrode and platinum mesh counter electrode. EIS was measured in the frequency range of 100 kHz-10 mHz with an AC amplitude of 10 mV (rms). Both cyclic voltammetry and EIS were run using 0.01 M $K_3Fe(CN)_6$ with 0.1 M $NaNO_3$ as the supporting electrolyte in aqueous media. This concentration was selected in order to reduce the ohmic overpotential in the cell so as to obtain meaningful information on the electrochemical performance of the prepared electrodes.

5.4 Results and discussion

5.4.1 Improving hydrophilicity of electrodes

In order to ensure optimum wettability of the carbon based electrodes, plasma treatment in air was done. The as-prepared film (Figure 5.3A) showed a water droplet with a contact angle ~ 97^{o}. After 10 minutes of plasma treatment, increased hydrophilicity was observed (Figure 5.3B); i.e. the contact angle decreased in the films. At a plasma treatment time of 20 minutes the contact angle could not be measured (Figure 5.3C), indicating that the carbon film was hydrophilic. Having

hydrophilic electrodes is critical in thermocell applications as this will allow maximum interaction between the electrode and aqueous electrolyte.

Figure 5.3 Increased hydrophilicity for A) as-prepared, B) 10 minutes, C) 20 minutes plasma treatment of carbon electrodes.

5.4.2 Optimisation of SWNT-rGO composition

5.4.2.1 Raman spectroscopy of various SWNT-rGO compositions

The bands of importance in the Raman spectra of the SWNT-rGO samples (Figure 5.4) are the D (~1350 cm^{-1}) and G bands (~1600 cm^{-1}). The D band is indicative of defects that may be associated with the edges of the sheet or defects on the basal plane and is associated with the order or disorder of the sample [16]. One way to measure the defects in the rGO structure is by comparing the D-to-G band intensity ratio (I_D/I_G) [17]. Raman spectra of the rGO sample reveal that it has $I_D/I_G = 1.316$. This implies that the sample has structural imperfections that may be attributed to the vacancies and topological defects introduced during the thermal reduction, and the residual oxygen containing functional groups (introduced during the oxidation step of rGO synthesis) that act as defects on the basal plane and edges of the rGO sheets [18]. Raman spectra of the SWNT-rGO composites are similar to that of pure SWNT as the composites used were predominantly composed of

SWNTs. It is worth noting that comparison of I_D/I_G (Table 5.2) indicates a slight increase in the ratio (from 0.104 for pure SWNT to 0.155 for 80 % SWNT) as the amounts of rGO added to the sample was increased. This is caused by the increase in defective sites associated with the rGO sheets.

The peaks that appear in the low frequency spectra correspond to the radial breathing mode and are inherent in SWNTs. These arise from the vibration of carbon atoms along the SWNT tube/bundle diameter [19, 20]. The pure SWNT film used has three distinct peaks at 219.74 cm^{-1}, 258.41 cm^{-1}, and 284.20 cm^{-1}. The SWNT bundle diameter can be estimated using Equation 5.1 [21].

$$d = \frac{248}{\omega} \qquad \text{Equation 5.1}$$

Where d is the SWNT bundle diameter in nm and ω is the wavenumber in cm^{-1}. The addition of rGO to SWNT does not affect the quality of the SWNT dispersion as there is very little variation in bundle diameter across the various compositions of SWNT-rGO samples (Table 5.2).

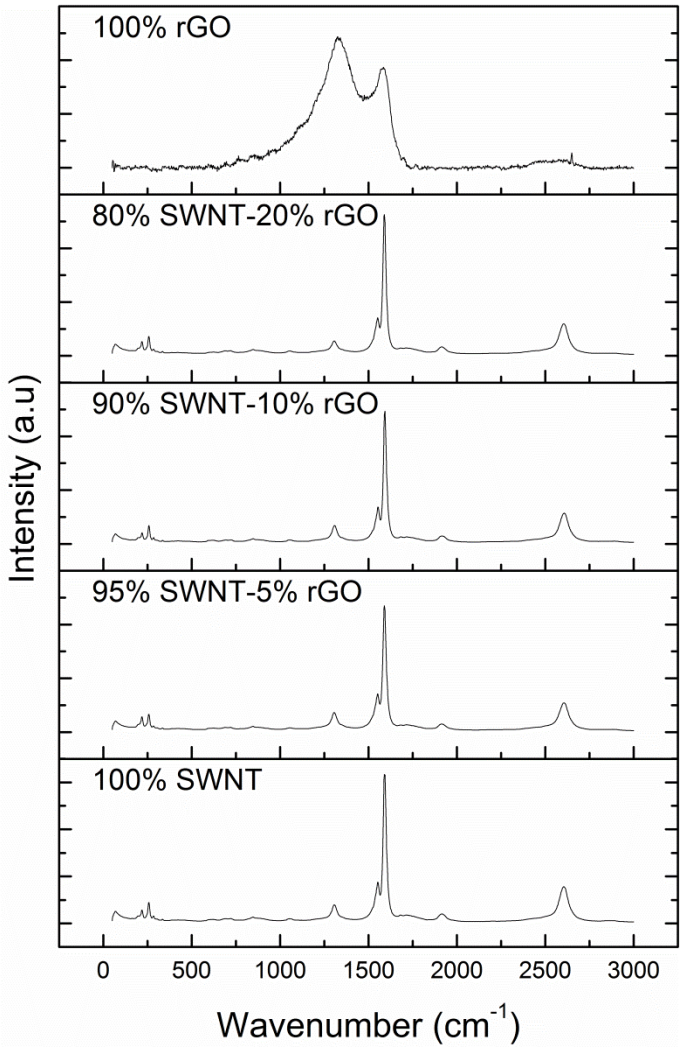

Figure 5.4 Raman spectra of the various carbon electrode compositions used.

Table 5.2 D-to-G band intensity ratios and SWNT bundle diameters (estimated using Equation 5.1) of the various carbon electrode compositions.

	I_D/I_G	SWNT bundle diameter (nm)		
100% rGO	1.316	1st peak	2nd peak	3rd peak
80% SWNT-20% rGO	0.155	1.14	0.96	0.873
90% SWNT-10% rGO	0.138	1.129	0.96	0.873
95% SWNT-5% rGO	0.126	1.14	0.96	0.879
100% SWNT	0.104	1.129	0.96	0.873

5.4.2.2 Morphology of various SWNT-rGO compositions

Work presented in Chapter 3, involving the synthesis of rGO electrodes via chemical reduction resulted in relatively flat sheets, clearly seen in the SEM image of the surface (Figure 5.5A). Sheets of this morphology have a tendency to restack during film fabrication via vacuum filtration of the dispersion (Figure 5.5B). This can be attributed to the van der Waals interactions between the rGO sheets [22]. For thermocell and other electrochemical applications, this is undesirable as it inhibits ion accessibility to the active areas of the carbon electrode.

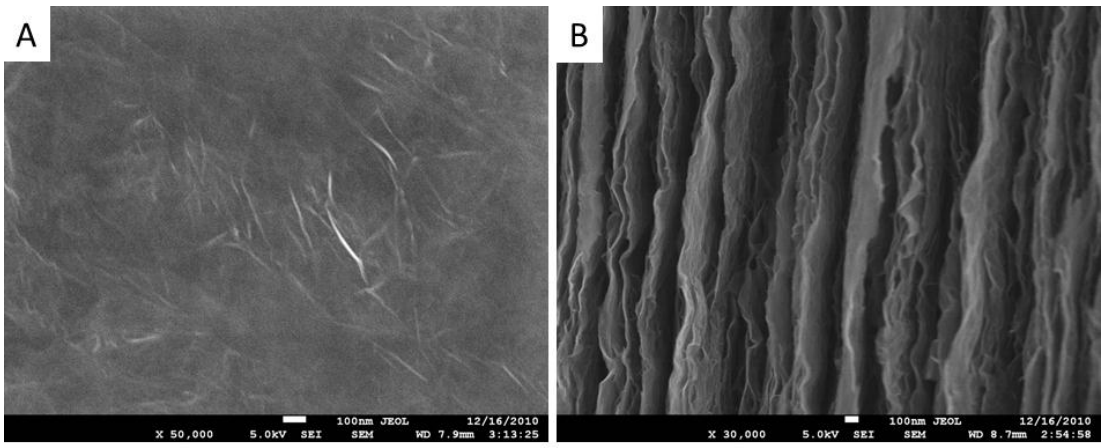

Figure 5.5 SEM images of A) surface, B) cross-section of chemically reduced graphene oxide

The micrographs of the rGO film (Figure 5.6A and B) indicate that it is composed of sheets that have a wrinkled surface. It is surmised that this morphology can minimise restacking of the rGO sheets which is the reason rGO was thermally reduced via microwave irradiation for this study. SEM images of the SWNT film (Figure 5.6C and D) display a uniform mat of CNTs. Micrographs of the SWNT-rGO

composite (Figure 5.6E and F) depict the interaction of the rGO sheets with the SWNTs wherein the latter is randomly attached to the surface of the former. This morphology may result in enhanced charge transfer as tube-sheet interactions have larger electron pathways as compared to tube-tube interactions. It must also be noted that larger pores are generated at SWNT-rGO interfaces; i.e. the composites are mesoporous. These larger pores are not present in the pure SWNT sample (Figure 5.6C and D).

The cross-section of the rGO electrode (Figure 5.7B) clearly shows the wrinkled nature of the sheets. The cross-section of the SWNT Figure 5.7A depicts a uniform mat of tubes. Looking at Figure 5.7B and C, it can be seen that interaction of SWNT and rGO produces a “layered” structure wherein gaps are generated between SWNT mats, presumably due to the presence of rGO sheets. These gaps may enhance electrolyte diffusion into the SWNT-rGO composite.

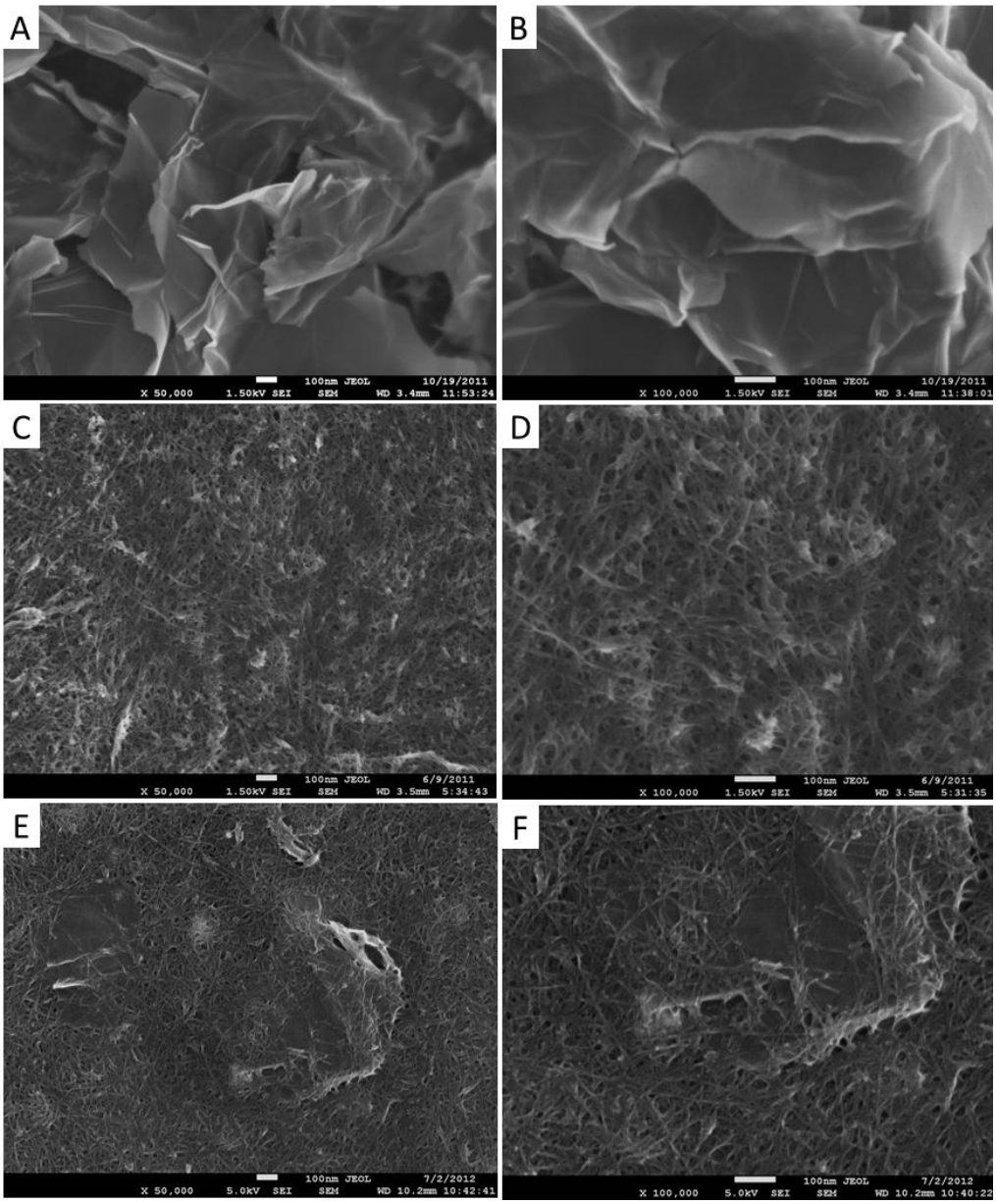

Figure 5.6 SEM images of the surface of A) and B) rGO, C) and D) SWNT, E) and F) SWNT-rGO composite

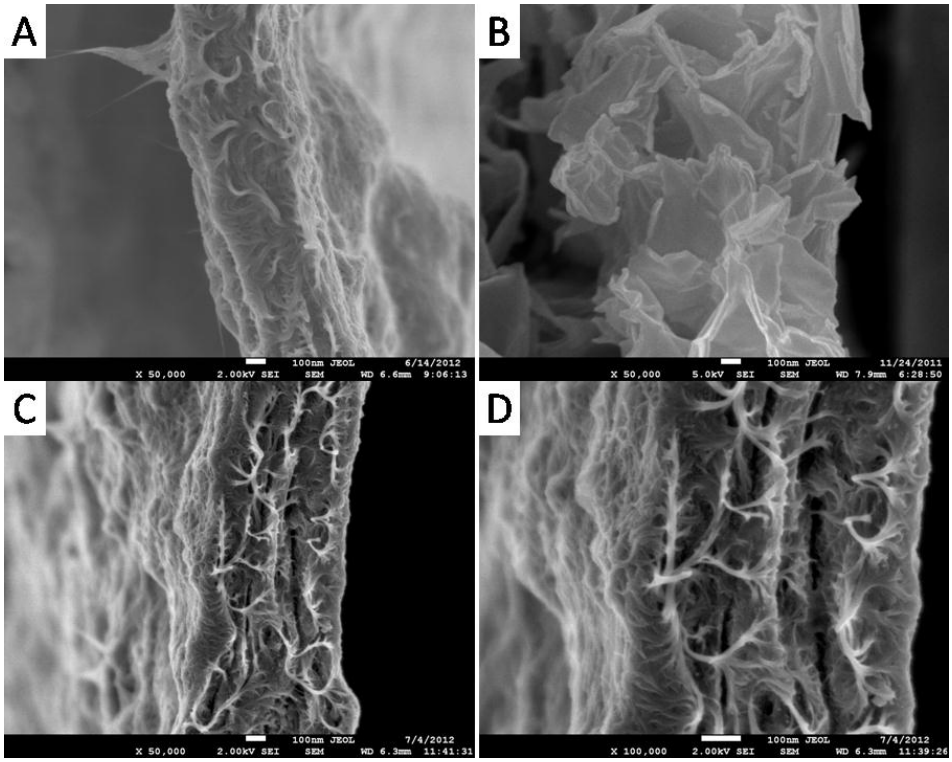

Figure 5.7 SEM images of the cross-section of A) SWNT, B) rGO, C and D) SWNT-rGO composite

5.4.2.3 Electrochemical impedance spectroscopy of various SWNT-rGO compositions

The diameter of the semicircle in the Nyquist plot for the SWNT electrode (Figure 5.8) is indicative of the charge transfer resistance (R_{ct}) [23]. From the EIS response of said sample, this value was estimated to be 73.98 Ω. This may be attributed to the tortuous nature of the SWNT film, wherein ions are not readily able to travel through the electrode. It is difficult to estimate R_{ct} for the SWNT-rGO composites as the EIS response is controlled by the mass transfer process; i.e. Warburg impedance is dominant [24]. The solution resistance (R_s) may be extrapolated from the Nyquist plot at high frequencies; i.e. obtain the intercept at the left side of the curve with the real part of impedance (x-axis) [25]. Based on this, the

SWNT film has an R_s of 38 Ω. The 95% SWNT-5% rGO and 80%SWNT-20% rGO films yielded R_s values of 36.8 Ω and 35.2 Ω respectively. The lowest R_s, 34.1 Ω was obtained from the 90% SWNT-10% rGO film. The rGO electrode has a slightly higher R_s, 44.2 Ω. This may be attributed to the defects in the rGO sample introduced during the sample synthesis; evidenced by the D-band in the Raman spectra (Figure 5.4). Defects act as scattering sites and decrease the ballistic transport path length, thereby decreasing the electronic performance of rGO [26, 27].

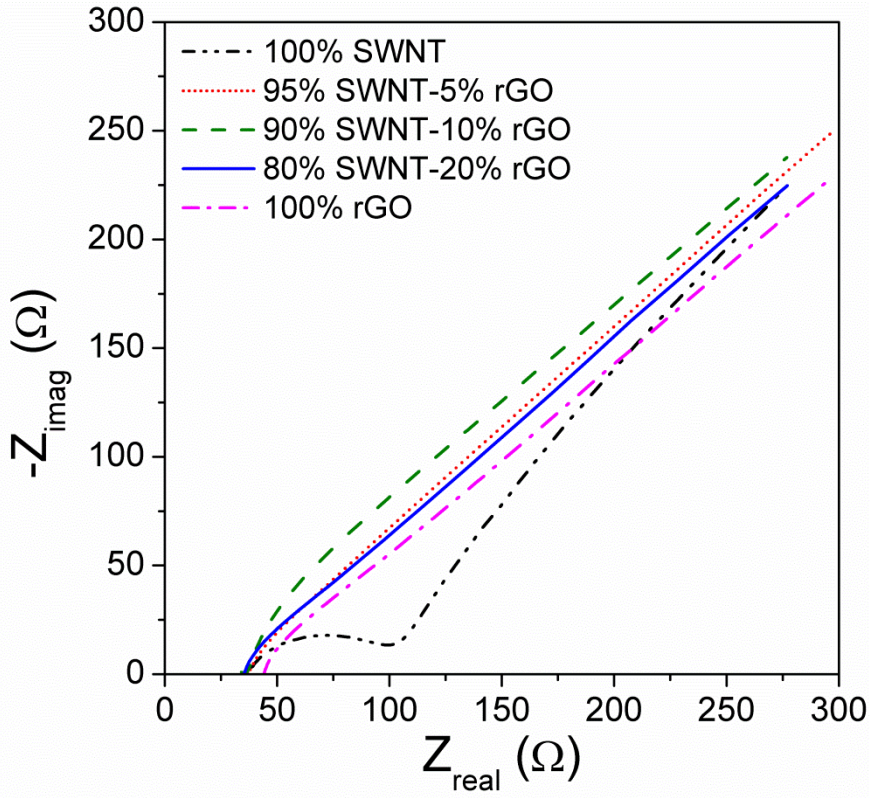

Figure 5.8 Nyquist plots obtained using electrodes of various SWNT-rGO ratios.

5.4.2.4 Cyclic voltammetry of various SWNT-rGO compositions

The main features in cyclic voltammograms (CVs) are the peak current and peak separations. The former gives insight to the electroactive surface area whereas the latter provides a measure of the heterogeneous reaction rate constant [28]. CVs run at 10 mV/s (Figure 5.9) clearly indicate an increase in faradaic peak current for the various carbon materials as compared to platinum. Also, the SWNT-rGO composites have larger faradaic peak currents compared to SWNT and rGO individually. Since all the electrodes used exhibit reversible kinetics, the increase in faradaic peak current can be attributed to a larger electroactive surface area (ESA) when the two different carbon materials are combined, as stated in Equation 5.2 [24].

$$I_{p-f} \; \alpha \; \sqrt{Dv} C_o A \qquad \text{Equation 5.2}$$

Where $I_{p\text{-}f}$ is the faradaic peak current, D the diffusion coefficient, v the rate at which the potential is swept (i.e. scan rate), C_o the initial electrolyte concentration, and A the ESA. The largest peak current was obtained when the 90% SWNT-10% rGO (this composite will be named 90-10 henceforth) was used. It must be noted that at the scan rate used (10 mV/s) the potential difference between the oxidation and reduction peaks for the various carbon materials are similar to that of platinum. This indicates that the carbon electrodes drive the electron transfer reaction at roughly the same rate as that of platinum.

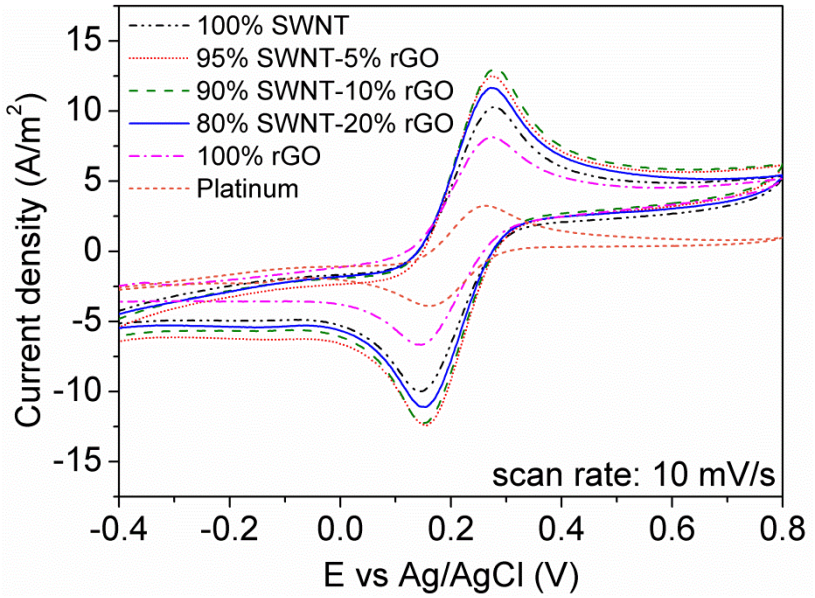

Figure 5.9 Cyclic voltammograms of various carbon electrodes compared with platinum (scan rate: 10 mV/s)

The ferricyanide/ferrocyanide redox couple may be used as a probe to measure the ESA of the various carbon electrodes [28]. By obtaining the faradaic peak currents of CVs run at different scan rates (Figure 5.10) and using the Randles-Sevcik equation (Equation 5.3), the ESA was determined.

$$I_{p-f} = 0.4463\, nFAC_o\sqrt{\frac{nFvD}{RT}} \qquad \text{Equation 5.3}$$

Where I_{p-f}, D, v, C_o, and A are as defined in the previous paragraph, n is the number of electrons, F is Faraday's constant, R is the universal gas constant, T is the temperature. It must be noted that the ESA values (Figure 5.11) may only be used to compare the performance of the various carbon electrodes and are not measurements of the actual area. This is because the Randles-Sevcik equation has been derived for

flat surfaces and does not take into account the porous nature of carbon electrodes. Nevertheless, the obtained values indicate that ESA is increased through the use of SWNT-rGO composites. More importantly the ESA is highest for the 90-10 electrode, which is in agreement with the qualitative comparison in the previous paragraph.

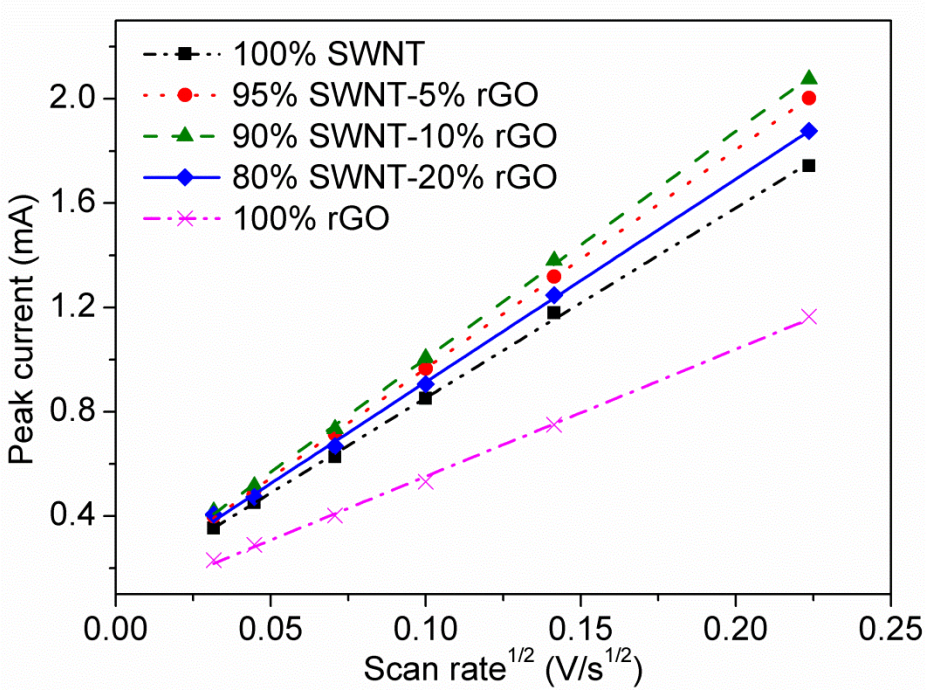

Figure 5.10 Peak current plotted against the square root of the scan rate for the various carbon materials used.

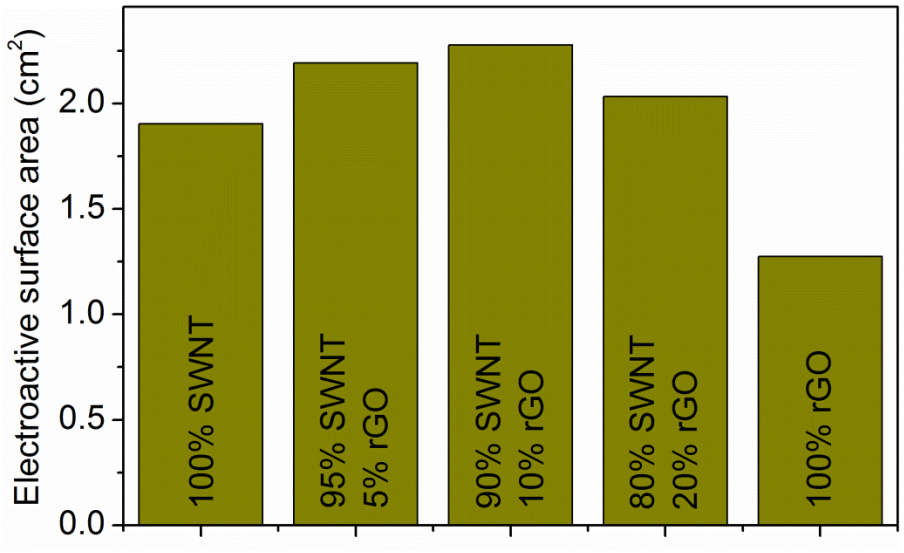

Figure 5.11 Electroactive surface area of the various carbon electrodes.

In cyclic voltammetry, for most systems, low scan rates facilitate electrochemical equilibrium at the electrode surface. When the scan rate is increased, the rate of electron transfer may become competitive with the potential sweep rate. Under these conditions, the potential difference between the oxidation and reduction peak may provide qualitative insight into the kinetics of the electron transfer process [29]. Sluggish electrode kinetics translates to greater potential or time to deplete all the ions at the electrode surface resulting in larger peak separations. Comparing the cyclic voltammograms taken at 200 mV/s (Figure 5.12) of the various carbon electrodes against that of platinum it can be seen that platinum has a smaller peak separation. This is expected as the carbon electrodes have a porous surface, as depicted in the micrographs (Figure 5.5), which increases the time required for diffusion of the electrolyte to and from the electroactive surface. Peak separation of the 90-10 (this composite was selected as it resulted in the largest peak currents) versus that that of SWNT and rGO indicates that the composite possesses the fastest electron transfer kinetics. It is surmised that this is brought about by a combination of

the enhanced ion accessibility and larger electron pathways in the 90-10 composite. These results are consistent with the electrode morphology (Figure 5.5 and Figure 5.6) and the EIS results. The Nyquist plot (Figure 5.8) indicates that charge transfer is slower in the SWNT electrode than the SWNT-rGO composite. Said plot also shows that the ohmic overpotential is higher for the rGO sample compared to the 90-10 which accounts for its slower kinetics.

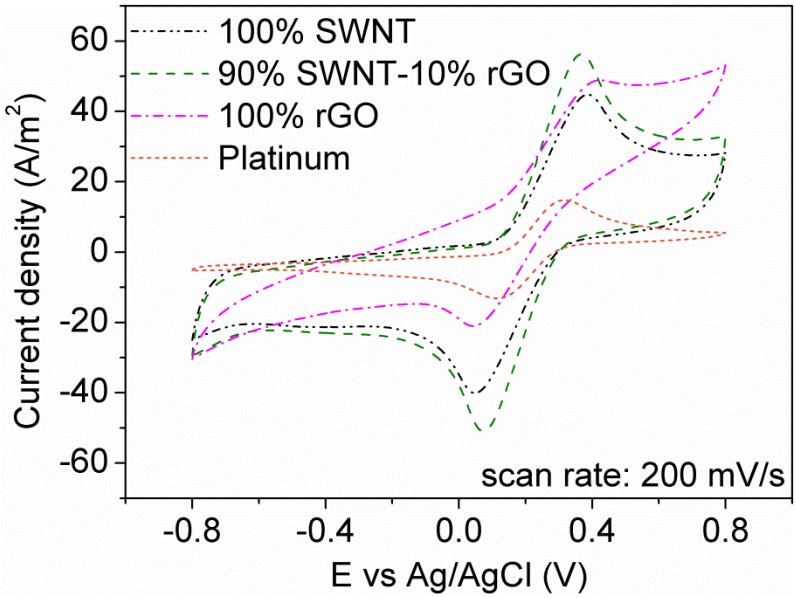

Figure 5.12 Cyclic voltammograms of various carbon electrodes compared with platinum (scan rate: 200 mV/s)

5.4.2.5 Thermocell testing of various SWNT-rGO compositions.

Current and power density was measured based on the size of a single electrode as the power conversion in a thermocell is limited by either the smaller or "slower" electrode; i.e. the electrode wherein the redox reaction is proceeding at a lesser rate. For systems that use the $K_3Fe(CN)_6/K_4Fe(CN)_6$ redox couple, the low temperature of the cathode contributes to sluggish diffusion and electron transfer

kinetics. For all the electrode materials used, the J-V curves (Figure 5.13) indicate an open circuit voltage (V_{oc}) around 43.5 mV. Using the Seebeck coefficient of 0.4 M $K_3Fe(CN)_6/K_4Fe(CN)_6$, which is 1.4 mV/K, the thermal gradient in the thermocell is roughly 31 K. The uniformity in V_{oc} across the various electrode materials is critical in order to ensure that meaningful data is obtained from the thermocell tests.

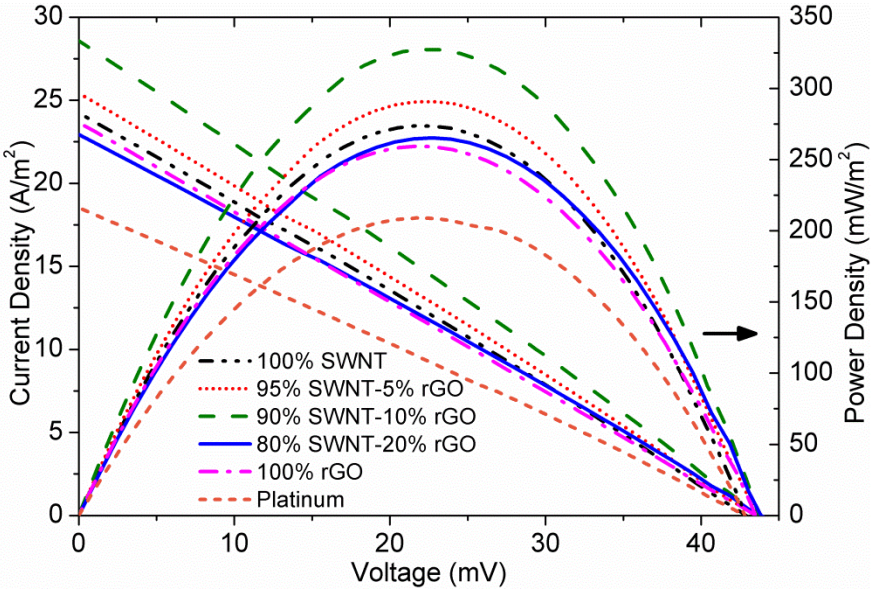

Figure 5.13 J-V curves generated using various electrode materials. Electrolyte: 0.4 M $K_3Fe(CN)_6/K_4Fe(CN)_6$

Thermal energy harvesting experiments (Figure 5.14) reveal that both SWNT and rGO are able to outperform platinum. Both carbon materials improved thermocell performance by roughly 30 %. This can be attributed to the larger electroactive surface area of the carbon materials as evidenced by their morphology and cyclic voltammograms. More importantly, by controlling the amounts of SWNT and rGO, this already improved performance may be further enhanced. The 90-10 composite outperformed the other composite materials along with its precursors,

generating 0.262 W/m^2. As mentioned previously, the 90-10 composite did not exhibit charge transfer overpotential (as opposed to SWNT) and had the lowest ohmic overpotential of all compositions tested. Also, it had the fastest kinetics and largest electroactive surface area as evidenced by its cyclic voltammograms (Figure 5.12 and Figure 5.9). The combined effects of these factors explain the improved performance of the 90-10 composite electrode. Although 10% rGO improved the performance relative to pure SWNT, it is surmised that excessive amounts of rGO (greater than 10 %) in the composite leads to a decrease in performance due to an increase in defect sites in the electrode material, lowering conductivity. Additionally, restacking of rGO sheets due to van der Waals interactions inhibits ion accessibility and reduces electroactive surface area [22].

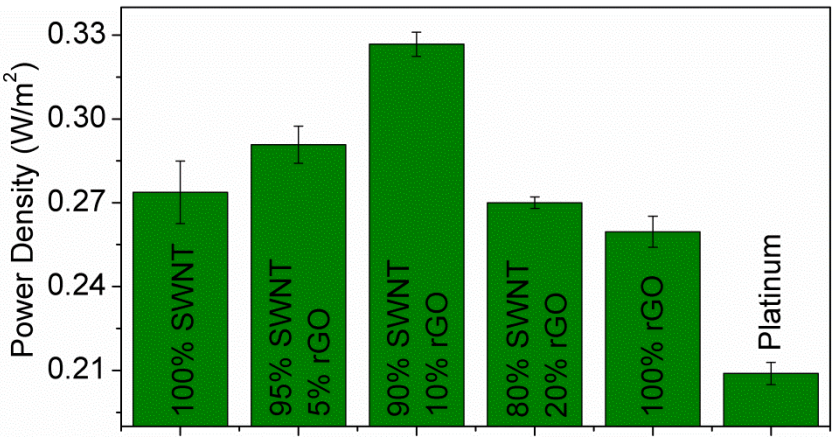

Figure 5.14 Power density attained through the use of various electrode materials. Electrolyte: 0.4 M $K_3Fe(CN)_6/K_4Fe(CN)_6$

As mentioned in Chapter 1, Section 1.2.3, the power conversion efficiency of thermogalvanic systems is given as [3]:

$$\Phi = \frac{0.25\, V_{oc} I_{sc}}{KA\left(\frac{\Delta T}{d}\right)}$$ Equation 5.4

Using Equation 5.4, the power conversion efficiency for the various electrodes (Figure 5.15) indicates that rGO has the lowest efficiency (3.06 x 10^{-2} %) of all the carbon materials. However it still outperforms platinum which has an efficiency of only 2.46 x 10^{-2} %. The SWNT-rGO composites outperformed their precursors, with the highest efficiency (3.85 x 10^{-2} %) attained using the 90-10 composite.

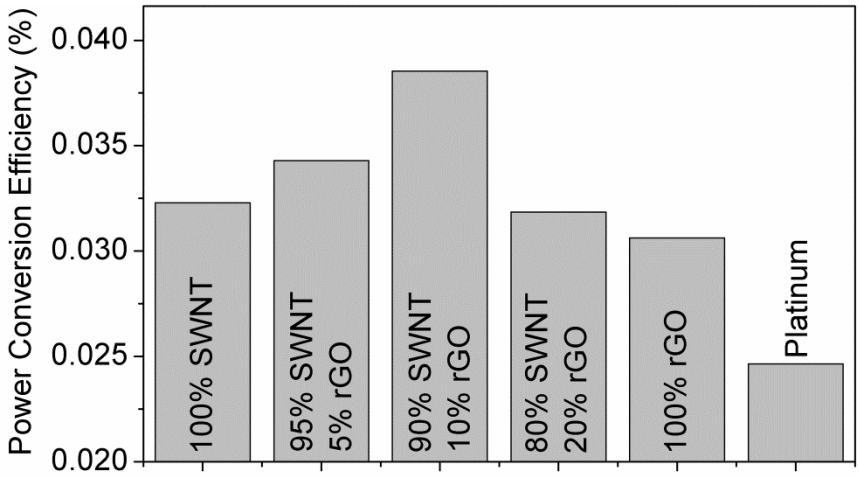

Figure 5.15 Power conversion efficiency attained through the use of various electrode materials. Electrolyte: 0.4 M $K_3Fe(CN)_6/K_4Fe(CN)_6$

5.4.3 Optimisation of electrode thickness

In order to improve thermocell performance it is desirable to further increase the exchange current density between the electrode and electrolyte; as this yields a larger net current density. An obvious approach to achieving this is to increase the

electrode thickness of the 90-10 composite. Therefore, films of 1.0, 1.5, 2.5, 4.5, 6.6 and 10.5 μm were prepared to facilitate an increase in electroactive sites.

5.4.3.1 Raman spectroscopy of 90-10 composite electrodes of various thicknesses

Raman spectra of the 90-10 films (Figure 5.16) prepared with increasing thicknesses have similar peak position and relative intensities. Values (Table 5.3) of the RBM depict SWNT bundle diameters of the same size and the I_D/I_G ratio is indicative of a similar amount of defects. These similarities are expected as the films have similar structures with only the thickness being changed.

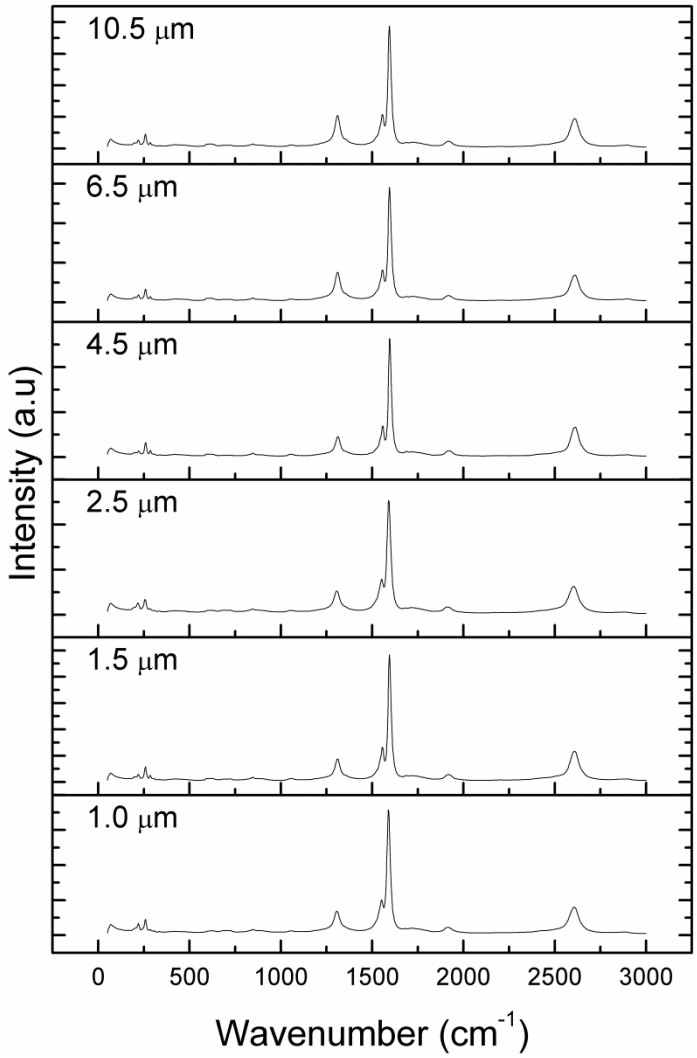

Figure 5.16 Raman spectra of the 90% SWNT - 10% rGO composite of difference thicknesses.

Table 5.3 D-to-G band intensity ratios and SWNT bundle diameters (estimated using Equation 5.1) of the 90% SWNT-10% rGO electrodes of various thicknesses.

Electrode thickness (μm)	I_D/I_G	SWNT bundle diameter (nm)		
		1st peak	2nd peak	3rd peak
1.0	0.138	1.140	0.960	0.873
1.5	0.138	1.139	0.960	0.873
2.5	0.139	1.140	0.961	0.874
4.5	0.138	1.139	0.960	0.873
6.5	0.138	1.139	0.960	0.873
10.5	0.138	1.139	0.960	0.873

5.4.3.2 Morphology of 90-10 composite electrodes of various thicknesses.

Micrographs of the surface (Figure 5.17) and cross-section (Figure 5.18) of the 90-10 composite of varying thicknesses depict similar morphologies wherein interaction of the SWNT and rGO sheets can clearly be seen. A clustering of tubes around dispersed rGO sheets prevents excessive restacking of the rGO. It can also be seen that the sheets are uniformly dispersed throughout the cross-section of even the thickest film.

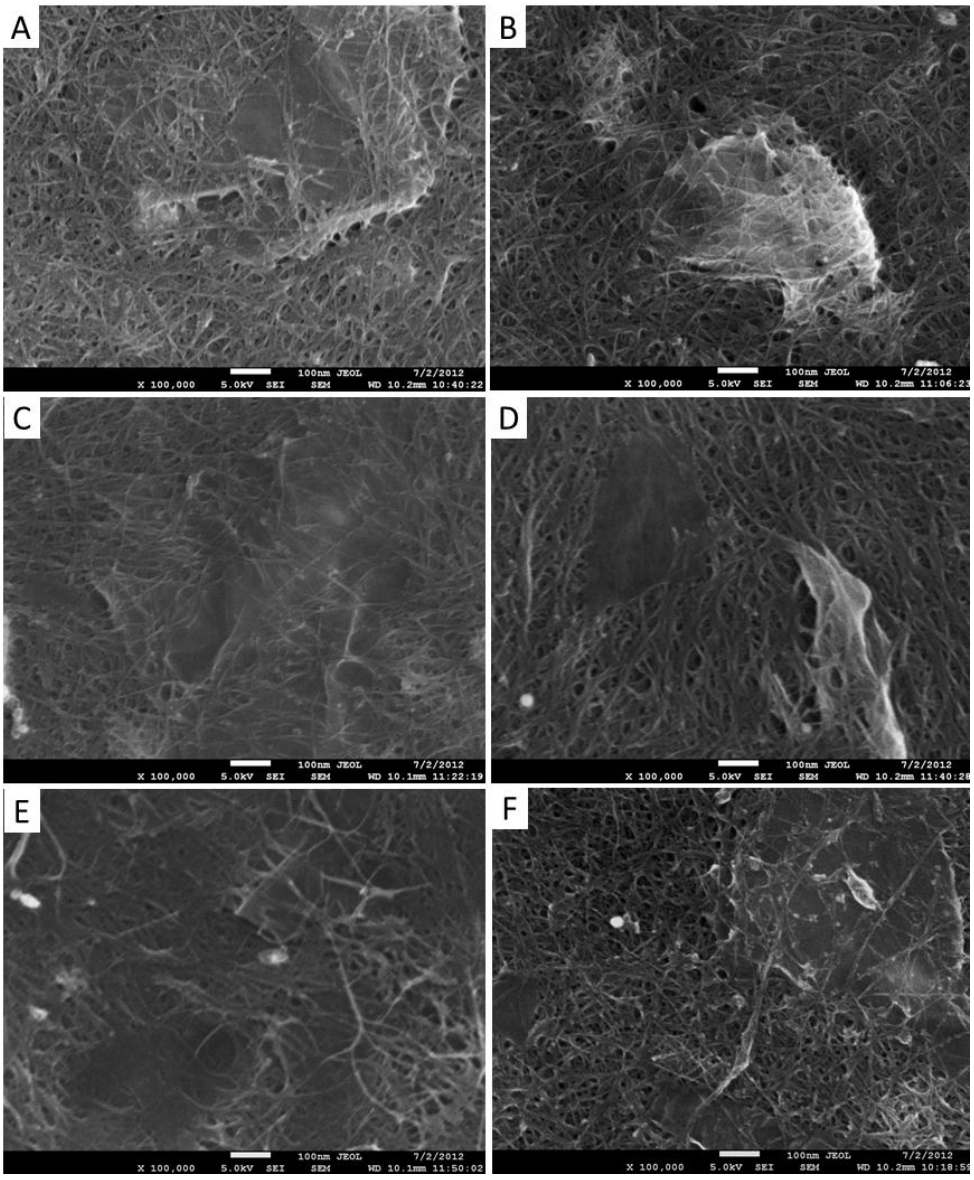

Figure 5.17 SEM images of the surface of A) 1.0, B) 1.5, C) 2.5, D) 4.5, E) 6.5, F) 10.5 μm thick films of 90% SWNT - 10% rGO composite

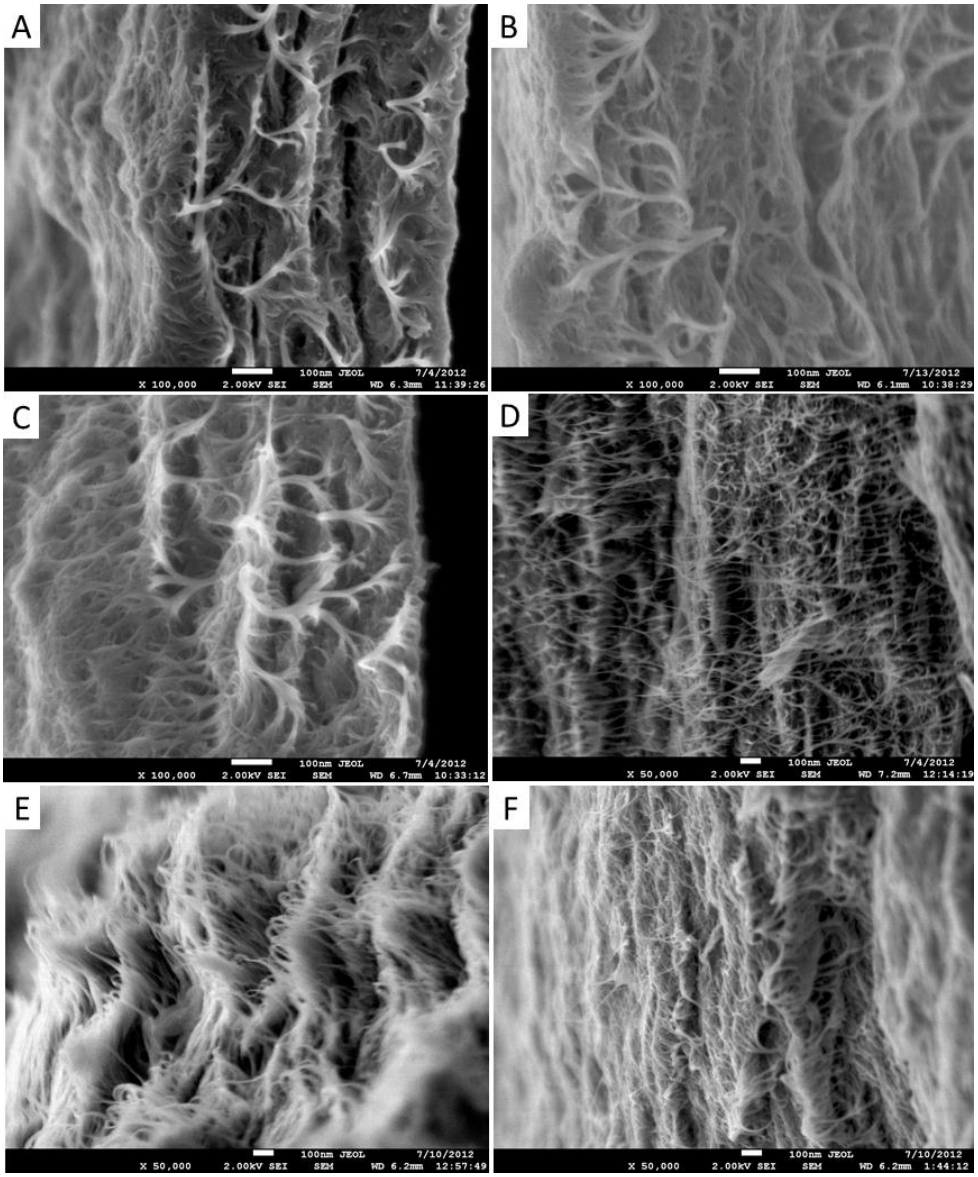

Figure 5.18 SEM images of the cross-section of A) 1.0, B) 1.5, C) 2.5, D) 4.5, E) 6.5, F) 10.5 μm thick films of 90% SWNT - 10% rGO composite

5.4.3.3 Electrochemical impedance spectroscopy of 90-10 composite electrodes of various thicknesses.

Nyquist plots generated using the 90-10 composite electrodes of varying thicknesses (Figure 5.19) indicate that as the film thickness is increased the semicircle increases in diameter. For thinner films (1.0 μm) the semicircle is

indistinguishable. This implies that R_{ct} is negligible and that the kinetics of the EIS response is limited by mass transfer [24]. The semicircle can clearly be seen for the 4.5 and 10.5 μm films, with R_{ct} of 27.5 and 34.8 Ω respectively. For these films the EIS response is limited by a mix of mass transfer and charge transfer [24]. The degree of tortuosity of the films is directly proportional to its thickness owing to the random nature of the pores. It is surmised that this increased tortuosity restricts ion accessibility, resulting in increased R_{ct}.

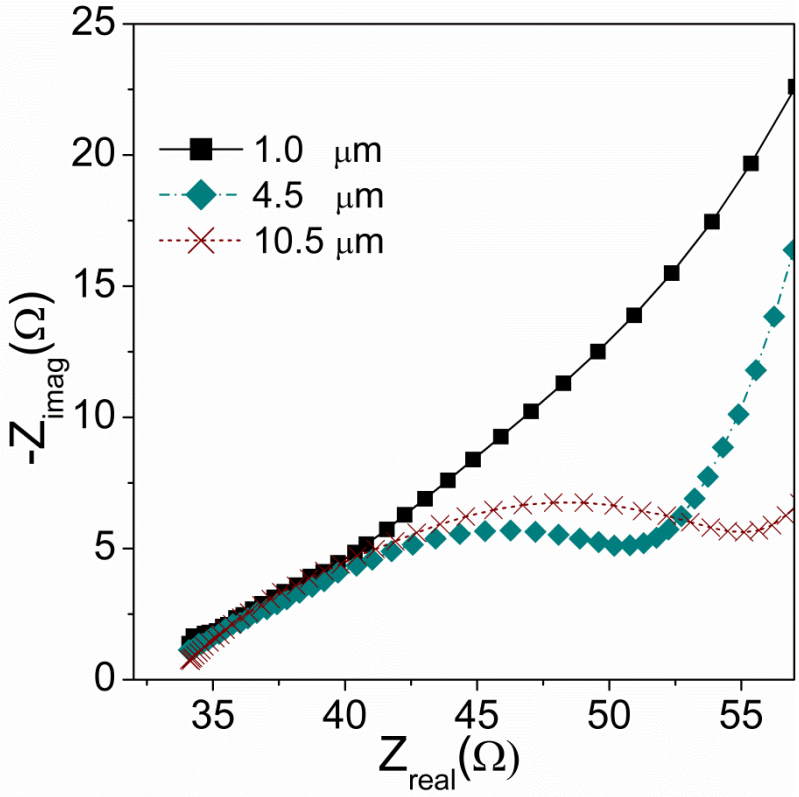

Figure 5.19 Nyquist plots generated using 90% SWNT-10% rGO composite electrodes of varying thicknesses.

5.4.3.4 Cyclic Voltammetry of 90-10 composite electrodes of various thicknesses

The faradaic peak currents in the CVs of the 90-10 composite (Figure 5.20) increase initially with thickness but plateau at the 4.5 μm film. As mentioned earlier, the faradaic peak current can be used to estimate the electroactive surface area using Equation 5.2 [24]. The fact that the electroactive surface area tapers off at the 4.5 μm film implies that ion accessibility is limited for thicker films by the tortuosity of the electrode structure.

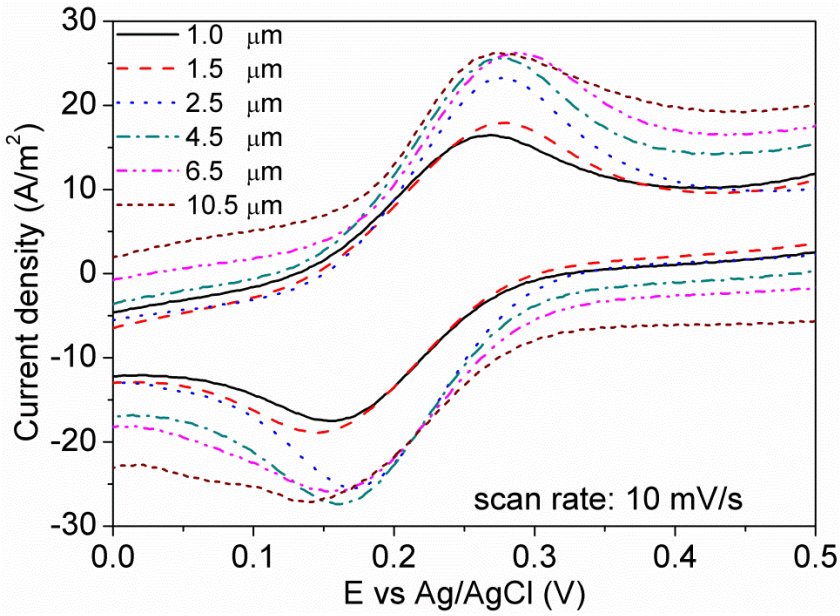

Figure 5.20 Cyclic voltammograms generated using 90% SWNT-10% rGO electrodes of varying thicknesses.

5.4.3.5 Thermocell testing of 90-10 composite electrodes of various thicknesses

Thermocell testing (Figure 5.21) indicates that power density initially scaled with thickness, then plateaued at around 0.46 W/m^2 for the 4.5 μm thick film. This

behaviour correlates well with the EIS measurements (increased R_{ct} for thicker films) and CV results (electroactive area is maximum at the 4.5 μm thick film).

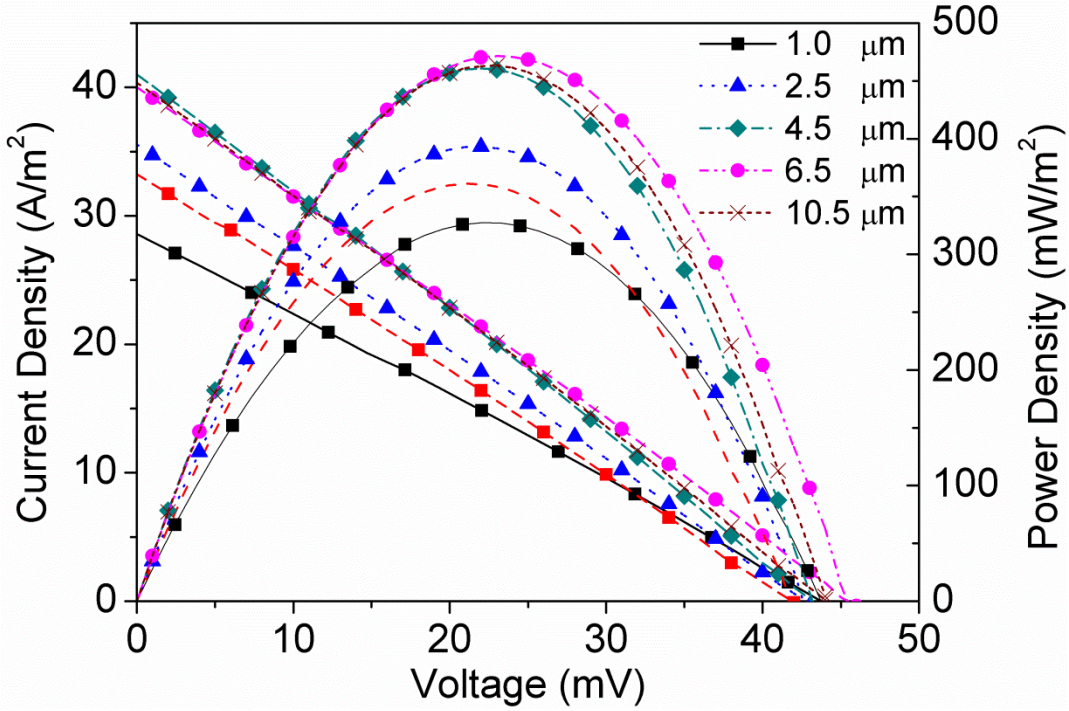

Figure 5.21 J-V curves generated using 90% SWNT-10% rGO electrodes of varying thicknesses. Electrolyte: 0.4 M $K_3Fe(CN)_6/K_4Fe(CN)_6$

The film density (Figure 5.22) displayed the same trend as power density. Said behaviour may provide insight as to how the film porosity changed with increasing thickness; i.e. the balance between porosity and film thickness was attained at the 4.5 μm film. For continuous power output in thermocells, reactants at the cathode need to be replenished by the reaction products formed at the anode and vice versa. Electrodes must be structured so as to facilitate this diffusion process and thus minimise the mass transport resistance [7]. As film thickness was increased, the random orientations of the pores led to increased tortuosity of the film thus exacerbating the problems associated with reactant/product diffusion, especially through the electrode; i.e. thicker materials have longer diffusion paths. Films thicker

than 4.5 μm only led to a waste of material as not all sites could be accessed by the electrolyte; thus did not participate in the redox processes required for thermal harvesting.

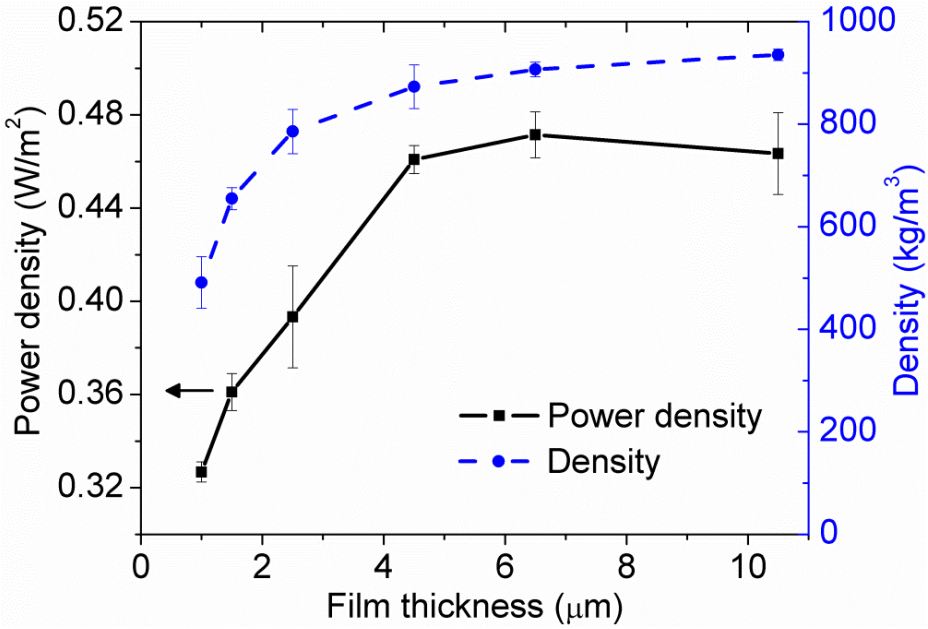

Figure 5.22 Power density and film density of 90% SWNT-10% rGO electrodes of varying thicknesses.

Extended tests of the 4.5 μm film (Figure S9) indicated a stable power output over a period of 48 hours. Furthermore, the power output remained stable despite repeated cycles wherein the thermal gradient was applied and removed. These findings indicate that diffusion and convection occurs in the thermocell and prevents excessive build-up of reaction products at the electrodes [2].

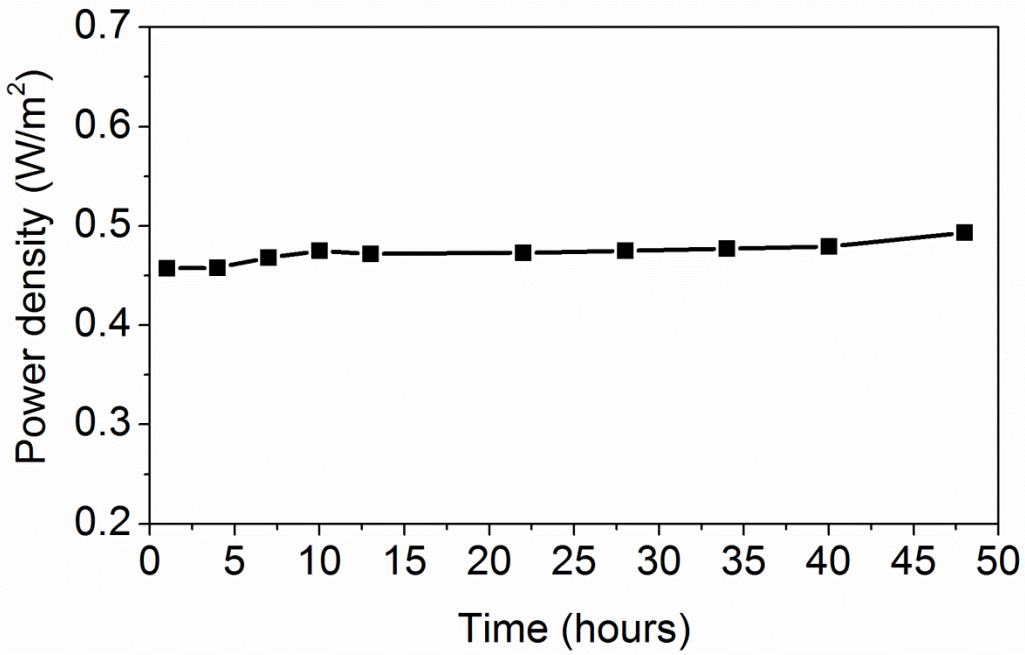

Figure 5.23 Power density obtained using the 4.5 μm thick 90% SWNT – 10% rGO electrodes over extended periods. Electrolyte: 0.4 M $K_3Fe(CN)_6/K_4Fe(CN)_6$

Comparison of the power conversion efficiency (calculated using Equation 5.4) of the films of various thicknesses (Figure 5.24) indicated that the maximum value of 5.44 x 10^{-2} % was attained at the 4.5 μm thick film. This is an improvement of around 41 % as compared to the 1 μm thick film, and 121 % relative to platinum. The thickest film (10.5 μm) had a power conversion efficiency of 5.47 x 10^{-2} %. Taking errors into account, this value is the same as that of the 4.5 μm film.

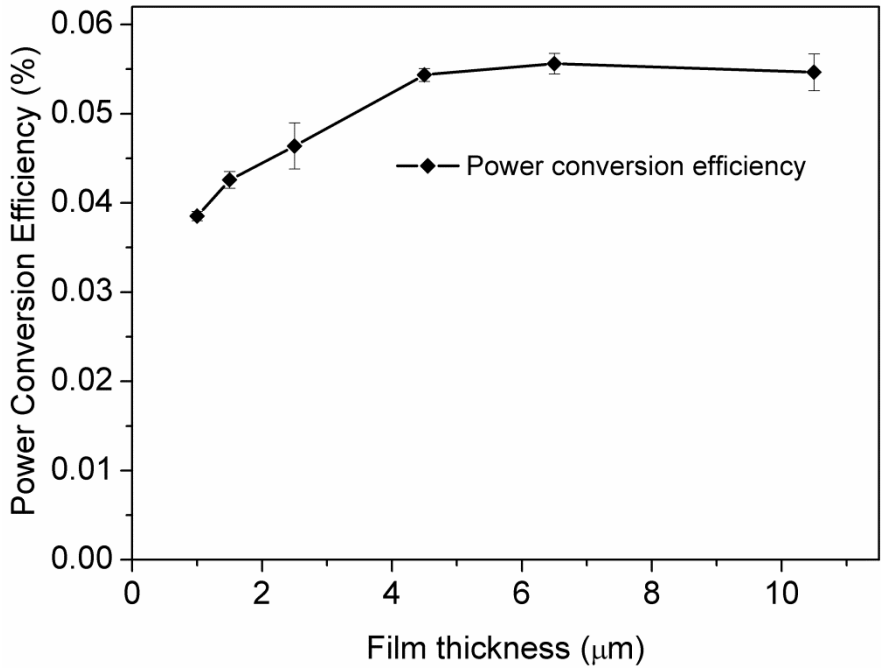

Figure 5.24 Power conversion efficiency of 90% SWNT-10% rGO films of varying thicknesses.

Using the efficiency attained through the use of the 4.5 μm thick film ($5.44x10^{-2}$ %), the efficiency relative to a Carnot engine is 0.65 %. This relative efficiency is seven times the value (0.09 %) reported in previous thermocell work involving platinum electrodes [3].

Despite the fact that power conversion efficiency is computed based on the area of the electrode (areal power density) it is still important to compare mass power density attained. The decreasing trend in mass power density (based on the mass of both electrodes) with electrode thickness (Figure 5.25) was expected as not all of the material would be accessible by the electrolyte, especially for the thicker films due to their increased tortuosity. The lowest mass power density (23.59 W/kg) was obtained through the use of the 10.5 μm film. The 4.5 μm film, which had the maximum power conversion efficiency, had a mass power density of 58.64 W/kg. This implies

that through the use of less than half of the carbon material, the power conversion efficiency is maximised. This translates to a lower price per watt and is critical in order to achieve the goal of commercial viability for thermogalvanic systems.

As mentioned earlier, platinum has a power conversion efficiency of only 2.46×10^{-2} %. The mass power density attained through using said material is only 0.14 W/kg. Using this value and the current price of platinum [30], said material has a price per watt that is ~146 times greater than that of the optimised composite electrode (4.5 μm thick 90% SWNT – 10% rGO). The developed optimised composite electrode has a price per watt that is around 22 times lower than that previously reported by Kang et. al. involving CNT-rGO composites [7]. It must be noted that said work was carried out without any attempt to optimize the electrode material and was focused on understanding the fundamentals of thermocells using nano-carbon electrodes.

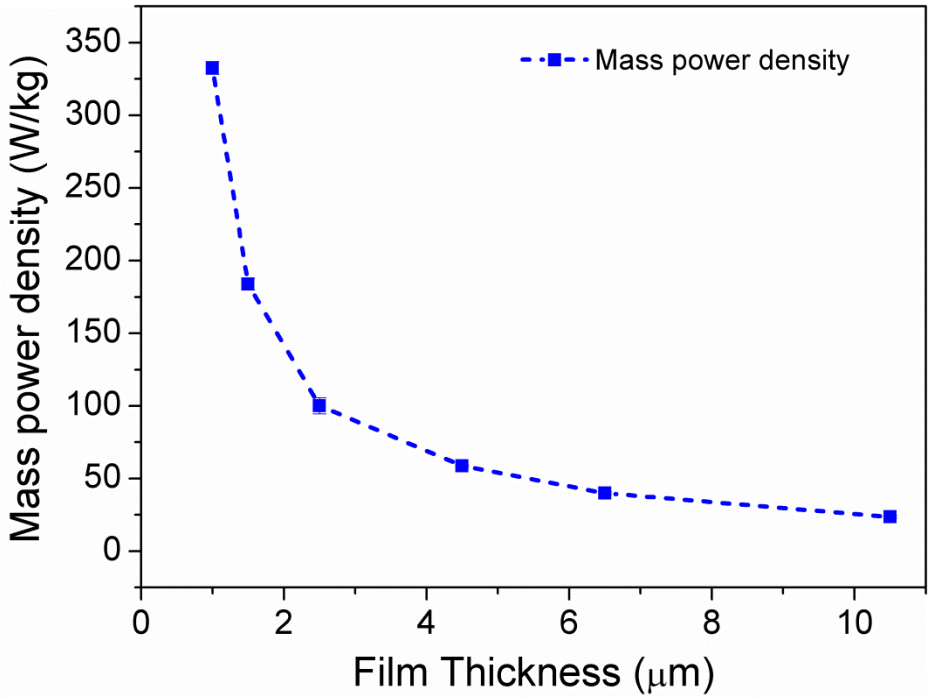

Figure 5.25 Mass power density of 90% SWNT-10% rGO films of varying thicknesses.

5.4.4 Stacked electrode configuration

In order to further enhance thermocell power output, the electrodes should be structured such that ions may freely diffuse while maintaining a high surface area and good electrical conductivity. Such a structure may be attained by using a stacked electrode configuration, which consists of alternating layers of the optimized SWNT-rGO film and stainless steel mesh (Figure 5.26). The stainless steel mesh acts as a separator between the SWNT-rGO films, allowing the electrolyte to interact with the high surface area of the nano-carbons while facilitating ionic diffusion. It also maintains a conductive path for electrons between the individual films.

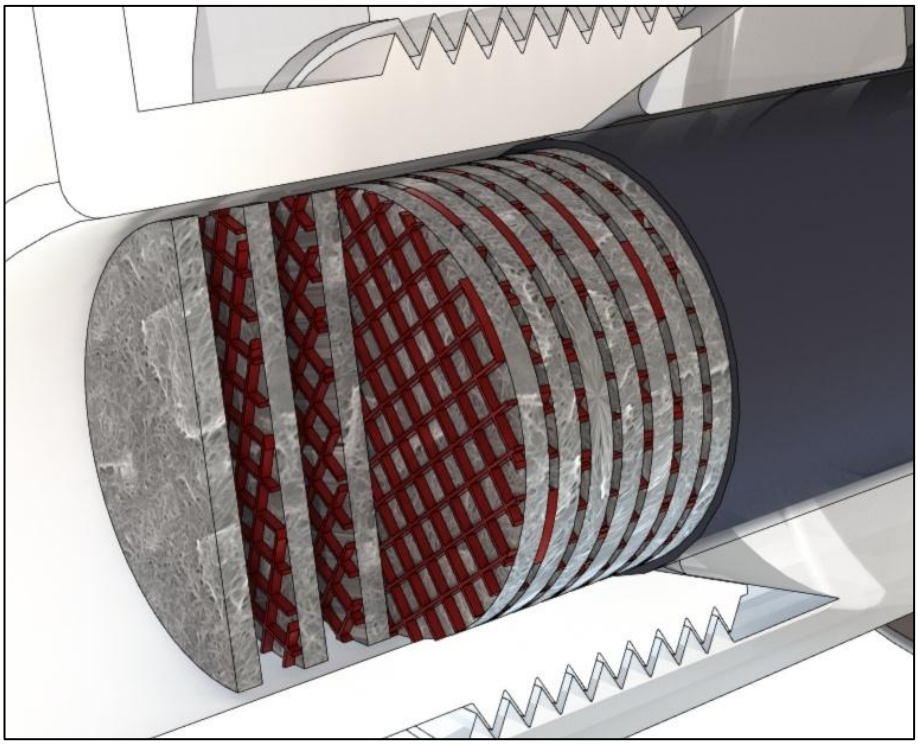

Figure 5.26 Schematic of the stacked electrode configuration. Stainless steel mesh is coloured red to differentiate from the SWNT-rGO film.

Thermocell testing involving 5 optimized SWNT-rGO films per half-cell yielded an areal power density of 1.29 W/m^2 (Figure 5.27); equivalent to an efficiency relative to a Carnot engine (Φ_r) of 1.83 % (Figure 5.28). Further improvement was realized when 10 optimized SWNT-rGO films per side were stacked (10 stack configuration), generating 1.85 W/m^2 (Figure 5.27). This areal power density is a four-fold increase over that of a single electrode (non-stacked) configuration (0.46 W/m^2, Figure 5.22). Previous work using SWNT-rGO composite electrodes yielded a normalised areal power density ($P_{area}/\Delta T^2$) of 0.4 mW/m^2-K^2 and normalised mass power density ($P_{mass}/\Delta T^2$) of 13 mW/kg-K^2 [7]. Through the use of the 10 stack configuration, improvements of ~380 % and ~280 % in $P_{area}/\Delta T^2$ (1.9 mW/m^2-K^2) and $P_{mass}/\Delta T^2$ (49 mW/kg-K^2) respectively were attained. These results

demonstrate enhanced thermocell performance using significantly less active material. These developments imply a lower price per Watt, thus making thermocells more cost effective to produce. More importantly, the combination of the optimized electrode composition, thickness, and the new stacked electrode configuration resulted in efficiency of 2.63 % relative to a Carnot engine (Figure 5.28). This Φ_r is a remarkable 88 % improvement compared to the highest reported Φ_r in thermocells (1.4 %) and within the range for commercial viability of these devices as predicted by Quickenden et al. (i.e. Φ_r between 2 to 5 %) [3, 8]. However, further developments in nano-carbon synthesis are still necessary to decrease the price of SWNT and rGO in order to achieve commercialisation of thermocells.

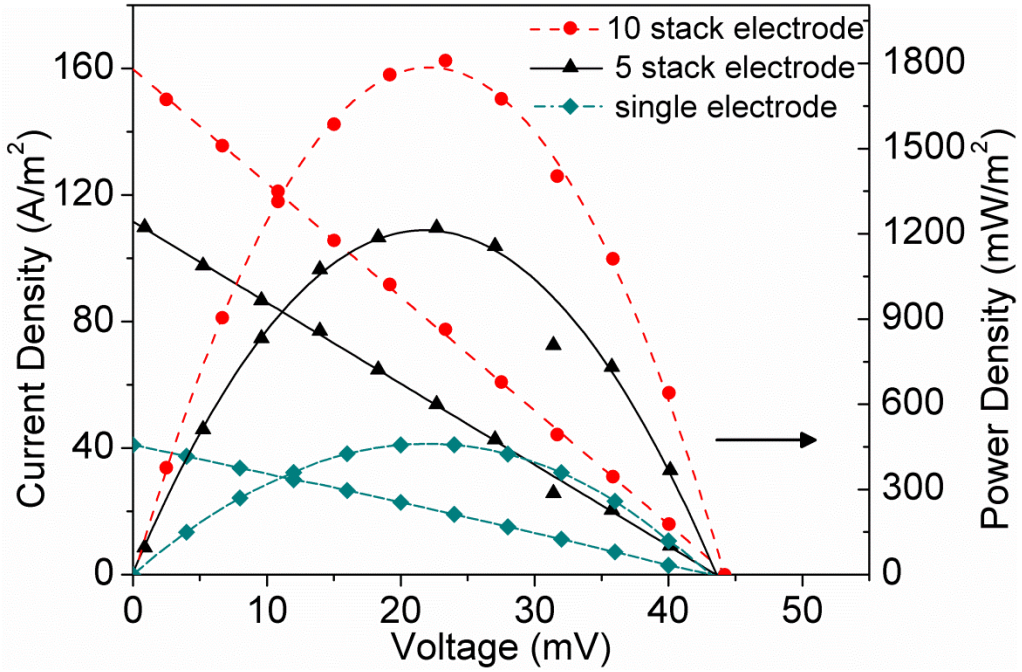

Figure 5.27 J-V curves generated using various electrode configurations. Electrolyte: 0.4 M $K_3Fe(CN)_6/K_4Fe(CN)_6$

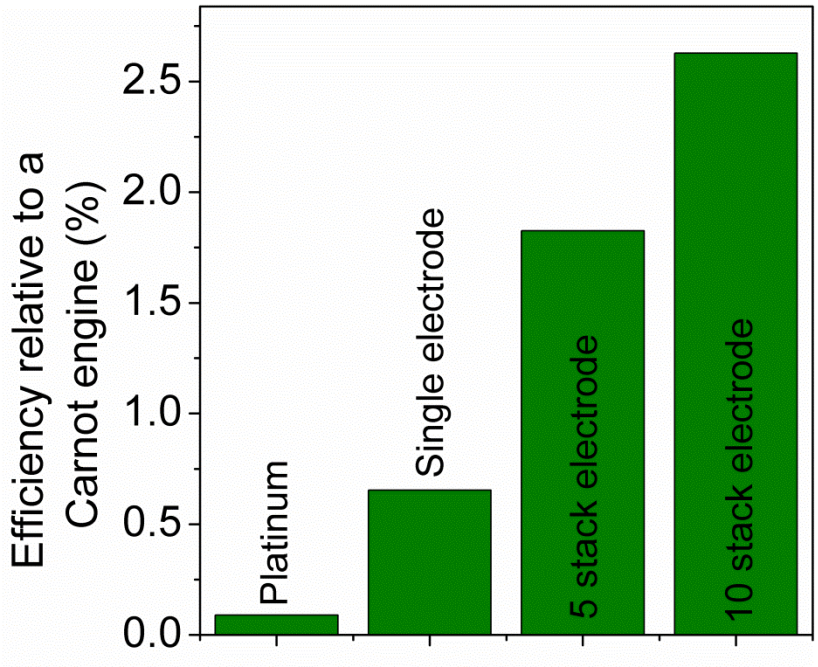

Figure 5.28 Relative power conversion efficiency attained using platinum [3], the optimised SWNT-rGO film in single, 5, and 10 stacked electrode configurations.

5.4.5 Vascular electrode structures

Improvement in thermocell performance may be realised through the use of electrode materials that have vascular structures, owing to their larger ESA. Carbon cloth possesses said structure aside from other properties (low electrical resistance, light weight, high porosity, chemical and thermal stability, good mechanical strength, and high degree of flexibility) which make it desirable for thermal harvesting applications [10, 11]. A further increase in ESA may be attained with proper integration of the 90-10 composite with carbon cloth.

5.4.5.1 Electrode morphology of carbon cloth based electrodes

The morphology of the different electrodes tested can be seen in Figure 5.29 and Figure 5.30. SEM images of the carbon cloth (Figure 5.29 A and Figure 5.30 A)

reveal a plain fibre whereas samples with the 90-10 composite show the integration of nano-carbons at varying degrees of uniformity. Filtration of the 90-10 dispersion through the carbon cloth produced a non-uniform structure with only certain parts of the fibres covered by the 90-10 composite (Figure 5.29 B and Figure 5.30 B). It must be noted that filtration may have led to the nano-carbons being deposited on the interior of the carbon cloth; i.e. the 90-10 composite dispersion was sucked into the carbon cloth by the vacuum. SEM images (Figure 5.29 C, D, E and Figure 5.30 C, D, E) reveal that a greater degree of uniformity of the 90-10 composite coating on the carbon cloth was obtained via dip coating. A comparison of the single-layer with the 5-layers dip coated sample reveals a higher density of the nano-carbons deposited on the latter; i.e. increasing the number of layers resulted in a greater degree of coverage of the 90-10 composite on the carbon cloth. The 10-layers dip coated sample had a morphology that was not as porous as the other samples. This structure was likely the result of excessive deposition of the 90-10 composite via dip coating and could lead to diminished electrochemical performance.

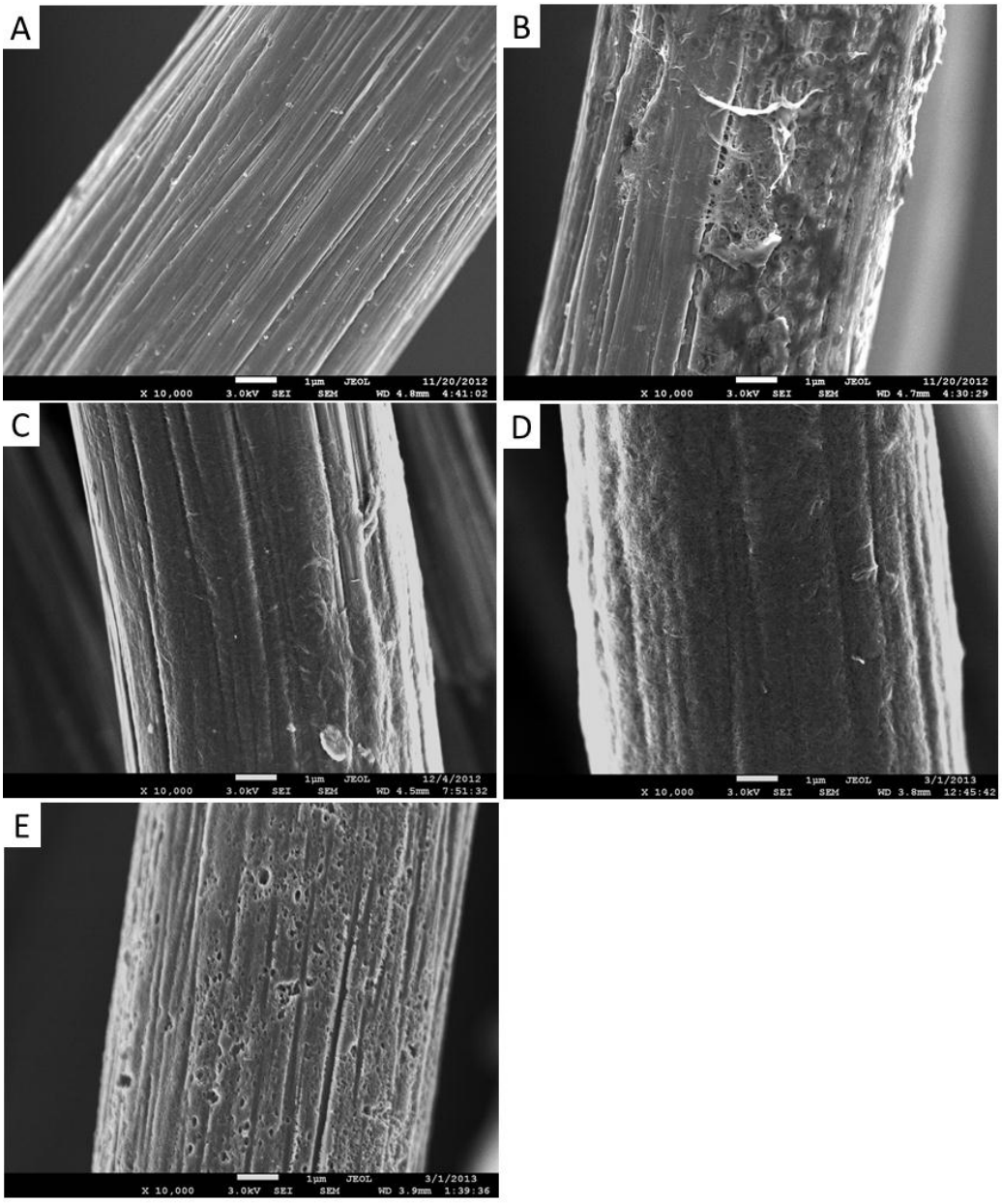

Figure 5.29 SEM images at 10000 X of the A) carbon cloth, 90 % SWNT-10 % rGO deposited on the carbon cloth by B) filtration, C) dip coating 1X, D) dip coating 5X, E) dip coating 10X.

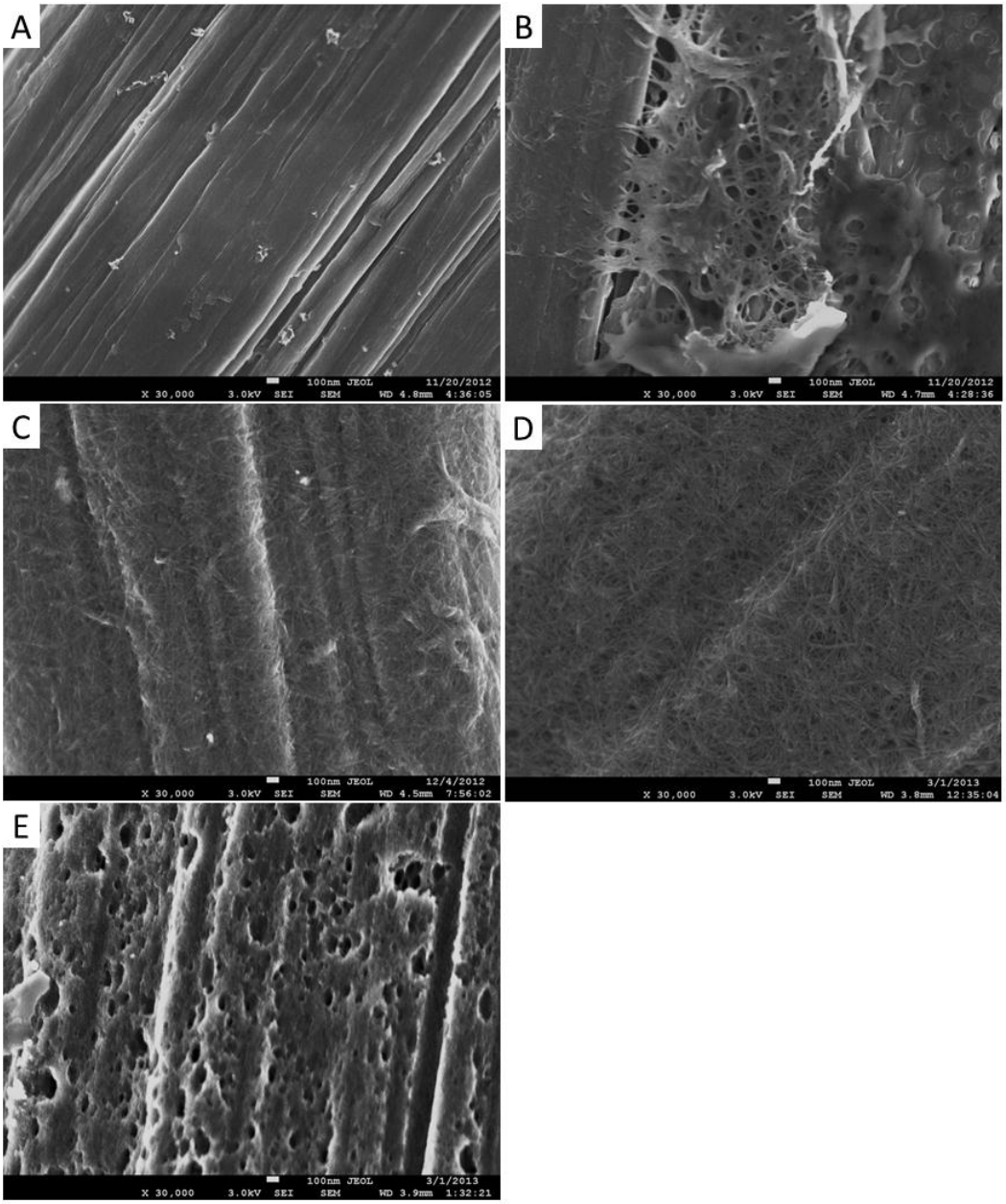

Figure 5.30 SEM images at 30000 X of the A) carbon cloth, 90 % SWNT-10 % rGO deposited on the carbon cloth by B) filtration, C) dip coating 1X, D) dip coating 5X, E) dip coating 10X.

5.4.5.2 Raman spectroscopy of carbon cloth based electrodes

As mentioned previously, the regions of note in the Raman spectra of carbon materials are the D (~1350 cm^{-1}) and G (~1600 cm^{-1}) peaks [16, 31, 32]. The ratio of

the D-to-G band intensity (I_D/I_G) may provide qualitative insight to the amount of defects present in carbon materials [17, 18, 31]. The Raman spectrum (Figure 5.31) of the carbon cloth reveals a structure that has structural imperfections (I_D/I_G = 1.473, Table 5.4). The 90-10 composite was predominantly composed of SWNT with minimal defects present, which is reflected in its low I_D/I_G of 0.138. The sample wherein the 90-10 composite was filtered through the carbon cloth yielded a Raman spectrum similar to that of pristine carbon cloth (I_D/I_G = 1.537). This may be caused by the uneven coverage of the carbon cloth by the 90-10 composite when this deposition method was employed; as shown in the SEM images (Figure 5.29 B and Figure 5.30 B). The Raman spectra of the dip coated samples are similar to that of the 90-10 composite. This is in good agreement with the morphology of said samples (Figure 5.29 and Figure 5.30) wherein a more uniform coating was obtained by dip coating. The I_D/I_G for the dip coated samples decreased as the number of layers of the composite was increased; i.e. 0.481, 0.267, and 0.155 for 1, 5 and 10 layers respectively. This could be indicative of a greater degree of coverage/coating of the 90-10 composite on the carbon cloth.

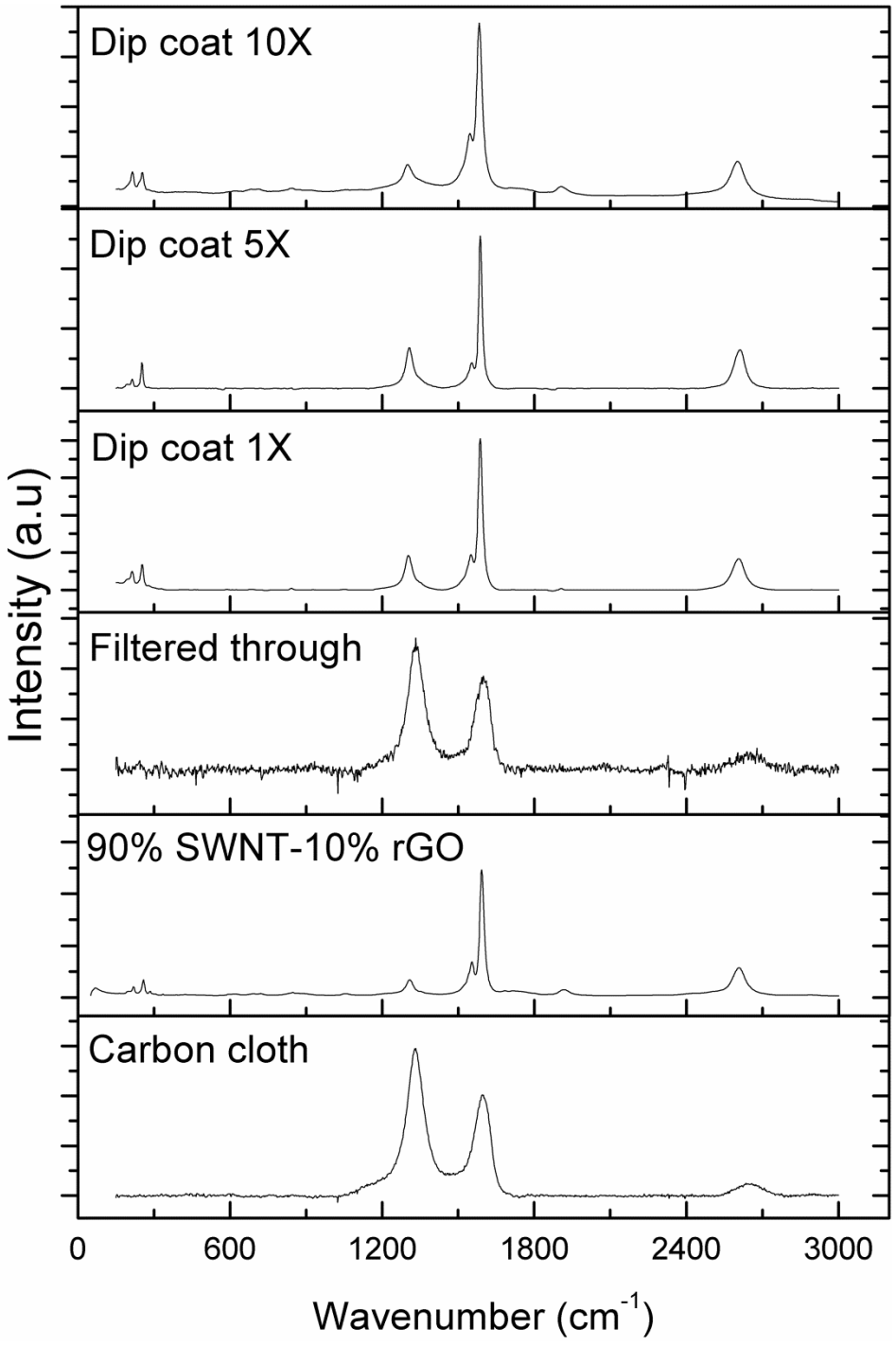

Figure 5.31 Raman spectra of the various vascular structured carbon electrodes.

Table 5.4 D-to-G intensity ratios of the various carbon electrodes developed.

	I_D/I_G
Carbon cloth	1.473
90% SWNT-10% rGO	0.138
Filtered through	1.537
Dip coat 1X	0.481
Dip coat 5X	0.267
Dip coat 10X	0.155

5.4.5.3 Cyclic voltammetry of carbon cloth based electrodes

CVs run at 10 mV/s of the various electrode materials investigated (Figure 5.32) indicate an increase in faradaic peak current as the 90-10 was incorporated into the carbon cloth. This rise in faradaic peak current may be attributed to an increase in electroactive surface area (ESA) when the nano-carbons were deposited on the carbon cloth, as stated in Equation 5.2. The sample wherein the 90-10 was filtered through has higher faradaic peak currents than the dip coated sample with 1 layer despite the fact that SEM images (Figure 5.29 and Figure 5.30) reveal a more uniform coating on the dip coated samples. As mentioned previously, this could be caused by the 90-10 composite being deposited on the inside of the carbon cloth when filtration was used, thus resulting in a higher ESA. The 5-layers dip coated sample afforded the highest faradaic peak current, which is in good agreement with the morphology of the various electrodes. The higher density of the 90-10 composite on the surface of the carbon cloth for said sample yielded an increased ESA. The 10-layers dip coated electrode had a lower ESA compared to the 5-layers dip coated

sample, which could have been caused by blocking of the pores of the carbon cloth, as shown in the SEM images.

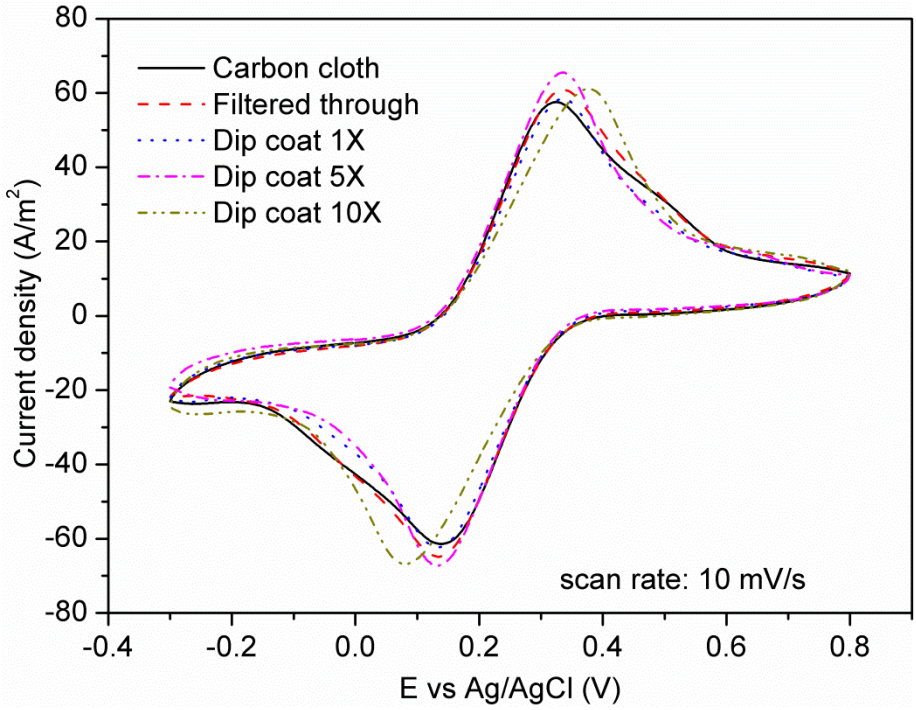

Figure 5.32 Cyclic voltammograms at a scan rate of 10 mV/s of the various vascular structured carbon electrodes investigated.

CVs obtained at low scan rates simulate conditions akin to electrochemical equilibrium at the electrode surface. Qualitative analysis on the rate of electron transfer of various electrode materials may be done by comparing the redox peak separation when the potential sweep rate is increased [18]. At fast scan rates, the rate of electron transfer may compete with the rate at which the potential is being swept. Slow electrode kinetics is characterised by a large separation between redox peaks in CVs [24]. CVs taken at 100 mV/s (Figure 5.33) reveal that the smallest peak separation was attained by the pristine carbon cloth. Incorporation of the 90-10 composite with the carbon cloth resulted in an increase in redox peak separation,

which implies a diminished rate of electron transfer. As mentioned previously, the tortuosity of the 90-10 composite (due to the random pore orientation) impedes ion diffusion. The slower electrode kinetics of samples coated with the nano-carbons may be attributed to the fact that the 90-10 composite is more tortuous than the carbon cloth. Furthermore, the CVs also reveal that the peak separation of the various samples is increasing in the following order: dip coat (1 layer), filtered through, dip coat (5 layers), dip coat (10 layers). This trend is consistent with findings in Section 5.4.3, wherein the degree of tortuosity scales with the 90-10 composite film thickness. Progressively increasing the thickness of the nano-carbon coating on the carbon cloth resulted in a rise in the degree of tortuosity of the electrode. This trend indicates that a balance between ESA and electrode transfer kinetics needs to be attained in order to maximise electrode performance.

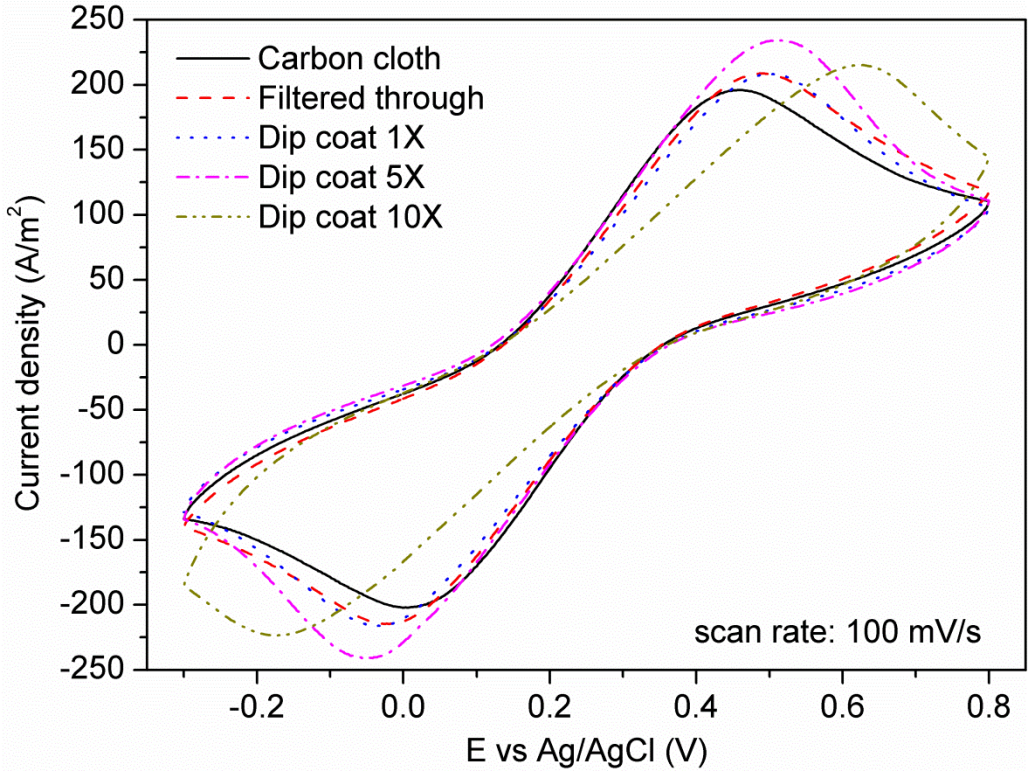

Figure 5.33 Cyclic voltammograms at a scan rate of 100 mV/s of the various vascular structured carbon electrodes investigated.

5.4.5.4 Thermocell testing of carbon cloth based electrodes

Thermocell testing of the carbon cloth based electrodes was done using a single piece per side. The stacked configuration was not done for these materials owing to their vascular nature.

Thermal harvesting experiments (Figure 5.34) indicated similar values of open circuit voltage (V_{oc}), around 41 mV. This V_{oc} equates to a temperature gradient of roughly 29.3 K, based on the Seebeck coefficient of 0.4 M $K_3Fe(CN)_6/K_4Fe(CN)_6$; which is 1.4 mV/K [7, 9].

J-V curves (Figure 5.34) indicate that the carbon cloth attained the lowest areal current density (38.91 A/m^2) of all electrodes tested. Incorporation of the 90-10

composite via the different methods tested resulted in an increase in areal current and power density. Filtration resulted in an areal current density of 51.45 A/m^2, an improvement of ~32 % as compared to carbon cloth. Dip coating produced varying degrees of improvement in areal current density. Having 1 layer yielded 47.98 A/m^2, a value slightly lower than that of the filtered sample. As mentioned previously (Section 5.4.5.3), the filtered sample had a higher faradaic peak current as compared with the single layer dip coated sample based on the CVs taken at 10 mV/s (Figure 5.32). Qualitative analysis of the CV implies that the filtered sample had a higher ESA which accounts for the higher areal current density in thermal harvesting experiments. The dip coated sample with 5 layers produced the largest areal current density (57.17 A/m^2) of all the carbon cloth based electrodes. These findings are in good agreement with the CVs (Figure 5.32) that reveal that this sample had the highest ESA. The 10-layers dip coated sample resulted in just a ~2 % improvement in areal current density compared to carbon cloth, producing only 39.61 A/m^2.This decrease in performance compared with the other electrodes wherein the 90-10 was incorporated may be attributed to the decrease in ESA (Figure 5.32) and slower electrode kinetics (Figure 5.33) of the 10-layers dip coat sample. As mentioned, the progressive increase in the layers of the nano-carbons deposited on the carbon cloth amplified the tortuous nature of the electrode. This increased tortuosity hindered ion flow and resulted in a decrease in areal current density.

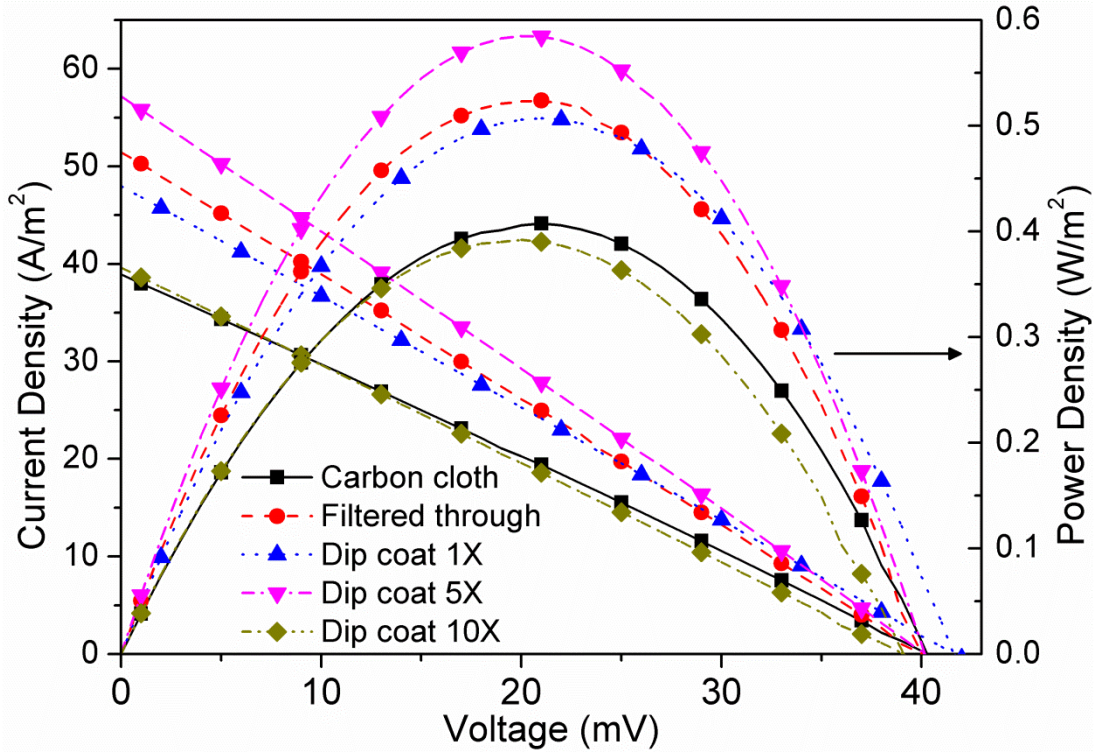

Figure 5.34 J-V curves generated using various vascular structure carbon electrodes. Electrolyte: 0.4 M $K_3Fe(CN)_6/K_4Fe(CN)_6$

Platinum films tested under similar conditions to the carbon cloth electrodes generated $P_{max}/\Delta T^2$ of 2.17 x 10^{-4} W/m^2-K^2 (Figure 5.35). Pristine carbon cloth produced the lowest $P_{max}/\Delta T^2$ of all the vascular electrode structures tested, only 4.75 x 10^{-4} W/m^2-K^2. Nevertheless, this value is ~119 % better than platinum. This highlights the importance of using electrodes that have a high internal surface area available for electron transfer. The trend in $P_{max}/\Delta T^2$ for the carbon cloth based electrodes is similar to that of areal current density. The 5-layers dip coated sample generated the largest areal power density (0.585 W/m^2), equivalent to a normalised areal power density ($P_{max}/\Delta T^2$) of 6.82 x 10^{-4} W/m^2-K^2.

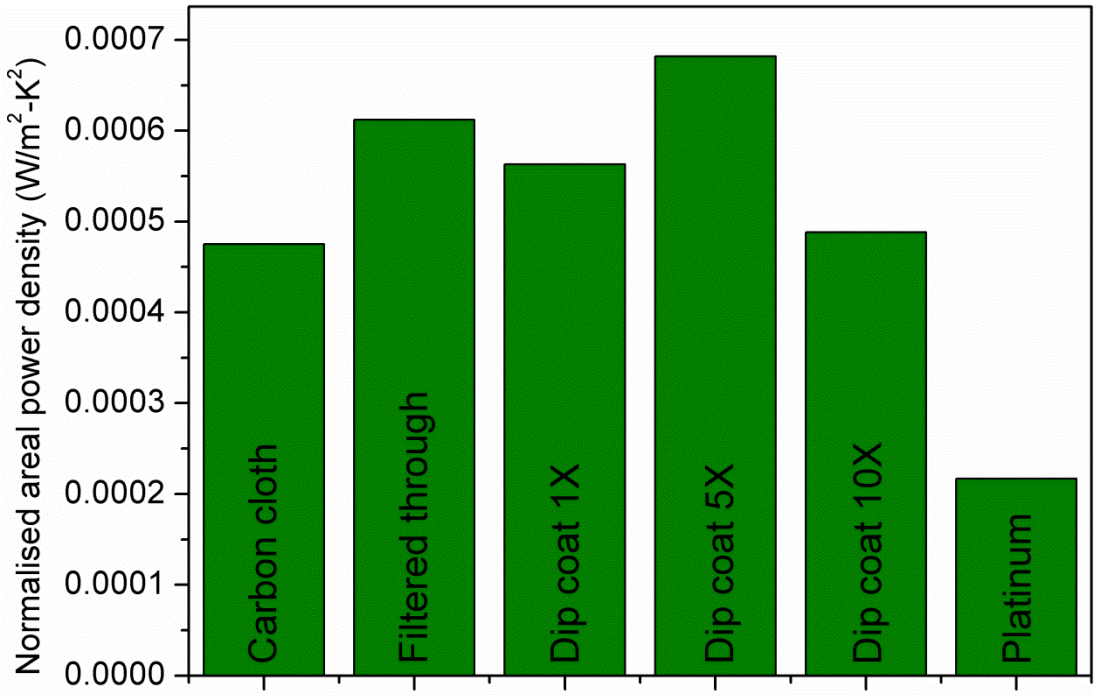

Figure 5.35 Normalised areal power density ($P_{max}/\Delta T^2$) attained through the use of various electrodes.

Extended tests of the dip coated samples with 5 layers (Figure 5.36) revealed a stable power output over a period of 48 hours. This suggests that ion flow was not hampered in said sample and that detrimental build-up of concentration gradients in the thermocell did not occur. This is important for electrodes with vascular structures as it indicates that a balance between the degree of tortuosity and ESA was attained [2].

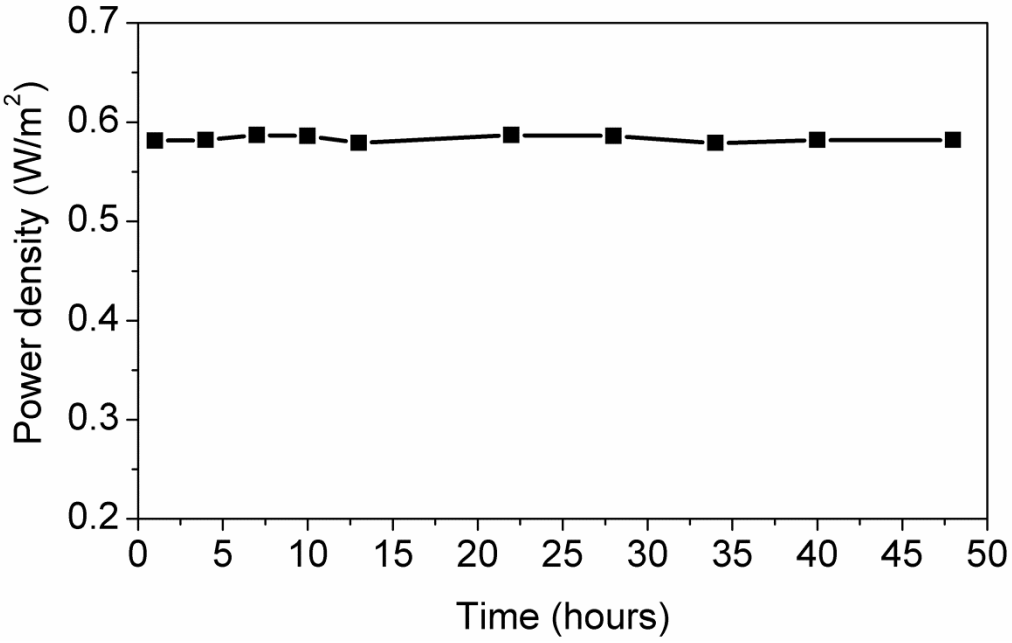

Figure 5.36 Power density obtained using the 5-layers dip coated electrodes over extended periods.

As expected from the produced power density, the dip coated sample with 5 layers had the highest efficiency relative to a Carnot engine (Φ_r = 0.930 %) among all the carbon cloth based electrodes tested (Figure 5.37). This Φ_r is an improvement of around 44 % compared to the pristine carbon cloth, which attained Φ_r = 0.648 %. It must be noted that the dip coated sample with 10 layers had roughly the same Φ_r as that of the optimised 90-10 film (4.5 μm thick, 90 % SWNT-10 % rGO, details in 5.4.3). This data suggests that having 10 layers of the 90-10 composite effectively blocks the pores of the carbon cloth. Excessive amounts of the nano-carbons will increase the tortuosity of the electrode and reduce the performance of the vascular structure to that of a thin film, i.e. the ESA is diminished.

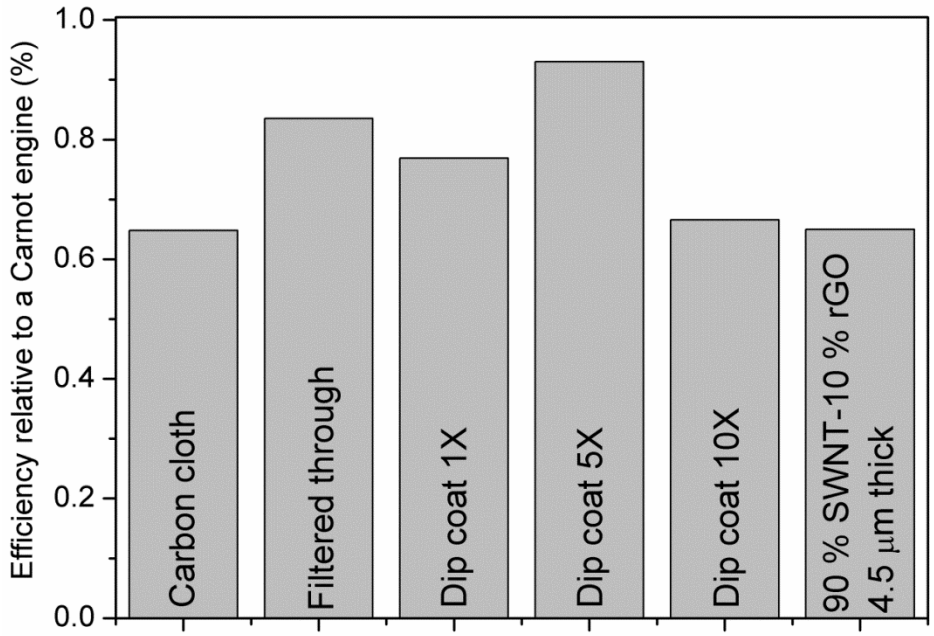

Figure 5.37 Efficiency relative to a Carnot engine of the various electrodes.

A summary of the thermocell testing results of the carbon cloth based electrodes is given in Table 5.5.

Table 5.5 Summary of data obtained from thermal energy harvesting experiments performed using various carbon cloth based electrodes.

Cell configuration	Carbon cloth	Filtered through	Dip coat 1X	Dip coat 5X	Dip coat 10X
ΔT (K)	29.3	29.3	30.0	29.3	28.3
Areal current density (A/m^2)	38.91	51.45	47.98	57.17	39.61
$I_{max}/\Delta T^2$ (A/m^2-K^2)	1.33	1.76	1.60	1.95	1.40
Areal power density (W/m^2)	0.408	0.525	0.507	0.585	0.392
$P_{max}/\Delta T^2$ (W/m^2-K^2)	4.75×10^{-4}	6.12×10^{-4}	5.63×10^{-4}	6.82×10^{-4}	4.88×10^{-4}
Φ (%)	0.051	0.066	0.062	0.073	0.051
Φ_r (%)	0.648	0.835	0.769	0.930	0.666

5.5 Conclusion

In conclusion, by optimising electrode composition and thickness (4.5 μm thick 90% SWNT – 10% rGO electrode), a delicate balance between porosity and tortuosity that favours rapid electrolyte diffusion and more efficient access to the electroactive surface area of the electrode has been attained. Using the optimised SWNT-rGO electrode in a novel stacked electrode configuration achieved $P_{area}/\Delta T^2$ that is ~380 % higher and $P_{mass}/\Delta T^2$ that is ~280 % larger than previously achieved using SWNT-rGO composite electrodes. These results demonstrate enhanced thermocell performance using significantly less active material. Furthermore, the 10 stack electrode configuration attained a record thermocell performance with Φ_r reaching up to 2.63 %. Quickenden et al stated that thermocells may have commercial possibilities if Φ_r between 2 to 5 % is attained [3]. However, further developments in nano-carbon synthesis are still necessary to decrease the price of SWNT and rGO in order to achieve commercialisation of thermocells.

It has also been demonstrated that the use of vascular electrode structures improves the performance of thermocells. More importantly, by incorporating the right quantity of nano-sized carbons into a vascular electrode the generated thermopower is further enhanced. This increased power output is a result of the larger ESA available when the 90-10 composite is combined with the carbon cloth. However, a delicate balance between ESA and tortuosity needs to be maintained. Excessive amounts of the 90-10 composite effectively blocks the pores in the carbon cloth and reduces the performance of the vascular structure as compared with that of a thin film.

Improvements in CNT and rGO synthesis may lead to mass production of these materials at reduced costs, which could facilitate mass production of thermogalvanic systems.

5.6 References

1. Mua, Y. and T.I. Quickenden, *Power Conversion Efficiency, Electrode Separation, and Overpotential in the Ferricyanide/Ferrocyanide Thermogalvanic Cell.* Journal of The Electrochemical Society, 1996. **143**(8): p. 2558-2564.
2. Quickenden, T.I. and Y. Mua, *The Power Conversion Efficiencies of a Thermogalvanic Cell Operated in Three Different Orientations.* Journal of The Electrochemical Society, 1995. **142**(11): p. 3652-3659.
3. Quickenden, T.I. and Y. Mua, *A Review of Power Generation in Aqueous Thermogalvanic Cells.* Journal of The Electrochemical Society, 1995. **142**(11): p. 3985-3994.
4. Nugent, J.M., et al., *Fast Electron Transfer Kinetics on Multiwalled Carbon Nanotube Microbundle Electrodes.* Nano Letters, 2001. **1**(2): p. 87-91.
5. El-Kady, M.F., et al., *Laser Scribing of High-Performance and Flexible Graphene-Based Electrochemical Capacitors.* Science, 2012. **335**(6074): p. 1326-1330.
6. Romano, M., et al., *Novel carbon materials for thermal energy harvesting.* Journal of Thermal Analysis and Calorimetry, 2012. **109**(3): p. 1229-1235.

7. Kang, T.J., et al., *Electrical Power From Nanotube and Graphene Electrochemical Thermal Energy Harvesters.* Advanced Functional Materials, 2012. **22**(3): p. 477-489.

8. Hu, R., et al., *Harvesting Waste Thermal Energy Using a Carbon-Nanotube-Based Thermo-Electrochemical Cell.* Nano Letters, 2010. **10**(3): p. 838-846.

9. Burrows, B., *Discharge Behavior of Redox Thermogalvanic Cells.* Journal of The Electrochemical Society, 1976. **123**(2): p. 154-159.

10. Wang, S. and R.A.W. Dryfe, *Graphene oxide-assisted deposition of carbon nanotubes on carbon cloth as advanced binder-free electrodes for flexible supercapacitors.* Journal of Materials Chemistry A, 2013. **1**(17): p. 5279-5283.

11. Chen, Y.-C., et al., *Highly flexible supercapacitors with manganese oxide nanosheet/carbon cloth electrode.* Electrochimica Acta, 2011. **56**(20): p. 7124-7130.

12. Bergin, S.D., et al., *New Solvents for Nanotubes: Approaching the Dispersibility of Surfactants.* The Journal of Physical Chemistry C, 2009. **114**(1): p. 231-237.

13. Marcano, D.C., et al., *Improved Synthesis of Graphene Oxide.* ACS Nano, 2010. **4**(8): p. 4806-4814.

14. Tryba, B., A.W. Morawski, and M. Inagaki, *Preparation of exfoliated graphite by microwave irradiation.* Carbon, 2005. **43**(11): p. 2417-2419.

15. Falcao, E.H.L., et al., *Microwave exfoliation of a graphite intercalation compound.* Carbon, 2007. **45**(6): p. 1367-1369.

16. Casiraghi, C., et al., *Raman Spectroscopy of Graphene Edges.* Nano Letters, 2009. **9**(4): p. 1433-1441.

17. Khan, U., et al., *High-Concentration Solvent Exfoliation of Graphene.* Small, 2010. **6**(7): p. 864-871.

18. Schniepp, H.C., et al., *Functionalized Single Graphene Sheets Derived from Splitting Graphite Oxide.* The Journal of Physical Chemistry B, 2006. **110**(17): p. 8535-8539.

19. Salzmann, C.G., et al., *The Role of Carboxylated Carbonaceous Fragments in the Functionalization and Spectroscopy of a Single-Walled Carbon-Nanotube Material.* Advanced Materials, 2007. **19**(6): p. 883-887.

20. Dresselhaus, M.S., et al., *Raman spectroscopy of carbon nanotubes.* Physics Reports, 2005. **409**(2): p. 47-99.

21. Shiau, S.H., et al., *Growth of a single-wall carbon nanotube film and its patterning as an n-type field effect transistor device using an integrated circuit compatible process.* Nanotechnology, 2008. **19**(10): p. 105303.

22. Chen, H., et al., *Mechanically Strong, Electrically Conductive, and Biocompatible Graphene Paper.* Advanced Materials, 2008. **20**(18): p. 3557-3561.

23. Randles, J.E.B., *Kinetics of rapid electrode reactions.* Discussions of the Faraday Society, 1947. **1**: p. 11-19.

24. Bard, A.J. and L.R. Faulkner, eds. *Electrochamical Methods-Fundamentals and Applications*. 2nd ed. 2001, John Wiley and Sons, Inc: New York.

25. Park, S.-M. and J.-S. Yoo, *Peer Reviewed: Electrochemical Impedance Spectroscopy for Better Electrochemical Measurements.* Analytical Chemistry, 2003. **75**(21): p. 455 A-461 A.

26. Park, S., et al., *Graphene Oxide Papers Modified by Divalent Ions—Enhancing Mechanical Properties via Chemical Cross-Linking.* ACS Nano, 2008. **2**(3): p. 572-578.

27. Park, S., et al., *Graphene Oxide Sheets Chemically Cross-Linked by Polyallylamine.* The Journal of Physical Chemistry C, 2009. **113**(36): p. 15801-15804.

28. Pacios, M., et al., *Electrochemical behavior of rigid carbon nanotube composite electrodes.* Journal of Electroanalytical Chemistry, 2008. **619-620**(0): p. 117-124.

29. Nicholson, R.S., *Theory and Application of Cyclic Voltammetry for Measurement of Electrode Reaction Kinetics.* Analytical Chemistry, 1965. **37**(11): p. 1351-1355.

30. Matthey, J. *Platinum Today*. [cited 2013; Available from: http://www.platinum.matthey.com/prices/price-charts.

31. Dresselhaus, M.S., et al., *Raman spectroscopy on one isolated carbon nanotube.* Physica B: Condensed Matter, 2002. **323**(1–4): p. 15-20.

32. Kudin, K.N., et al., *Raman Spectra of Graphite Oxide and Functionalized Graphene Sheets.* Nano Letters, 2007. **8**(1): p. 36-41.

CHAPTER 6

Summary, General Conclusions and Perspective

6.1 Summary and conclusions

An investigation into the effects of electrolyte concentration, cell configuration, composition and structure of the electrode material on thermogalvanic systems' performance has been carried out. The enhanced understanding of these parameters has led to significant improvements in thermocell performance. Development of novel carbon electrode materials has resulted in a record efficiency relative to a Carnot engine (Φ_r) of 2.63 %.

The initial part of this work focused on an investigation of the concentration of $K_3Fe(CN)_6/K_4Fe(CN)_6$ in aqueous media as the electrolyte for thermocell applications with carbon based electrodes. As the concentration of said redox couple was increased, the thermal conductivity of the electrolyte decreased. Decreased electrolyte thermal conductivity is desirable in thermocell applications as this mitigates the thermal flux between the hot and cold half-cells; i.e. it allows larger thermal gradients to be established. The ionic conductivity was shown to scale with electrolyte concentration. Increased ionic conductivity is advantageous as it lowers the ohmic overpotential in thermocells. Through the use of the highest possible concentration of $K_3Fe(CN)_6/K_4Fe(CN)_6$ in aqueous media, which is 0.4 M (the saturation limit of said redox couple in water), the thermocell current density is maximised.

The cell configuration used in thermogalvanic systems plays an important role in the power generation capabilities of these devices. A variety of thermocell designs were developed and tested in order to attain an understanding of how electrodes should be positioned to achieve increased power output. With electrodes placed far apart, a large temperature difference between the anode and cathode may be reached. However, this results in a lower current density because of the larger distance that ions need to diffuse in the thermocell. Electrodes also need to be oriented such that reaction products from the cathode only need to travel in a straight path to get to the anode, and vice versa. A comparison in performance of all the "single" chamber thermocells reveals that the T-shaped device is able to generate the highest power density at the highest efficiency. The fact that this cell configuration does not require extensive amounts of electrolyte makes it attractive for use in benchmarking the performance of various electrode materials. Through appropriate cell design, thermocells may be connected in series to significantly augment power output from a single heat source.

Composite electrodes of single-walled carbon nanotubes (SWNT) and reduced graphene oxide (rGO) for thermocell applications were developed in this study. The reason for the use of these nano-carbon materials was mainly due to their enhanced electroactive surface area (ESA). Benchmarking of electrode performance was done using the established 0.4 M $K_3Fe(CN)_6/K_4Fe(CN)_6$ in aqueous media and T-shaped cell configuration. An electrode composed solely of SWNT did not perform as well as the composite electrodes. The results indicate that this is due to the tortuous nature of SWNT films, which hinders electrolyte diffusion. Pure rGO electrodes generated the lowest power density of all the carbon materials. The

diminished performance of said material may be attributed to the defects introduced during the oxidation step of rGO synthesis, thus lowering conductivity. Additionally, re-stacking of rGO sheets due to van der Waals interactions inhibits ion accessibility and reduces ESA [1]. Optimisation of electrode composition revealed that the highest power density may be obtained by use of 90 % SWNT and 10 % rGO by weight (90-10). This is most likely due to the enhanced ESA of said composition as observed via cyclic voltammetry.

An increase in ESA may be realised through the use of thicker 90-10 composite films. The optimum 90-10 electrode thickness was established to be 4.5 µm. To ensure stable power output in thermocells, reactants at the cathode need to be replenished by the reaction products formed at the anode and vice versa [2]. Electrodes must be structured so as to facilitate this diffusion process and thus minimise the mass transport overpotential [3]. As film thickness is increased, the random orientations of the pores leads to increased tortuosity of the film thus exacerbating the problems associated with reactant/product diffusion, especially through the electrode; i.e. thicker materials have longer diffusion paths. A delicate balance between electrode porosity and tortuosity is attained through the use of the 90-10 composite at a thickness of 4.5 µm. This optimised electrode material favours rapid electrolyte diffusion and more efficient access to the ESA.

Further enhancements in thermocell performance were realised through the use of a novel stacked electrode configuration. Said configuration consists of alternating layers of the optimised SWNT-rGO film and stainless steel. The stainless steel mesh acts as a separator between the SWNT-rGO films, allowing the electrolyte to interact with the high surface area of the nano-carbons while

facilitating ionic diffusion. It also maintains a conductive path for electrons between the individual films. Using 10 optimised SWNT-rGO films per half-cell (10 stack configuration) achieved a normalised areal power density ($P_{area}/\Delta T^2$) that is ~380 % higher and normalised mass power density($P_{mass}/\Delta T^2$) that is ~280 % higher than previously achieved using SWNT-rGO composite electrodes [3]. These results demonstrate enhanced thermocell performance using significantly less active material. Furthermore, the 10-stack electrode configuration attained a record power conversion efficiency relative to a Carnot engine, Φ_r of 2.63 %. This Φ_r is a remarkable 88 % improvement compared to the highest reported Φ_r in thermocells (1.4 %) [4]. Quickenden et al stated that thermocells may have commercial possibilities if Φ_r between 2 to 5 % is attained [2]. Further developments in nano-carbon synthesis will lead to a decrease in production costs of these materials and could result in commercialisation of thermocells.

The final part of this study was to investigate the effect of vascular electrode structures on thermocell performance. Carbon cloth, which consists of carbon fibres that are woven in the form of cloth is an attractive material for thermocell electrodes owing to its low electrical resistance, light weight, high porosity, chemical and thermal stability, good mechanical strength, and high degree of flexibility [5, 6]. The developed 90-10 composite was incorporated into the carbon cloth using a variety of methods. The maximum power density is obtained by dip coating the carbon cloth with 5 layers of the 90-10 composite. This increased performance may be attributed to the larger ESA of the resulting electrode material as shown by cyclic voltammetry. Excessive amounts of the 90-10 composite blocks the pores in the carbon cloth and reduces the performance of the vascular structure to that of a thin film.

6.2 Perspective

Whilst this work discusses the incorporation of carbon nanomaterials onto vascular electrode structures, further enhancements in thermocell performance may be realised if more controllable deposition techniques are employed. Electrophoretic deposition (EPD) is one such method that may be used for the production of coatings of carbon nanomaterials [5, 7]. The degree of control on the deposition parameters in EPD may facilitate the uniform deposition of nano-carbons (thus increasing the ESA) while maintaining the macro porosity of the vascular electrode structure.

The use of doped carbon nanomaterials has been shown to enhance the catalytic activity in various electrochemical applications. Nitrogen-doped carbon nanotubes (CNTs) have high electrocatalytic activity in oxygen reduction reactions as compared to undoped CNTs [8]. Boron-doped CNTs are also attractive as electrode materials owing to the increased edge plane sites on the CNT surface; proven to be the predominant region for electron transfer. Initial work on using doped CNTs for thermocells revealed that electrodes that possess a higher ESA are necessary to increase their power generation capability [9]. Deposition of doped carbon nanomaterials onto the vascular electrode structures developed in this work may improve thermocell performance by providing a combination of lowered activation overpotential and high ESA.

As shown in Chapter 4, connecting thermocells in series significantly augments the amount of power generated from a single heat source. Further development of said cell design wherein the material used would be able to

withstand higher temperatures would improve device performance. Furthermore, the thermocell should be composed of a material or configured such that unnecessary thermal losses are eliminated or minimised. If the thermal resistances between the heating source and the hot electrode, and the cooling element and the cold electrode are eliminated then the thermal gradient in the cell may be maximised. A potential series thermocell configuration that may be used on heating pipes is shown in Figure 6.1. Heat will be provided by the hot pipe that each cell is in contact with, while cooling will be facilitated by the heat sinks attached to the opposite end.

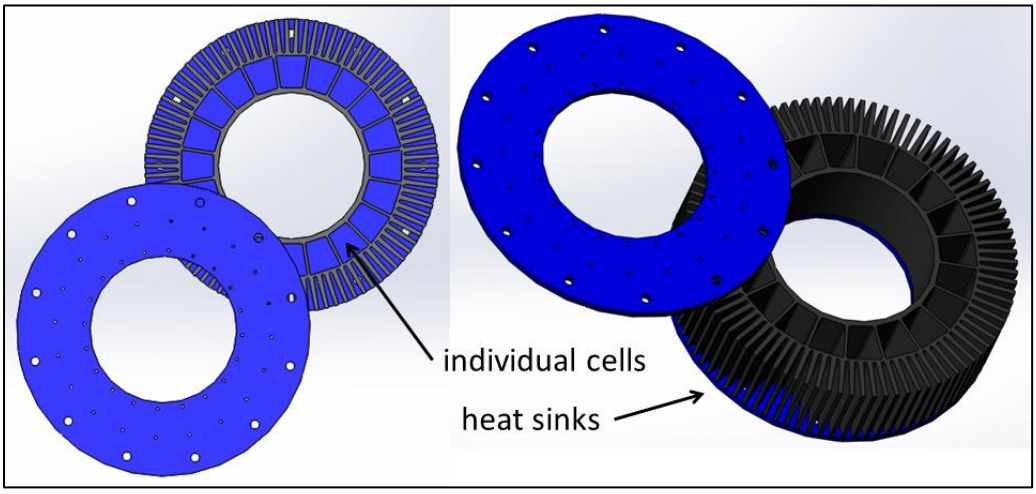

Figure 6.1 Schematic of a potential series thermocell that may be used around heating pipes.

It has been shown in chapter 5 that the use of a stacked electrode configuration produces a remarkable increase in power conversion efficiency relative to a Carnot engine (Φ_r). However, going from a 5 stack to a 10 stack configuration does not double the Φ_r. This is most likely caused by ohmic losses incurred when stacking the individual films. Improvements in said electrode configuration wherein said ohmic losses are reduced may result in further enhancements in device performance.

Throughout this study the electrolyte utilised was $K_3Fe(CN)_6/K_4Fe(CN)_6$ in aqueous media. Said electrolyte is limited to operating temperatures below 100 ^oC due to the boiling point of water. Certain waste heat sources fall between 100 ^oC and 200 ^oC. In order to maximise the power generation capabilities of thermogalvanic systems, the electrolyte must be stable within said temperature range. Recent work has emerged on using ionic liquid as electrolytes for thermogalvanic cells [10, 11]. The thermal stability of said materials makes them ideal for thermal energy harvesting applications in the 100-200 ^oC range [12]. However, these initial studies on ionic liquid electrolytes have been limited to the use of platinum electrodes. The investigation of thermocells with ionic liquid electrolytes and nano-structured carbons as electrodes may yield improvements in thermo-energy conversion efficiency.

6.3 References

1. Chen, H., et al., *Mechanically Strong, Electrically Conductive, and Biocompatible Graphene Paper.* Advanced Materials, 2008. **20**(18): p. 3557-3561.
2. Quickenden, T.I. and Y. Mua, *A Review of Power Generation in Aqueous Thermogalvanic Cells.* Journal of The Electrochemical Society, 1995. **142**(11): p. 3985-3994.
3. Kang, T.J., et al., *Electrical Power From Nanotube and Graphene Electrochemical Thermal Energy Harvesters.* Advanced Functional Materials, 2012. **22**(3): p. 477-489.

4. Hu, R., et al., *Harvesting Waste Thermal Energy Using a Carbon-Nanotube-Based Thermo-Electrochemical Cell.* Nano Letters, 2010. **10**(3): p. 838-846.

5. Wang, S. and R.A.W. Dryfe, *Graphene oxide-assisted deposition of carbon nanotubes on carbon cloth as advanced binder-free electrodes for flexible supercapacitors.* Journal of Materials Chemistry A, 2013. **1**(17): p. 5279-5283.

6. Chen, Y.-C., et al., *Highly flexible supercapacitors with manganese oxide nanosheet/carbon cloth electrode.* Electrochimica Acta, 2011. **56**(20): p. 7124-7130.

7. Boccaccini, A.R., et al., *Electrophoretic deposition of carbon nanotubes.* Carbon, 2006. **44**(15): p. 3149-3160.

8. Gong, K., et al., *Nitrogen-Doped Carbon Nanotube Arrays with High Electrocatalytic Activity for Oxygen Reduction.* Science, 2009. **323**(5915): p. 760-764.

9. Salazar, P.F., S. Kumar, and B.A. Cola, *Nitrogen- and Boron-Doped Carbon Nanotube Electrodes in a Thermo-Electrochemical Cell.* Journal of The Electrochemical Society, 2012. **159**(5): p. B483-B488.

10. Abraham, T.J., D.R. MacFarlane, and J.M. Pringle, *High Seebeck coefficient redox ionic liquid electrolytes for thermal energy harvesting.* Energy & Environmental Science, 2013. **6**(9): p. 2639-2645.

11. Zinovyeva, V., et al., *Enhanced Thermoelectric Power in Ionic Liquids.* ChemElectroChem, 2013: p. n/a-n/a.

12. Johnson, K.E., *What's an Ionic Liquid.* The Electrochemical Society's INTERFACE, 2007. **16**(1).